

DOCTOR OF PHILOSOPHY

Advanced control and optimisation of DC-DC converters with application to low carbon technologies

Maganga, Othman G.

Award date:
2015

Awarding institution:
Coventry University

[Link to publication](#)

General rights

Copyright and moral rights for the publications made accessible in the public portal are retained by the authors and/or other copyright owners and it is a condition of accessing publications that users recognise and abide by the legal requirements associated with these rights.

- Users may download and print one copy of this thesis for personal non-commercial research or study
- This thesis cannot be reproduced or quoted extensively from without first obtaining permission from the copyright holder(s)
- You may not further distribute the material or use it for any profit-making activity or commercial gain
- You may freely distribute the URL identifying the publication in the public portal

Take down policy

If you believe that this document breaches copyright please contact us providing details, and we will remove access to the work immediately and investigate your claim.

Advanced Control and Optimisation of DC-DC Converters with Application to Low Carbon Technologies

Othman G Maganga

B.Eng, MSc, MInstMC

A Thesis submitted in partial fulfillment of the University's requirements for the
Degree of Doctor of Philosophy
September 2015

Control Theory and Applications Centre

Coventry University

Acknowledgement: Support of European Thermodynamics Limited, Kibworth,
Leicester, UK

Abstract

Prompted by a desire to minimise losses between power sources and loads, the aim of this Thesis is to develop novel maximum power point tracking (MPPT) algorithms to allow for efficient power conversion within low carbon technologies. Such technologies include: thermoelectric generators (TEG), photovoltaic (PV) systems, fuel cells (FC) systems, wind turbines etc. MPPT can be efficiently achieved using extremum seeking control (ESC) also known as perturbation based extremum seeking control. The basic idea of an ESC is to search for an extrema in a closed loop fashion requiring only a minimum of a *priori* knowledge of the plant or system or a cost function.

In recognition of problems that accompany ESC, such as limit cycles, convergence speed, and inability to search for global maximum in the presence local maxima this Thesis proposes novel schemes based on extensions of ESC. The first proposed scheme is a variance based switching extremum seeking control (VBS-ESC), which reduces the amplitude of the limit cycle oscillations. The second scheme proposed is a state dependent parameter extremum seeking control (SDP-ESC), which allows the exponential decay of the perturbation signal. Both the VBS-ESC and the SDP-ESC are universal adaptive control schemes that can be applied in the aforementioned systems. Both are suitable for local maxima search. The global maximum search scheme proposed in this Thesis is based on extensions of the SDP-ESC. Convergence to the global maximum is achieved by the use of a searching window mechanism which is capable of scanning all available maxima within operating range. The ability of the proposed scheme to converge to the global maximum is demonstrated through various examples. Through both simulation and experimental studies the benefit of the SDP-ESC has been consistently demonstrated.

Acknowledgements

I am deeply indebted to my Director of studies Dr Malgorzata Sumislawska, my Supervisors Prof. Keith Burnham and Joe Mahtani from the Control Theory and Applications Centre (CTAC) for their advice, kindness, encouragement and stimulating suggestions which motivated me while working on this Thesis. Also, I would like to thank Kevin Simpson and other members of European Thermodynamics Limited for the support they have given me while conducting my research. Furthermore, I pass on my thanks to Andrea Montecucco from Glasgow University and my colleague Navneesh Phillip and all of those who supported me in any respect during the completion of my Thesis. Lastly, I offer my regards and blessings to my lovely wife Martyna Maganga and my family for their advice and encouragement that enabled me to complete this work.

Contents

	Page
Abstract	i
Acknowledgements	ii
Contents	iii
List of Figures	vi
Nomenclature	xii
Abbreviations	xii
Notation	xiii
1 Introduction	1
1.1 Introduction	1
1.2 Statement of the problem	2
1.2.1 Local maxima search for mismatch reduction	2
1.2.2 Global maximum search in the presence of local maxima	4
1.3 Scope and goals of this Thesis	4
1.4 List of publications	7
1.5 Original contributions	8
1.6 Outline of the Thesis	10
2 A review of maximum power point tracking algorithms	13
2.1 Introduction	13
2.2 Perturb and observe (P & O)/ Hill climbing	14
2.3 Incremental conductance	17
2.4 Open circuit voltage/short circuit current	21
2.4.1 Open circuit voltage	21
2.4.2 Short circuit current	24

2.5	Artificial intelligence methods	24
2.6	Hybrid methods	26
2.7	Performance comparison	29
2.8	Critical appraisal and conclusions	32
3	Extremum seeking control	34
3.1	Introduction	34
3.2	Survey on extremum seeking control	35
3.2.1	Non constraints based ESC	43
3.3	PESC concept, analysis and design	44
3.3.1	Problem description	45
3.3.2	Gradient search	47
3.3.3	Plant dynamics and learning time scale	50
3.3.4	PESC parameter design	55
3.4	Limit cycle minimisation	56
3.4.1	Lyapunov function based switching (LBS) extremum seeking control	56
3.4.2	Variance Based Switching (VBS) ESC	59
3.5	Critical appraisal and conclusions	61
4	State dependent parameter (SDP) extremum seeking control	62
4.1	Introduction	62
4.2	SDP-ESC intuitive explanation	64
4.3	Convergence analysis	66
4.3.1	SDP-ESC for a static map	66
4.4	Stability analysis	71
4.5	SDP-ESC design for single parameter scheme	79
4.5.1	Algorithm design guideline	79
4.6	Simulation examples	82
4.6.1	SDP-ESC for LTI system	82
4.6.2	SDP-ESC for plant with dynamics	85
4.7	Sensitivity analysis	86
4.7.1	SDP-ESC tuning parameters	88
4.7.2	Measurement noise	90
4.8	Critical appraisal and conclusions	94
5	Extended SDP extremum seeking control	95
5.1	Introduction	95

5.2	Problem statement	97
5.2.1	GM scanning scheme	98
5.3	Simulation study	102
5.3.1	Static nonlinear map: Example 1	102
5.3.2	Static nonlinear map: Example 2	105
5.3.3	Static nonlinear map: Example 3	105
5.3.4	Plant with dynamics: Example 4	110
5.4	Critical appraisal and conclusions	112
6	Simulation study: Application in thermoelectric generator systems	113
6.1	Introduction	113
6.2	TEG overview	114
6.3	Power conditioning unit (PCU) modelling	117
6.3.1	DC-DC converter modelling	118
6.3.2	Control technique modelling:	121
6.4	MPPT performance criterion	121
6.5	Simulation study: Phase I	123
6.5.1	Findings and observations	125
6.6	Simulation study: Phase II	125
6.7	Critical appraisal and conclusions	134
7	Experimental work	135
7.1	Introduction	135
7.2	Experiment-setup: Phase I	136
7.2.1	Synchronous DC-DC converter	136
7.2.2	dSPACE interface	138
7.2.3	TEG test rig and electrical characterisation	139
7.2.4	Steady state analysis	140
7.2.5	TEG emulation: fast transients analysis	141
7.2.6	Transient analysis with actual TEG	143
7.2.7	Findings and observations	145
7.3	Experimental set-up: Phase II	146
7.3.1	TEG test rig and electrical characterisation	146
7.3.2	TEG emulation via power supply unit	148
7.3.3	Transients analysis with real TEG system	151
7.4	Critical appraisal and conclusions	159

8	Conclusions and Further work	160
8.1	Conclusions and Further work	160
8.1.1	VBS-ESC for local maxima search	160
8.1.2	SDP-ESC for local maxima search	161
8.1.3	Extended SDP-ESC for global maximum search	162
8.1.4	Modelling, simulation and experimental validation: TEG .	163
8.2	Further work	164
8.2.1	Constrained VBS-ESC/SDP-ESC scheme	165
8.2.2	Experimental validation global maximum searching scheme	165
8.2.3	Embedding VBS-ESC/SDP-ESC for stand-alone operation	166
8.2.4	Degradation of PCU components	166
	References	166
	Appendices	180
A	Description of the TEG model	181
A.1	Thermal electric module (TEM)	181
A.2	Heat exchange (HX) subsystem	183
B	Simulink block diagram for MPPT algorithms	185
B.1	Simulink models of MPPT algorithms	185
C	Components/Instruments used in the HIL set-up	192
C.1	Cartridge heater and temperature control box	193
C.2	Synchronous DC-DC buck-boost converter	195
C.3	GM250-127-28-12 TEMs characteristics	196

List of Figures

1.1	Maximum power point tracking configuration with various systems	2
1.2	Structural representation of a logical flow of the developments of this Thesis	12
2.1	Power conditioning unit (PCU)	14
2.2	A flow chart algorithm for perturb and observe (P&O)	16
2.3	Curve for Power Vs Source voltage	18
2.4	A flow chart algorithm for incremental conductance (IC)	20
2.5	A flow chart of open circuit voltage method	22
2.6	A generic flow chart for hybrid methods	27
3.1	Block diagram of perturbation based extremum seeking control . .	45
3.2	Extremum seeking control scheme	47
3.3	Perturbation extremum seeking control	51
3.4	PESC with Lyapunov based switching	58
3.5	PESC with variance based switching	60
4.1	Illustrates state dependent parameter (SDP) ESC scheme	65
4.2	Simplified SDP-ESC scheme	67
4.3	Illustrates output of the ESC and the SDP-ESC for LTI system . .	84
4.4	Illustrates estimates of the PESC and the SDP-ESC for LTI system	84
4.5	Illustrates steady-state percentage error of the estimated input obtained using the PESC and the SDP-ESC, respectively.	85
4.6	u parameter for ESC and SDP-ESC	87
4.7	Output measurement for PESC and SDP-ESC	87
4.8	Illustrates estimates of the SDP-ESC for different α	88
4.9	Illustrates output of the SDP-ESC for different α	89
4.10	Illustrates perturbation gain amplitude of the SDP-ESC for different α	89
4.11	Illustrates output of the SDP-ESC for different k	90

4.12	Illustrates estimates of the SDP-ESC for different k	91
4.13	Illustrates perturbation gain amplitude of the SDP-ESC for different k	92
4.14	Noise level effects on estimates for PESC and SDP-ESC	93
5.1	Block diagram of the extended SDP-ESC scheme for global maximum search	98
5.2	Extended SDP-ESC scheme for global maximum search in the presence of local maxima	100
5.3	Flow chart for global maximum searching using extended SDP-ESC scheme	101
5.4	Control input for PESC, SDP-ESC and extended SDP-ESC for global maximum search of example in Section 5.3.1	103
5.5	Output of example in Section 5.3.1	104
5.6	Input-output map of example in Section 5.3.1	104
5.7	Control input for PESC, SDP-ESC and extended SDP-ESC for global maximum search of example in Section 5.3.2	106
5.8	Output of example 5.3.2	106
5.9	Input-output map of example 5.3.2	107
5.10	Control input for PESC, SDP-ESC and extended SDP-ESC for global maximum search of example in Section 5.3.3	108
5.11	Output of example in Section 5.3.3	108
5.12	Input-output map of example in Section 5.3.3	109
5.13	Control input for PESC, SDP-ESC and extended SDP-ESC for plant with dynamics	111
5.14	Output of example in Section 5.3.4	111
6.1	Thermoelectric module (TEM)	115
6.2	Block diagram of waste heat recovery from engine exhaust	116
6.3	TEG model integration of subsystems	117
6.4	Schematic diagram of a synchronous DC-DC buck-boost converter	119
6.5	Waveform for CCM and DCM, where dT_s denote period when switch is closed and T_s denote switching period	120
6.6	Block diagram for the pulse width modulation (PWM)	122
6.7	Simulation results for theoretical power, output power with ESC, P&O and Fixed Duty Cycle: Losses reduced to within 5%	124
6.8	Simulation results of V_{mpp} , I_{mpp} and d using PESC, LBS-ESC, VBS-ESC and SDP-ESC MPPT algorithms	127

6.9	Variance of state \hat{x} for SDP-ESC scheme	128
6.10	Simulation results for PESC, LBS-ESC, VBS-ESC and SDP-ESC MPPT algorithms while PSU voltage increased from 12V to 16V by step increment of 2V	129
6.11	Variance of state \hat{x} for SDP-ESC algorithm while PSU voltage increased from 12V to 16V by step increment of 2V	130
6.12	Lyapunov function for the LBS-ESC while PSU voltage increased from 12V to 16V by step increment of 2V	131
6.13	Simulation results for PESC, LBS-ESC, VBS-ESC and SDP-ESC MPPT algorithms while PSU voltage increased from 12V to 16V and then reduced from 16V to 14V	132
6.14	Variance of state \hat{x} for VBS-ESC algorithm while PSU voltage increased from 12V to 16V by step increment of 2V	133
6.15	Lyapunov function for the LBS-ESC while PSU voltage increased from 12V to 16V and then reduced from 16V to 14V	133
7.1	Schematic diagram of the connections between instrumentals and devices used for the experimental tests	137
7.2	Picture of the top layer of the converters PCB. The bottom layer hosts the inductor and the capacitors.	138
7.3	Electrical characterisation for TEG-2 and for three different tem- perature gradients: 100°C, 150°C, and 200°C between the hot and cold sides of the thermoelectric module.	140
7.4	Steady-state performance of perturb and observe and ESC algo- rithms for 100°C, 150°C, and 200°C temperature difference	141
7.5	Converter's operating input voltage during PSU open-circuit volt- age transients (12V, 15V, 18V) with the perturb and observe con- troller. Expected theoretical input voltage would be: 6V, 7.5V, 9V. Time <i>div.</i> = 100ms; voltage <i>div.</i> = 1V	142
7.6	Converter's operating input voltage during PSU open-circuit volt- age transients (12V, 15V, 18V) with the ESC. Expected theoretical input voltage would be: 6V, 7.5V, 9V. Time <i>div.</i> = 100ms; voltage <i>div.</i> = 1V	143
7.7	Thermal transient test of the TEGs from $\Delta T = 100^\circ\text{C}$ to $\Delta T =$ 200°C, connected to the converter with the perturb and observe MPPT algorithm. Tracking with accuracy around 5% the transient maximum estimated TEG.	144

7.8	Thermal transient test of the TEGs from $\Delta T = 200^{\circ}\text{C}$ to $\Delta T = 100^{\circ}\text{C}$, connected to the converter with the ESC MPPT algorithm. Tracking with accuracy around 5% the transient maximum estimated TEG.	145
7.9	Rig provided by ETL used for experiment tests phase II	147
7.10	Schematic diagram of coolant of the rig used in experiment phase II	147
7.11	Input current at MPP for emulated TEG at steady-state operation	149
7.12	Input voltage at MPP with emulated TEG at steady-state operation	150
7.13	Illustrates duty cycle for a standard ESC and SDP-ESC	151
7.14	Zoomed input current at MPP (I_{mpp}) for variable open circuit voltage	152
7.15	Zoomed input voltage at MPP (V_{mpp}) for variable open circuit voltage	153
7.16	Transient response of emulated TEG with PESC and SDP-ESC MPPT algorithms	154
7.17	Hot side temperature measurements for the real TEG system with PESC and SDP-ESC MPPT algorithms	155
7.18	Cold side temperature measurements for the real TEG system with PESC and SDP-ESC MPPT algorithms	155
7.19	Temperature difference (ΔT) measurements for the real TEG system with PESC and SDP-ESC MPPT algorithms	156
7.20	Duty cycle measurements for the real TEG system with the use of PESC and SDP-ESC MPPT algorithms	156
7.21	Input voltage at MPP (V_{mpp}) for the real TEG system with PESC and SDP-ESC MPPT algorithms	157
7.22	Comparison of limit cycle minimisation between PESC and SDP-ESC MPPT algorithms when applied to the real TEG system. SDP-ESC tracking with an accuracy around of 4% of the transient maximum estimated TEG	158
A.1	TEG subsystem configuration in comparison to physical system . .	182
A.2	TEG HX/TEM configuration	184
B.1	Simulink block diagram for P&O, PESC, LBS-ESC, VBS-ESC and SDP-ESC subsystems	186
B.2	Simulink block diagram for PESC subsystem	187
B.3	Simulink block diagram for sensor measurements from ADCs . . .	188
B.4	Simulink block diagram for LBS-ESC subsystem	189
B.5	Simulink block diagram for VBS-ESC subsystem	189
B.6	Simulink block diagram for SDP-ESC subsystem	190

B.7	Simulink block diagram for extended SDP-ESC subsystem	190
B.8	Simulink block diagram for window search subsystem	191
C.1	Schematic diagram of control box used in experiment test phase II	193
C.2	Specifications for cartridge heater block used in experiment phase II	194
C.3	Schematic diagram of DC-DC buck-boost converter used for ex- periment tests	195

Nomenclature

Abbreviations

ABS	anti-locking brake systems
AI	artificial intelligence
AP-ESC	approximation extremum seeking control
AESC	adaptive extremum seeking control
BPF	band pass filter
DC	direct current
EKF	extended Kalman filter
ESC	extremum seeking control
ESR	equivalent series resistor
FC	fuel cells
FLC	fuzzy logic controller
GA	genetic algorithm
GM	global maximum
GMPP	global maximum power point
HC	hill climbing
HPF	high pass filter
IAE	integral absolute error
IC	incremental conductance
LBS	Lyapunov based switching
LBS-ESC	Lyapunov based switching extremum seeking control
LPF	low pass filter
LTI	linear time invariant
LTV	linear time varying
MIMO	multiple-input multiple-output
MPC	model predictive control
MPP	maximum power point
MPPT	maximum power point tracking
NN	neural network
NN-ESC	neural network extremum seeking control
OCV	open circuit voltage
PCU	power conditioning unit
PESC	perturbation extremum seeking control

PEM	polymer electrolyte membrane
PEM-FC	polymer electrolyte membrane fuel cell
PESC	perturbation based extremum seeking control
PID	proportional integral derivative
PO	perturb and observe
PSU	power supply unit
PV	photovoltaic
RUL	remaining useful life
SCC	short circuit current
SDP	state dependent parameter
SDP-ESC	state dependent parameter extremum seeking control
SISO	single-input single-output
SM-ESC	slide mode extremum seeking control
SSE	sum squared error
TEG	thermoelectric generator
TEM	thermoelectric module
VBS	variance based switching
VBS-ESC	variance based switching extremum seeking control
VPO	Van der pol oscillator
VPO-ESC	Van der pol oscillator based extremum seeking control

Notation

Latin variables

$C(s)$	compensator
C_{min}	minimum value of the capacitor
$D_i(s)$	input dynamics of a plant
$D_o(s)$	output dynamics of a plant
d	duty cycle
d_{min}	minimum duty cycle
χ	state vector of nonlinear system
\hat{x}	estimated state x
$f(\hat{x})$	state dependent function
k	integrator gain
k_c	compensator gain
k_d	product of k_c and k
L	inductor
L_{min}	minimum value of the inductor
L_{tem}	length of TE module
g	nonlinear vector
h	output performance map
u	control input
u_c	smooth control law

u_e	estimation error
u^*	control input at extremum point
\tilde{u}	tracking error
\hat{u}	estimated input
R	resistance
V	voltage
V_{ref}	reference voltage
ΔV	incremental voltage
I	current
ΔI	incremental current
P	power
V_{mpp}	voltage at maximum power point
V_k	voltage at time instant k
I_{mpp}	current at maximum power point
I_k	current at time instant k
P_{mpp}	power at maximum power point
P_k	power at time instant k
R_{tem}	module internal resistance
$R_{L(max)}, R_{L(min)}$	maximum and minimum load resistance, respectively
Z	Figure of merit
$e(t)$	noise term
$y(t)$	measured output
y^*	maximum output value
\tilde{y}	tracking output

Greek variables

α	exponential decay positive constant
δ	small positive constant
β	perturbation gain
φ	phase angle
ω	perturbation frequency
ω_h	high pass filter cut-off frequency
ω_l	low pass filter cut-off frequency
ξ	low pass filter output
μ	variance of state \hat{x}
γ	time varying parameter present ratio between α and μ
τ	time constant
κ	high pass filter gain
σ_e	electrical resistivity

Chapter 1

Introduction

1.1 Introduction

In the past few decades, investigation into low carbon technologies (e.g thermo-electric generators (TEGs), photovoltaic (PV) systems, fuel cell (FC) systems, wind turbines, etc.) has seen several advancements. This is attributed to the requirement of green energy and emission reduction. A wide range of research has been conducted on technologies such as material selection, system configuration, development of estimation models, etc. Despite these advances, however, the science of low carbon technologies still remains an open area of research. One area, for example, is the optimisation of the electrical interface between the power source and the load. This electrical interface or power conditioning unit (PCU) includes a DC-DC converter controlled by a maximum power point tracking (MPPT) algorithm to maximise power transfer from the power source to the load. The MPPT is a method to obtain the optimum power generating point for a given system and load. Fig.1.1 illustrates the configuration of a MPPT with low carbon technologies. The need for MPPT algorithms exists mainly for systems with variable outputs such as low carbon technologies, where output power reduction due to load mismatch occurs. As an example, for TEGs, this

power reduction is caused by the variable temperature across the devices during its normal operation. MPPT enables efficient interfacing of TEG and/or PV systems with a DC-DC converter to transfer maximum power at a fixed voltage, which in automotive applications is most often the 12V battery.

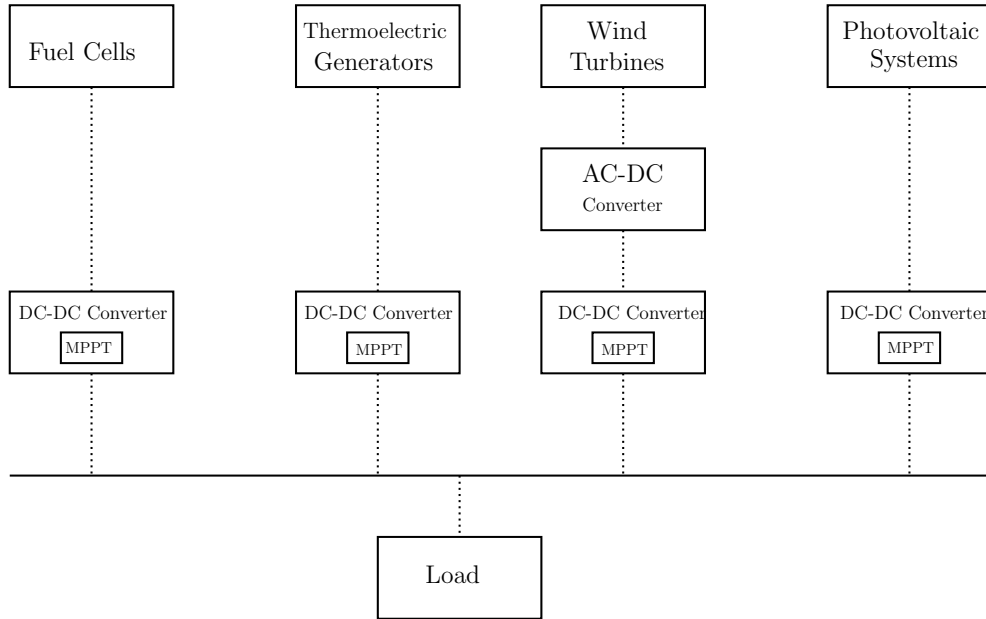


Figure 1.1: Maximum power point tracking configuration with various systems

1.2 Statement of the problem

1.2.1 Local maxima search for mismatch reduction

There are several MPPT techniques for mismatch reduction between the power source (e.g. TEG, PV, FC, etc.) and the load (see Chapter 2). However, there are still problems associated with these techniques, such as the trade-off between convergence/tracking speed and steady-state performance. It is relatively difficult to simultaneously achieve fast convergence speed and optimal performance at a steady state via traditional MPPTs. As an example, perturbation based MPPT techniques attempt to improve the tracking speed by employing a large step-size in

the algorithm. However, this affects the steady-state performance by increasing oscillations at the maximum power point (MPP). On the other hand, hybrid approaches combine offline MPPT methods which provide fast convergence to the MPP, and perturbation based techniques with the use of small step-size to provide fine tuning. Nevertheless, there still are some problems associated with this approach (see Chapter 2). Another problem of MPPT techniques is their limited adaptation capability, mainly due to rapid variations of the power source terminal voltage, which causes most traditional MPPT converters to fail to adapt, leading to a reduction in system efficiency; for example, TEG terminal voltage change due to the variation of temperature between the hot side and cold side of the TEG.

Similar problems arise in PV systems when atmospheric conditions rapidly change. Apart from that, steady-state oscillations arise as a result of continuous perturbation of the terminal voltage or terminal current of the power source. This, consequently, increases power losses and reduces system efficiency. There are three types of steady-state oscillations, namely; forced, conservative, and limit cycles. Forced oscillations are usually referred to as a systematic response whose amplitude and frequency depends on forcing signal amplitude and forcing signal frequency, respectively. The other two types of oscillations (i.e. conservative, limit cycle) are types of behavioral modes of unforced systems. While conservative forced oscillations are an initial condition dependent periodic mode occurring in nondissipative systems, a limit cycle is an initial condition independent response occurring in dissipative systems. Limit cycles occur in traditional MPPTs such as perturb and observe (P&O), incremental conductance (IC), and extremum seeking control (ESC) are undesirable. For instance, in a standard ESC, limit cycles are caused by the dither signal (e.g sine wave, square wave or triangle) which is applied to seek for an extremum point. Therefore the type of steady-state referred to in this Thesis is known as an undesirable limit cycle.

1.2.2 Global maximum search in the presence of local maxima

Global maximum search in the presence of multiple maxima is still an open problem. Multiple maxima are a problem that commonly occurs in PVs due to the shading effect. When a PV panel is shaded, multiple maxima may occur, hence the MPPT converter may become inefficient by failing to converge to the global maximum. This is due to the fact that most of the traditional MPPTs are based on gradient search techniques. Once the MPPT converter has located the nearest MPP, it converges and oscillates around it. Several studies have been published in this area that utilise stochastic based approaches (reviewed in Chapter 2). These approaches require the pre-training of the system, hence the implementation cost is much higher, as a large memory is required to store these models. Being model dependent, the aforementioned approaches, cannot be applied directly to different systems, since each individual system has its own characteristics. For instance, TEGs are temperature dependent and their power-voltage relation is parabolic whereas PVs are temperature and irradiance dependent and their power-voltage relationship is logarithmic.

1.3 Scope and goals of this Thesis

The main goal of this research is to develop an advanced control scheme for DC-DC converters with application to low carbon technologies. So far, there is no advanced controller MPPT algorithm which addresses all the aforementioned issues in Sections 1.2.1 and 1.2.2 simultaneously. Most of the existing techniques attempt to solve one issue at a time. It has been found through a literature survey that, compared to other MPPTs, ESC is an ideal candidate which can be extended to resolve all of the mentioned issues. The reason for this is the adaptation capability to rapid variation in the terminal voltage of the power

source, as compared to other MPPT algorithms. However, the extension requires the resolution of the following drawback or issues of the standard ESC:

- Limit cycle due to periodic perturbation, which makes it more difficult for the true MPP to be achieved
- Trade-off between convergence speed and minimisation of losses. A small tuning parameter results in a slow convergence speed and also failure to excite the system or plant. On the other hand, a large tuning parameter achieves a fast convergence speed, however this introduces oscillations and losses
- Inability of the ESC to find global maximum search in the presence of local maxima

A DC-DC converter model developed in the MATLAB/Simulink environment serves as a surrogate and is used to develop the scheme performance. To achieve the goals, the models must combine static (very low bandwidth) and dynamic (including medium and high bandwidth) characteristics. Having obtained the converter model(s), an advanced non-model based adaptive control scheme is developed along with the associated re-configurable structures such that can be applied to different power sources as shown in Fig.1.1. To gain confidence in the simulation results, the novel scheme(s) will be validated experimentally using an emulated TEG (power supply unit (PSU) in series with a resistor) as well as a real TEG system. Additionally, in order to address all the issues described in Section 1.2 along with making the developed control scheme suitable for TEGs and PVs working under rapid varying environmental conditions such as temperature and irradiance, the scheme should comprise the following key features:

- ***Non-constraints based***: In order to design a universal advanced control scheme for stand-alone PCU which can be easily applied in several areas without pre-requisite knowledge/pre-training of the system, the MPPT converter should be *non-constraints based* and *self-adaptive*. Only input/output

measurement should be needed for the designer to achieve these objectives. There are some approaches existing, also known as online methods (see Chapter 2), but most of them do not achieve the trade-off between MPP tracking speed and steady-state performance. On the other hand, ESC is a non-model based adaptive controller that can be extended for multi-applications. Therefore, in this Thesis an advanced controller based on the extension of the standard ESC scheme is proposed.

- ***Limit cycle minimisation:*** Most of the commonly used MPPT techniques in the aforementioned power sources tend to enter undesirable limit cycles due to periodic perturbation. Consequently, this increases losses and reduces the overall system efficiency. Limit cycle minimisation is required to increase the efficiency as well as minimising losses. Additionally, limit cycle is associated with ripple currents of the power converter and may cause components such as capacitors and inductors to degrade much faster, hence, limit cycle minimisation may improve the life time of the power converter.
- ***Implementation complexity and cost:*** Most of the MPPT converters which are either inexpensive or easy to implement tend to be inefficient. The idea of this Thesis is to develop a universal MPPT converter that is relatively inexpensive and easy to implement, whilst also being efficient. The scheme developed in this Thesis incorporates the trade-off between implementation complexity, efficiency and cost.
- ***Global maximum search in the presence of local maxima:*** This feature allows the MPPT converter to be used within PV systems and improve their overall efficiency. As compared to other existing approaches, the developed technique is less expensive due to the fact that it is non-constraints based. Additionally, it can be applied to any system or sub-system which requires a global maximum search in the presence of multiple maxima without pre-training of the system.

- **Robust and reliable:** The scheme should be robust and reliable in different operating conditions such as noise, harsh driving conditions, etc. Additionally, it should maintain optimal performance as the system degrades. Most of the model based approaches are inefficient as the system degrades. It should be noted that, the study of controller performance for the degraded system or converter is out of the scope of this Thesis. Limit cycle minimisation however, can be used as an indicator of degradation reduction and reliability.

1.4 List of publications

This Section contains is the list of patents, journals and conference papers published as part of the research work undertaken in this Thesis.

Patents:

- [1] "State dependent electricity controller", *UK patent No. GB1604935.5*

Journal papers:

- [2] Maganga, O., Phillip, N., Burnham, K. J., Montecucco, A., Siviter, J., Knox, A. & Simpson, K. (2014), *Hardware implementation of maximum power point tracking for thermoelectric generators*, Journal of Electronic Materials 43(6), 2293-2300.
- [3] Phillip, N., Maganga, O., Burnham, K. J., Ellis, M. A., Robinson, S., Dunn, J. & Rouaud, C. (2013), *Investigation of maximum power point tracking for thermoelectric generators*, Journal of electronic materials 42(7), 1900-1906.

Conference papers:

- [4] Maganga, O., Sumislawska, M. & Burnham, K.J. (2015) *Review of a model free adaptive extremum seeking control for maximum point tracking*, 24th

International Conference on Systems Engineering (ICSE), Coventry, UK, September, 2015.

- [5] Phillip, N., Maganga, O., Burnham, K.J., Dunn, J., Rouaud, C., Ellis, M. & Robinson, S. (2012), *Modeling and simulation of a thermoelectric generator for waste heat energy recovery in low carbon vehicles*, in Environment Friendly Energies and Applications (EFEA), Newcastle, UK, pp. 9499.
- [6] Maganga, O., Larkowski, T. & Burnham, K.J. (2012), *Model complexity reduction of a DC-DC buck-boost converter*, 22nd International Conference on Systems Engineering (ICSE), Coventry, UK, September 2012
- [7] Maganga, O., & Burnham, K.J. *Modeling and control of a waste heat energy recovery system utilising maximum power transfer for hybrid electric vehicles*, Proceeding of 2nd International Conference on Mechanical and Industrial Engineering (MIE), Arusha, Tanzania, 2012.

1.5 Original contributions

A list of original contributions by the author as a part of the research work undertaken in this Thesis is presented in this section. References in square brackets refer to contributions listed in Section 1.4, these are listed in order of their importance as perceived by the author.

- *An improved ESC scheme known as the state dependent parameter extremum seeking control (SDP-ESC) with the benefit of reducing limit cycles, improved convergence speed, ability to track the MPP adaptively as well as to preserve stability and simplicity of the standard ESC. SDP-ESC is a universal self-adaptive control scheme that can be applied in various systems/sub-systems (TEGs, PVs, FCs, wind turbines, etc.) to maximise output power without requirement for a cost function or knowledge of the*

system. The only limitation of the SDP-ESC is its inability to search for the global maximum in the presence of local maxima, therefore, it is suitable for local maxima search. (Chapter 4).

- Following the limitation of the SDP-ESC for global maximum search, an extended SDP-ESC scheme is developed (Chapter 5). The scheme is capable of searching for the global maximum in the presence of local maxima and can be applied to both TEG and PV systems. It is able to locate the global maximum quickly (within seconds) and is less expensive compared to stochastic based approaches.
- A simplified scheme for limit cycle minimisation is known as variance based switching (VBS) ESC. This scheme is a simplified version of Lyapunov based switching (LBS) ESC, it also preserves the simplicity of a standard ESC. Similar to the SDP-ESC it can be applied to the aforementioned power sources. It is also suitable for local maxima searches (Chapter 3).
- Simulation study for application of the ESC within TEGs. The application of the ESC within TEG was presented as part of this research for the first time and published in [3]. A well-known perturb and observe P&O served as a benchmark (Chapter 6).
- Simulation study of the SDP-ESC within TEGs, whereby standard ESC and Lyapunov based switching (LSB-ESC) serves as a benchmark (Chapter 6).
- Experimental validation (Phase I) which validates simulation results of the ESC application to the TEG which was presented in [3]. In this phase, for the first time, ESC was implemented in the actual TEG and thereafter published in [2] (Chapter 7).
- Following limitations of the standard ESC observed in experiment phase I and superior simulation results of the SDP-ESC over the standard ESC. Experimental validation (Phase II), which compares, various MPPT controllers such as P&O, ESC, LBS-ESC, VBS-ESC and SDP-ESC is pre-

sented (Chapter 7).

1.6 Outline of the Thesis

This section gives a brief description of the chapters forming this Thesis. A generalised review of MPPT algorithms used in a wide range of applications such as TEGs, PVs, FCs, etc., is presented in Chapter 2.

State of art of ESC, as well as the methodological background concepts, upon which this Thesis is based, are introduced in Chapter 3. This comprises fundamental understanding of the ESC feedback loop such as learning time scale, averaging, gradient search, ESC designing procedures and limit cycle minimisation. Also, in this Chapter a simplified scheme known as variance based (VBS)-ESC for limit cycle minimisation is proposed. The VBS-ESC is compared with other ESC schemes for limit cycle minimisation, such as LBS-ESC.

Chapter 4 presents an improved ESC scheme known as SDP-ESC. Stability analysis of the SDP-ESC is presented to demonstrate the ability of the proposed scheme to preserve stability. Also, the ability to reduce limit cycles, and improve the convergence speed as compared to the standard ESC is demonstrated, using linear time invariant (LTI) and linear time varying (LTV) examples. Moreover, the design procedure for the proposed SDP-ESC scheme is discussed.

In Chapter 5, an extended SDP-ESC scheme for the global maximum search in the presence of local maxima is presented. Various polynomials with multiple maxima (emulate shading effects in PV systems) are used as surrogates to demonstrate the extended SDP-ESC performance, such as time taken, to converge to the global maximum power point(GMPP).

Chapter 6 is concerned with a simulation study to investigate the performance of the SDP-ESC in comparison to other MPPT algorithms such as P&O, ESC, LBS-ESC, VBS-ESC and SDP-ESC. A simplified TEG model is used for

MPPT performance at transients and steady-state.

Subsequently, in Chapter 7, two phases of experimental validation for the MPPT algorithms are presented. Phase (I) demonstrates performance of the current existing MPPT algorithms and their limitations. In this phase, three different analyses are presented: steady-state, transient using emulated TEG (power supply unit (PSU) connected in series with a resistor), and transient via actual TEG. Steady-state analysis is conducted to determine limit cycles as well as losses. On the other hand, transient analysis using emulated TEG aimed to test the performance of MPPT algorithms and their adaptation capability under rapid variations of terminal voltage. Based on similar analysis as in phase (I), phase (II) presents improved results with the use of the SDP-ESC. The performance of the SDP-ESC is compared with all MPPT algorithms presented in phase (I).

Chapter 8 Provides conclusions on a chapter by chapter basis of the overall achievements of the Thesis and also discusses items for further-work. Fig. 1.2 illustrates a structural representation of a logical flow of the Thesis.

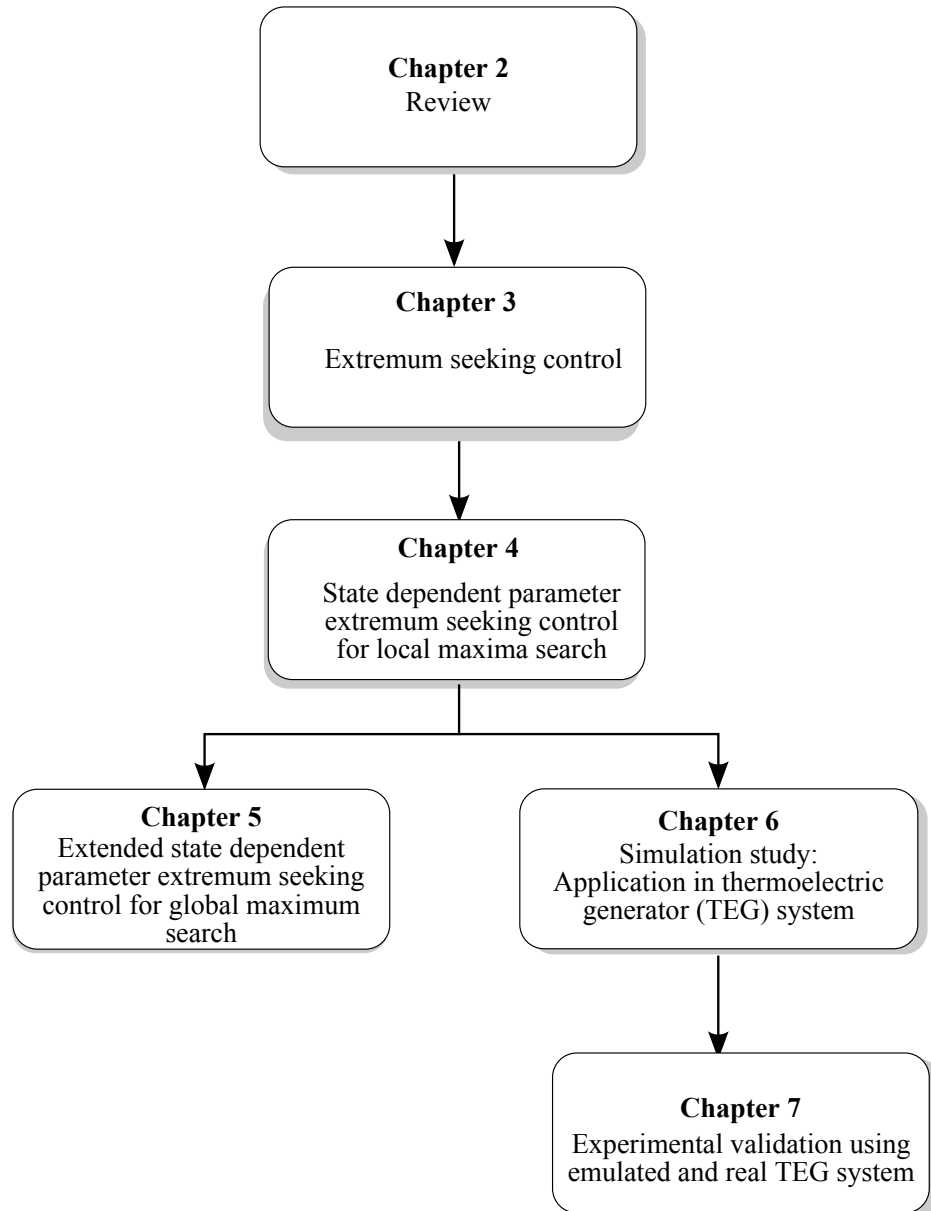


Figure 1.2: Structural representation of a logical flow of the developments of this Thesis

Chapter 2

A review of maximum power point tracking algorithms

2.1 Introduction

A power conditioning unit (PCU) is essential in a system which comprises unstable heat sources and loads. Fig. 2.1 illustrates the block diagram of the PCU considered in this Thesis. The output of the power source is connected to the DC-DC converter and the output of the converter is connected to the DC load or 12V battery. Voltage and current measurements taken from the power source are applied to the maximum power point tracking (MPPT) controller as inputs and pulse width modulation as an output. The MPPT controller is implemented within a PCU (see Fig. 2.1) to alter the operating point of the power source in order to extract the maximum available power. This power is transferred to a DC load, or most often a 12V battery in automotive applications. Some of the MPPT algorithms do not require any prior knowledge, whereas input/output measurements are sufficient to find the maximum power point (MPP). Such algorithms include: perturb and observe (P&O), incremental conductance (IC), and extremum seeking control (ESC). Since the contribution of this Thesis is based on

extensions of the ESC, this method is therefore reviewed separately in Chapter 3. Also, some MPPT algorithms such as open-circuit-voltage (OCV), short-circuit-current(SCC) and artificial intelligence (AI) require prior training or knowledge of the power source to generate control signals. Moreover, some algorithms, also known as hybrid methods utilise both algorithms; i.e.-', those which do or do not require prior knowledge, to search for the MPP. This Chapter is organised as follows; Section 2.2 presents the literature survey of aforementioned MPPT algorithms. In Section 2.6 hybrid techniques are reviewed. Sections 2.7 and 2.8 present comparative performance evaluations and critical analysis of the MPPT techniques, respectively.

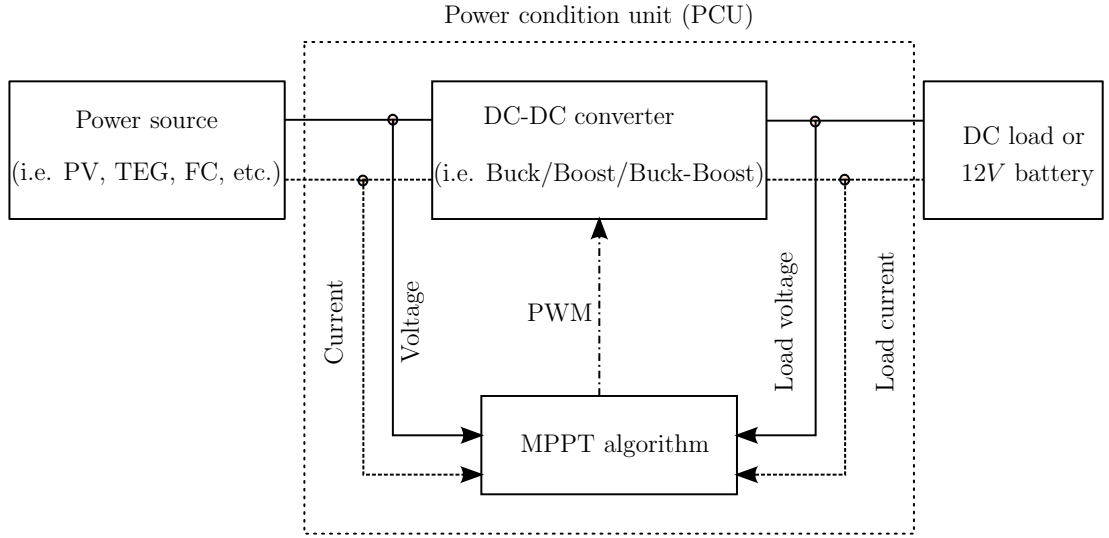


Figure 2.1: Power conditioning unit (PCU)

2.2 Perturb and observe (P & O)/ Hill climbing

P&O works in a similar manner to the hill climbing (HC) algorithm (Reisi, Moradi & Jamasb 2013, Kamarzaman & Tan. 2014). HC uses the perturbation of reference variables such as duty cycle, current or voltage to search for the MPP. While the P&O is based on the power-voltage(P-V) or power-current(P-I) relationship,

HC is based on the power-duty cycle (P-D), as compared to other MPPT algorithms, P&O is most widely used in practical applications. It is also used as the benchmark controller by most researchers due to its simplicity of implementation (Phillip, Maganga, Burnham, Dunn, Rouaud, Ellis & Robinson 2012).

Fig. 2.2 illustrates a flow chart of the most commonly used P&O algorithm which works as follows: Current and voltage (i.e. I_k and V_k) at time instance k are sensed and used to compute current power P_k . Current power P_k is compared to the power at the previous time instance P_{k-1} . If P_k is greater than P_{k-1} and current voltage V_k is also greater than V_{k-1} , it indicates that the power point is moving toward the MPP, hence duty cycle d will be increased by step-size C . However, if V_k is less than V_{k-1} it implies the power point is moving away from the MPP, therefore d will be decreased by C . Also, if P_k is less than P_{k-1} and V_k is greater than V_{k-1} it indicates that the power point is moving away from MPP, therefore d will be decremented by C . On the other hand, if P_k is less than P_{k-1} and V_k is less than V_{k-1} it indicates that the power point is moving towards the MPP, therefore d will be incremented by C .

As compared to the MPPT algorithms for PV systems, development of MPPTs for TEGs is still immature. As an example, early research on MPPTs for the TEGs utilising P&O algorithm emerged more than a decade ago (Nagayoshi, Kajikawa & Sugiyama 2002, Eakburanawat & Boonyaroonate 2006, Nagayoshi & Kajikawa 2006, Nagayoshi, Tokumisu & Kajikawa 2007). In Eakburanawat & Boonyaroonate (2006), the battery voltage is considered to be constant and the MPP is obtained via current measurements only. Also, Eakburanawat & Boonyaroonate (2006) present the comparison of battery charging in three different methods, namely: directly, with a fixed duty cycle and MPPT utilising P&O algorithm. It has been claimed that, the efficiency of the MPPT converter increased by 15% when P&O is used. Nagayoshi & Kajikawa (2006) and Nagayoshi et al. (2007) presented P&O with the use of the buck-boost converter within a

Figure 2.2: A flow chart algorithm for perturb and observe (P&O)
(Reisi et al. 2013)

PCU. The MPPT efficiency of the system however was not specified. Further advancement of MPPT converters utilising P&O algorithms for TEG appeared in the following: (Kim & Lai 2008, Vieira & Mota 2009, Champier, Favarel, Bdcarrats, Kousksou & Rozis 2013). Kim & Lai (2008) present a modified P&O which utilises the voltage/current compensator. The prime function of the compensator is to continuously loop back input measurements (current and voltage), and the output voltage error to adjust the input reference current to capture maximum available power from the TEG. Kim & Lai (2008) used a power supply unit (PSU) connected in series with a resistor to emulate a TEG. MPPT efficiency however was not evaluated in their work. In Vieira & Mota (2009), benefits of using MPPT within the PCU were presented and the harvested energy increased by 34% as compared to when TEG is connected directly to the load. Champier et al. (2013), achieved approximately 99% MPPT efficiency by utilising a boost

converter and the P&O within the PCU. Despite its simplicity and low implementation cost, the major drawback of the P&O is its inability to track the MPP effectively when rapid variations occur (e.g. irradiance variation in PV systems or hot side and cold side temperatures in TEGs). Also, continuous perturbations make P&O oscillate around the MPP, hence the algorithm fails to converge to the actual MPP. More research has been conducted on improving the tracking ability of the P&O/HC as well as reducing the steady-state error (limit cycle minimisation) by utilising adaptive (variable) step-size (Xiao & Dunford 2004, Wai, Wang & Lin 2006).

The idea behind variable step-size is that large step-size is used to allow fast convergence when the operating point is far away from the MPP. On the other hand, when the operating point is close to the MPP, small step-size is used to reduce steady-state error. Xiao & Dunford (2004), achieved a variable step size by introducing a auto-tuning parameter and control mode switching. The control mode switching in Xiao & Dunford (2004) aimed to eliminate the deviation from the MPP when rapid variations of power source (i.e. temperature, irradiance) occurs. In Wai et al. (2006), adaptive step-size is based on incremental reference voltage and only the trade-off between transients and steady-state error was targeted. It has been reported in Moradi & Reisi (2011) that,- despite utilising a variable step-size to overcome the trade-off between transient and steady-state responses, when the system operating point changes quickly, the algorithm may fail to converge to the actual MPP.

2.3 Incremental conductance

This method is based on slope finding and utilises the fact that the slope is calculated as the derivative of power with respect to voltage as zero at the MPP (Reisi et al. 2013). For a voltage smaller than that of the MPP, the slope is

positive. On the other hand, when voltage is greater than that at the MPP, this slope is negative, i.e:

$$\frac{\partial P}{\partial V} = 0, \text{ at MPP} \quad (2.1a)$$

$$\frac{\partial P}{\partial V} > 0, V < V_{mpp} \quad (2.1b)$$

$$\frac{\partial P}{\partial V} < 0, V > V_{mpp} \quad (2.1c)$$

where P and V denote power and voltage, respectively, I denotes the source current, and V_{mpp} is the voltage at the MPP. Fig. 2.3 illustrates the P-V curve with respect to the power voltage relationship presented in (2.1). From (2.1a) it follows that the derivative of MPP with respect to voltage is:

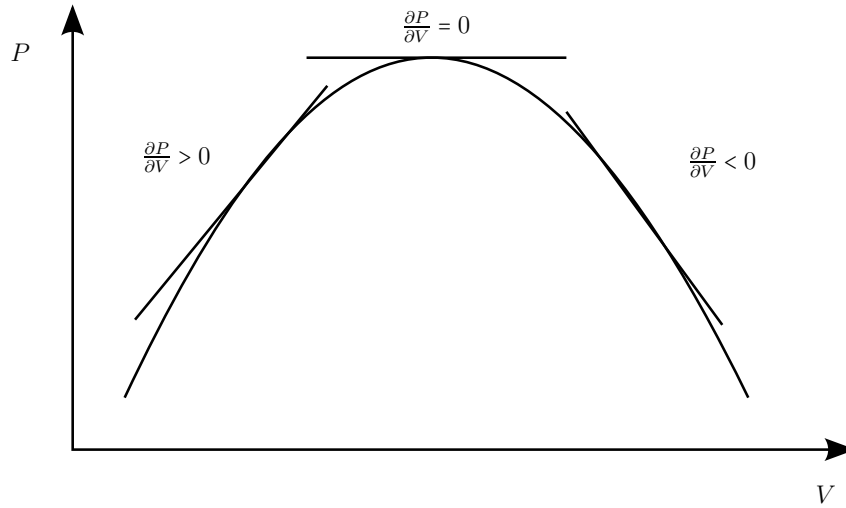


Figure 2.3: Curve for Power Vs Source voltage

$$\frac{\partial P}{\partial V} = \frac{\partial(IV)}{\partial V} = 0 \quad (2.2a)$$

$$\frac{\partial P}{\partial V} = I + V \frac{\partial I}{\partial V} = 0 \quad (2.2b)$$

$$\frac{\partial I}{\partial V} = \frac{-I}{V} \quad (2.2c)$$

$$\frac{\partial I}{\partial V} \approx \frac{\Delta I}{\Delta V} = \frac{-I}{V} = -\frac{I_{mpp}}{V_{mpp}} \quad (2.2d)$$

where, I_{mpp} denotes current at the MPP. ΔI and ΔV denotes incremental current and incremental voltage, respectively, which are given as

$$\Delta I = I_k - I_{k-1} \quad (2.3a)$$

$$\Delta V = V_k - V_{k-1} \quad (2.3b)$$

where, I_k and I_{k-1} denotes current and previous values of current (A), respectively. V_k and V_{k-1} denotes current and previous values of voltage (V), respectively. The point at the left and right of the MPP is given as,

$$\frac{\Delta I}{\Delta V} > \frac{-I}{V}, \text{ at left of MPP} \quad (2.4a)$$

$$\frac{\Delta I}{\Delta V} < \frac{-I}{V}, \text{ at right of MPP} \quad (2.4b)$$

where, $\frac{I}{V}$ denotes the measured conductance of the power source and $\frac{\Delta I}{\Delta V}$ denotes the incremental conductance of the power source. The flow chart in Fig. 2.4 illustrates the most commonly used IC algorithm (Liu, Duan, Liu & Xu 2007, Esham & Chapman 2007, Laird, Lovatt, Savvides, Lu & Agelidis 2008, Reisi et al. 2013).

IC work as follows: First, current and voltage (i.e., I_k and V_k) at time instance k are sensed and used to compute ΔI and ΔV . If $\Delta V \neq 0$ and $\frac{\Delta I}{\Delta V}$ is equal to $\frac{-I}{V}$, based on (2.2d), it indicates that the MPP has been reached, hence previous values for current and voltage (i.e. I_{k-1} and V_{k-1}) will be updated with new values (i.e. I_k and V_k). Or else if $\Delta V \neq 0$ and $\frac{\Delta I}{\Delta V}$ is greater than the $\frac{-I}{V}$ based on (2.4a), it indicates current power point is on the left side of the MPP (see Fig. 2.4) therefore voltage and current at which power source is forced to operate (i.e., reference voltage or rated voltage for the sources denotes V_{ref}) must be incremented or perturbed by the small step-size denoted by C . On the other hand, if $\frac{\Delta I}{\Delta V}$ is less than $\frac{-I}{V}$ based on (2.4b), it indicates the power point is at



Figure 2.4: A flow chart algorithm for incremental conductance (IC)
(Reisi et al. 2013)

right side of the MPP therefore V_{ref} must be decremented by C . Also, if $\Delta V = 0$ and $\Delta I = 0$ based on (2.1a) it implies the power point is exactly at the MPP, hence previous values of current and voltage will be updated with present values (see Fig. 2.4). Moreover, if $\Delta V = 0$ and $\Delta I > 0$ it indicates power point is at right side of the MPP therefore V_{ref} must be decremented by C followed by updating the I_{k-1} and V_{k-1} values (see Fig. 2.4). Furthermore, if $\Delta V = 0$ and $\Delta I < 0$ it implies the power point is at the left side of the MPP hence V_{ref} will be incremented to allow the power point to move towards the MPP followed by updating I_{k-1} and V_{k-1} . The convergence speed of IC depends on C . A large value of C indicates fast convergence, however this reduces the accuracy of IC on tracking the MPP. Some research has been done to improve the convergence speed and the accuracy of the standard IC, particularly in application to PVs, see (Lee, Bae & Cho 2006, Liu et al. 2007). Lee et al. (2006) achieved this by

using a variable increment or decrement denoted by $C(k)$ with similar a concept as the one used in (Xiao & Dunford 2004, Wai et al. 2006). Convergence speed is achieved by selecting a large $C(k)$ while the operating point of the source is away from the MPP and a small $C(k)$ is chosen when the operating point of the source is relatively close to the MPP (Liu et al. 2007). The standard IC and the adaptive IC are based on the assumption that the MPP will be reached when the slope equal to zero, which is not feasible in practice (Laird et al. 2008).

2.4 Open circuit voltage/short circuit current

2.4.1 Open circuit voltage

There are several open circuit voltage (OCV) algorithms for the MPPT with application to low carbon technologies (Cho, Kim, Park & Kim 2010, Kim, Cho, Kim, Baatar & Kwon 2011, Schwartz 2012, Montecucco, Siviter & Knox 2012, Laird & Lu 2013, Kamarzaman & Tan. 2014, Eram & Chapman 2007). The idea behind OCV methods is to find the voltage at the MPP via OCV measurements, denoted V_{oc} . This approach is based on assumption that V_{oc} is linearly related to voltage at the MPP and is presented as

$$V_{mpp} \approx aV_{oc} \quad (2.5)$$

where a is an empirically derived parameter based on V_{oc} and V_{mpp} measurements in different environmental conditions. The flow chart in Fig. 2.5 depicts commonly used OCV method which work as follows: initially, the power source is isolated from the load and V_{oc} measurements are recorded. Using the relationship shown in (2.5), the voltage at the MPP is evaluated. V_{oc} measurements are obtained by repeating this process periodically. It is difficult to determine optimal value of a , however, there is a suitable range for this parameter. For instance,

in PV applications a range from 0.73 to 0.80 (Kamarzaman & Tan. 2014, ESRAM & Chapman 2007). On the other hand, in thermoelectric generator (TEG) applications a is 0.5, hence the OCV for the TEGs is termed as fractional OCV (Schwartz 2012, Montecucco, Siviter & Knox 2012, Laird & Lu 2013, Montecucco & Knox 2014).

This material has been removed from this thesis due to Third Party Copyright. The unabridged version of the thesis can be viewed at the Lanchester Library, Coventry University.

s

Figure 2.5: A flow chart of open circuit voltage method
(Reisi et al. 2013)

Despite its simplicity and low cost of implementation, the actual MPP may not be accurately tracked for both applications (PV/TEG). The reason is the assumption that V_{oc} and V_{mpp} are linearly related, which is unrealistic (Laird et al. 2008), hence true the MPP can not be achieved. Both the OCV and the fractional OCV suffer from periodic disconnections of the power source from the load to measure the V_{oc} and this may cause the unexpected interference of the circuit operation and lead to more losses.

To overcome this problem, various researchers focused on improving V_{oc}

estimation methodologies (Montecucco, Siviter & Knox 2012, Montecucco & Knox 2014, Park, Lee & Bond 2014). Montecucco & Knox (2014) introduced a switching device across the input capacitor within a synchronous DC-DC buck-boost converter. The V_{oc} measurements are obtained while the added switch is open for a short period. Although it has been claimed that-, the V_{oc} estimation method does not require the disconnection of the TEG from the load, this method has several drawbacks: firstly, the circuit comprises of an additional switch in the power converter which increases control complexity as well as the cost. Along with control complexity, switching devices are one of the major cause of failures in power converters (Yang, Xiang, Bryant, Mawby, Ran & Tavner 2010), hence adding more switches may result in the deterioration of reliability. Apart from that, the frequency of V_{oc} measurements is determined by a specific design parameter, hence the accuracy is highly dependent on the designer's experience. Therefore the accuracy of the OCV method proposed by Montecucco & Knox (2014) is arguable.

In (Park et al. 2014), a TEG OCV based MPPT controller has been used to extract the maximum power available from the TEG. This method is a feed forward MPPT controller which utilises temperature measurements of the hot side and cold side ends of the TEG to evaluate the MPP. The V_{oc} measurements with respect to the temperature gradient are used to generate reference voltage. The DC-DC converter is used to regulate the TEG output at this voltage to extract the maximum power available. The MPP is achieved with 1.15% tracking error is presented. The proposed method is claimed to be simple, inexpensive and more reliable as compared to other MPPT approaches for the TEG. This is not necessarily true as it requires a TEG model to search for the MPP. Therefore accuracy is highly dependent on the TEG model; and it is also expensive. Another work on the fraction OCV method has been presented by Youn, Lee, Wee, Gomez, Reid & Ohara (2014) whose paper is a response to recent publications concerning the

effectiveness of impedance matching techniques for the MPP search. Youn, Lee, Wee, Gomez, Reid & Ohara (2014) analytically justify that the V-I characteristic curve is approximately linear. It is argued that, impedance matching approach can still be used as an effective way to evaluate the MPP.

2.4.2 Short circuit current

The short circuit current (SCC) method is very similar to the OCV and is based on the assumption that, the SCC, denoted as I_{sc} , is linearly related to the current at MPP denoted as I_{mpp} . The mathematical relationship between I_{sc} and I_{mpp} is presented as:

$$I_{mpp} \approx \hat{a}I_{sc} \quad (2.6)$$

Similar to the a parameter in the OCV method, \hat{a} is empirically determined and it ranges between 0.8 and 0.9 (for PV applications). As compared to the OCV, the SCC is more efficient and accurate (Reisi et al. 2013). It is however sophisticated to obtain measurements of I_{sc} and, as a consequence, the implementation cost of SCC is usually very high.

2.5 Artificial intelligence methods

Recently, the interest in artificial intelligence (AI) based methods such as the fuzzy logic controller (FLC), the neural network (NN) and the genetic algorithm (GA) for MPPT has shown tremendous growth (Patcharaprakiti, Premrudeepreechacharn & Sriuthaisiriwong 2005, Esham & Chapman 2007, Hiyama, Kouzuma & Imakubo 1995, Elobaid, Abdelsalam & Zakzouk 2012, Messai, Melit, Guessoum & Kalogirou 2011). These methods have been mainly applied in PV systems for global maximum searches in presence of local maxima. Traditional FLC is an offline method in which expert knowledge of the designer is

essential. One of the advantages of the FLC is its ability to work effectively with less accurate mathematical models as well as handling non-linearities (Esram & Chapman 2007). Fixed parameters within the FLC may become inadequate, especially in applications whereby the operating conditions change in a wider range and the expert knowledge is limited. Patcharaprakiti et al. (2005) proposed an adaptive FLC to eliminate this problem by making FLC less dependent on the expert knowledge. The adaptive FLC continuously tunes its membership function and the rule based table, hence it achieves a fast response, and a good performance. However, the computational cost of the proposed method is much higher than that of the traditional FLC due to the inclusion of the learning mechanism. The NN is an off-line method which requires prior training to track the MPP effectively, see,- (Hiyama et al. 1995, Elobaid et al. 2012, Reisi et al. 2013, Kamarzaman & Tan. 2014). Applications of the NN have significantly increased due to its ability to perform nonlinear tasks (Kamarzaman & Tan. 2014). Similar to the FLC, it has been used for a global maximum search in PV systems (Elobaid et al. 2012). In comparison to other methods, the NN does not require any programming it totally depends on the learning process. It can provide accuracy in tracking the MPP without requiring significant knowledge of the power source (e.g TEG/PV). On other the hand, it is only suitable for a particular power source, since different power sources have different characteristics. Also, most power sources are nonlinear in nature (time-varying), hence the NN must be trained regularly to guarantee reasonable tracking performance, which is time consuming. Hiyama et al. (1995) presented the first research work of NN for the MPP search. In (Hiyama et al. 1995), V_{oc} is used as the input and voltage as the output of the NN. The PI controller was used to eliminate any error between the V_{oc} and the output voltage. Elobaid et al. (2012) propose a two stage NN structure. The role of the first stage is to estimate temperature and irradiance from the PV measurements (voltage and current). The second NN stage uses

the estimates of the temperature and the irradiance to determine the MPP. The proposed approach offers the following advantages: it reduces the training set due to its cascaded structure and it does not require temperature or irradiance measurements. In (Messai et al. 2011), GA is used to optimise the FLC by tuning membership functions to optimal values to track the MPP under varying atmospheric conditions. On other the hand, Ramaprabha & Mathur (2011) use GA to optimise the values used to train the NN to track the MPP.

2.6 Hybrid methods

Hybrid methods are mostly used in PV applications (Irisawa, Saito, Takano & Sawada 2000, D'Souza, Lopes & Liu 2005, Kobayashi, Takano & Sawada 2006, Moradi, Tousi, Nemati, Basir & Shalavi 2013, Zhang, Thanapalan, Procter, Carr & Maddy 2013) and are usually comprise of two control loops. The first loop (inner loop) is based on methods which do require prior information and it is dependent on the system (e.g TEG, PV, etc.) variables, see (Fig. 2.6). The prime function of the inner loop is to adapt the fast variation of environmental conditions in order to improve the transient response to converge fast and close to the MPP. The second loop (outer loop) utilises approaches which do not require prior knowledge of the system, aiming to minimise steady-state error to ensure that the algorithm converges to the exact MPP by providing fine-tuning. Fig. 2.6 portrays a generic flow chart of a hybrid methods which comprises two aforementioned loops for set-point calculation and fine tuning.

In (Moradi & Reisi 2011, Zhang et al. 2013), a hybrid method comprising two loops is proposed. The first loop determines the set-point calculations via OCV at a constant temperature. The second loop performs fine tuning utilising a standard P&O algorithm. It has been shown that, the proposed method gives higher accuracy as well as better convergence speed compared to the standard

This material has been removed from this thesis due to Third Party Copyright. The unabridged version of the thesis can be viewed at the Lanchester Library, Coventry University.

P&O. Better convergence speed is achieved due to its ability to pre-determine V_{oc} which allows for the faster evaluation of the V_{mpp} . Although it is difficult for the classic P&O to achieve concurrently fast transience as well as high accuracy, by allowing the standard P&O to converge slowly (keeping amplitude and frequency of perturbation small), the same accuracy as the proposed method can be achieved. Contrary to the method proposed by Moradi & Reisi (2011), Moradi et al. (2013) proposed to take into account the effect of the load and the battery characteristics which are modelled using a Thevenin equivalent circuit in order to

design the offline loop. It has been claimed that, compared to the method proposed in (Moradi & Reisi 2011), the method of Moradi et al. (2013) tracks the MPP efficiently when load variation occurs as well as when the battery degrades. Irisawa et al. (2000) and Kobayashi et al. (2006) proposed a hybrid algorithm that utilises an offline method to allow the PV system to quickly converge close to the MPP and online IC method, to minimise steady-state error, respectively. Fast convergence of these methods is achieved by matching the power converter initial operating point with the load resistance. As compared to other hybrid methods, the proposed method is capable of searching the global maximum in the presence of local maxima and, as a consequence, ensures the actual MPP is effectively tracked when PV system is partially shaded. Efficiency of the MPPT converter was not evaluated in Kobayashi et al. (2006).

D'Souza et al. (2005) proposed a modified P&O that utilises FLC to determine the direction and magnitude of the next perturbation. This approach simultaneously improves both the transient and the steady-state performance. Additionally, the method can achieve a faster transient response by adjusting the duty cycle of the power converter, which forces the operating point toward the MPP as quickly as possible. Benchmark results with the standard P&O was not presented in (D'Souza et al. 2005), hence the significance of the announced improvement is not demonstrated. Jain & Agarwal (2004) proposed a hybrid method that comprises the transient and the steady-state loops. The transient loop is determined by the PV cells dependent parameter which is obtained empirically. As compared to other MPPT methods, in transient, the proposed algorithm tracks this parameter instead of the power; Subsequently, the actual MPP is obtained via fine tuning with the P&O or the IC. In Koizumi & Kurokawa (2005), the offline loop utilises a linear function to identify the neighbourhood of the operating point relative to the MPP, to apply appropriate perturbation. This function is developed from PV cells characteristics. The online loop utilises the IC method.

Shadmand, Balog & Abu Rub (2014) use a hybrid method to improve the performance of the standard P&O. This is achieved by using a model predictive control (MPC) and P&O. The MPC determines the reference current using P&O and uses this current as the input as well as the PV's voltage and current. The MPC predicts the future error, in addition to the next switching state based on the defined optimisation cost function. The result shows that the MPC-MPPT converges faster, compared to the standard P&O. Daraban, Petreus & Morel (2014) proposed a modified GA which utilises P&O. Population size and number of iterations of the traditional GA are reduced by embedding a classic P&O inside the structure of the GA, hence the time required to search for the global MPP is reduced.

2.7 Performance comparison

Depending on the application, the choice of the MPPT technique should be made based on the algorithm's ability to track the actual MPP, its convergence speed, implementation complexity, cost, robustness, reliability and sensitivity. Table. 2.1 summarises different features of the reviewed MPPT algorithms. The OCV and the SCC can be implemented in both analog or digital systems. Both methods have a medium convergence speed and low efficiency. However, implementation of the SCC is more complex and it is more costly compared to the OCV. The NN, the FLC and the GA can be implemented in digital systems only. These methods provide high efficiency. On the other hand, the implementation cost and complexity is high for both methods. P&O with fixed step size can be implemented in digital systems only. Also, it offers high efficiency with low implementation costs. However, it converges slower than the P&O with variable step size. IC can be implemented on digital systems only and has high efficiency. The convergence speed of the IC is highly dependent on step size. Hybrid methods are suitable

for digital systems only. They provide high efficiency and fast convergence speed. The implementation cost however is high. ESC is suitable for both digital and analogue systems. It provides high efficiency and a fast convergence speed with moderate implementation complexity and cost.

Methods	Analogue or Digital?	Convergence speed	MPPT Converter Efficiency	Complexity
Open circuit voltage (OCV)	Both	Medium	Low	Low
Short circuit current (SCC)	Both	Medium	Low	Medium
Neural networks (NN)	Digital	Fast	High	High
Fuzzy logic controller (FLC)	Digital	Fast	High	High
P&O (fixed step-size)	Both	slow	High	Low
P&O (Adaptive step-size)	Digital	Fast	High	Medium
Genetic algorithm (GA)	Digital	Fast	High	High
Incremental conductance	Digital	Depend on step size	High	Medium
Hybrid	Digital	Fast	High	High
ESC	Both	Fast	High	Medium

Table 2.1: Summary of MPPT techniques characteristics

2.8 Critical appraisal and conclusions

The OCV method does not require current sensing therefore it is considered as the least computationally intensive. Also, the voltage at MPP is determined by known empirical values in PVs or by taking half of the open circuit voltage in TEGs. This, however, requires the intermittent disconnection of the power source from the load to establish the prevailing open circuit voltage value. Disconnection of the power source can lead to undesired transients and reduced efficiency. For instance, undesired transients in TEG applications can be due to the operation in dynamic thermal environments. Conversely, IC is able to identify if the MPP has been reached or not, but is computationally intensive and, as a consequence, converges more slowly to the MPP than the OCV. The true MPP cannot be achieved using P&O due to continuous perturbations which cause the operating point to oscillate around the MPP. One disadvantage of the P&O and the IC methods is that for an accurate tracking of the MPP the perturbation gain is required to be small in order to minimise the amplitude of the limit cycle which in turn degrades the algorithm's transient tracking ability. Despite extensions of P&O, OCV, IC and hybrid methods to address the trade-off between transient and steady-state performances, an optimal solution does not yet exist. Also, these methods are suitable only for local maxima searches. NN, FC and GA have shown great success in searching the global maximum in presence of local maxima. However, these algorithms require prior knowledge or training. Since the objective of this Thesis is to create a universal MPPT converter for different aforementioned power sources, model dependent algorithms are not considered here.

To address the deficiencies found for the MPPT algorithms presented in this chapter, the requirement is for an algorithm which can work without disconnecting the power source and load and perform optimally in a transient and steady state

operation as well as search for global maximum. One such algorithm is the ESC, which has shown superior performance to other well-known MPPT methods such as P&O for PV systems (Phillip, Maganga, Burnham, Ellis, Robinson, Dunn & Rouaud 2013). The perceived advantage is attributed to the ability of the ESC to converge more rapidly whilst retaining steady-state performance similar to the P&O method. Therefore, extensions of an ESC for the MPP is proposed in this Thesis.

Chapter 3

Extremum seeking control

3.1 Introduction

This Chapter presents a detailed analysis of perturbation based extremum seeking control (ESC) methods, and a novel simplified scheme for limit cycle minimisation. The novel scheme proposed in this Chapter is known as variance based switching extremum seeking control (VBS-ESC). It achieves limit cycles minimisation based on variance detection of the estimated input. There are different types of ESC schemes, some of which do not require any constraints and some which do require constraints. As compared to constraints based ESC, non-constraints based ESC is considered to be the most favourable option for the MPP search, if negligible parameter uncertainty in the plant or system exists (Guay & Zhang 2003). The main reason for this is that no constraints are imposed on the objective function (Guay 2014). On the other hand, in constraints based ESC, the cost function is considered to be known; therefore, it provides optimal results by quickly identifying the optimum point and converging towards it (Guay & Zhang 2003). Taking into consideration that non-constraints based ESC methods have shown great success in the domain of low carbon technologies, such as FCs, PVs, and most recently TEGs, this Thesis aims to contribute to the domain

of the non-constraints based ESC. However, for the sake of completeness, constraints based ESC is also reviewed in this Thesis. This Chapter is constructed as follows: firstly the state of the art for ESC is presented in Section 3.2, followed by the perturbation (P)ESC feedback loop design in Section 3.3.4. Limit cycle minimisation techniques and an improved scheme for reducing limit cycles are given in Section 3.4.1 and Section 3.4.2, respectively. Section 3.5 presents conclusions and critical appraisals.

3.2 Survey on extremum seeking control

ESC is an approach which seeks the extremum for steady state online optimisation without knowing the plant model and/or the cost function in a closed loop fashion. However, it is assumed that measurements of the plant's input and output signals are available. Early work on ESC goes back to 1922 by Leblanc (1922), where control mechanism that maintain the desirable maximum power transfer was proposed. However, neither mathematical analysis of the scheme's dynamics nor practical evaluation was provided. Despite these limitations, ESC became a powerful and popular tool for either maximising or minimising the unknown output of functions. Significant use of the ESC method occurred between the 1940's to 1960's. For instance, in the early 1940's (during World War II) tremendous research interest in the area of ESC appeared in the Soviet Union. As an example, Kazakevich a Russian PhD student wrote his Thesis titled "*On extremum seeking*". On other the hand, presumably the first English article on ESC was written by Draper & Li (1951), who described ESC and its performance. In the aforementioned article, internal combustion engine optimisation using ESC, or more precisely, a technique for selecting input (ignition timing) to achieve maximum power output was discussed. Generally speaking, most of the ESC research work between 1950's and 1960's emphasized either implementation

of the algorithm (ESC) or explored the algorithm performance for a specific application. Thereafter interest was lost for almost three decades (between 1970's to 1990's) due to the lack of a proof of stability. Nevertheless, ESC gained renewed interest after Krstic (2000) proved local stability for a single-input single-output (SISO) system. The averaging technique and singular perturbations were used to demonstrate that ESC converges to the neighbourhood of the extremum. It was also proven that the neighbourhood is inversely proportional to the perturbation gain, the amplitude and the perturbation frequency of the dither signal used to search for the extremum. Due to its robustness and reliability, non-constraints based ESC has been used in a wide range of applications including: anti-locking brake systems (ABS) (Zhang 2007, Tanelli, Astolfi & Savaresi 2006), control system and optimisation of bio processes (Krstic & Bastin 1999, Guay, Dochain & Perrier 2004, Zhang, Guay & Dochain 2002), proportional integral controller (PID) tuning (Killingsworth & Krstic 2006), flow control problems (Chang & Moura 2009, Kim, Kasnakoglu, Serrani & Samimy 2008), internal combustion engine (Draper & Li 1951, Haskara, Zhu & Winkelman 2006), ESC with limit cycle detector has been applied in subsonic cavity flow (Kim, Kasnakoglu, Serrani & Samimy 2009).

It has also been used to reduce the tuning time of various parameters of the combustion timing controller as well as finding the optimal combustion timing set point (Popovic, Jankovic, Magner & Teel 2006). Moreover, non-constraints based ESC has been used for optimising NN/FLC (Gurvich 2004, Hu & Zuo 2005), autonomous vehicle control and most recently ESC has been applied in TEGs (Phillip et al. 2013, Maganga, Phillip, Burnham, Montecucco, Siviter, Knox & Simpson 2014). Non-constraints ESC can either be based on gradient search or slope seeking. Gradient search is the most commonly used non-constraints based ESC, and usually utilises both the high pass filter (HPF) and the low pass filter (LPF) to calculate the gradient of the cost function. Slope seeking is an extension

of the standard non-constraints based ESC and has attracted significant interest (Ariyur & Krystic 2003, Wiederhold, King, Noack, Neuhaus, Neise, Enghardt & Swoboda 2009, King, Petz & Lemke 2006). This method usually drives the plant to the value of the reference slope of the reference-output map at steady-state. Slope seeking ESC has been applied to improve the aerodynamic performance of axial turbo machine (Wiederhold et al. 2009). This approach has been useful in some applications such as the axial turbo machine, as the peak point between the input-output map is not distinctly visible. Interest in ESC is based on the fact that it is non-constraints based and adaptive. ESC is suitable for situations where non-linearity in the system has a local minimum or local maximum (Ariyur & Krystic 2003).

For example, in TEG applications it finds a set point which keeps the output power of the TEG at the MPP. As compared to other traditional MPPT controllers reviewed in Chapter 2, the ESC controller offers a faster convergence speed and adaptation capability. Within the aforementioned ESC groups there are five different categories which include: slide mode (SM) ESC, neural network (NN) ESC, approximation (AP) ESC, perturbation (P) ESC and adaptive (A) ESC. The main advantage of non-constraints based ESC is that it can be applied to any system where the input-output relationship has local maxima or local minima requiring only minimum knowledge of the actual system. On the other hand, constraints based ESC requires prerequisite-knowledge or information of the system. All non-constraints based ESC are highly dependent on the time separation between the learning and the dynamics to be optimised (Guay 2014). Compared to non-constraints based ESC, constraints based ESC converge to the true peak point. The drawback of constraints based ESC is that it requires a model of the system as well as storage of the models, which make constraints based ESC more expensive compared to non-constraints based ESC.

Perturbation based ESC

Perturbation based ESC (PESC) is the most common and popular ESC in literature (Krstic 2000, Tan, Nei & Mareels 2008, Maganga et al. 2014). As compared to other ESC, PESC allows fast adaptation and it is easy to implement. The PESC depends on external excitation by a continuous perturbation signal (dither signal) to numerically calculate the gradient. A sine wave is most commonly used as the source of perturbation. However, it has been demonstrated by Tan et al. (2008) and references therein that, dither shapes have an impact on convergence speeds. As compared to sinusoidal and triangular perturbations, square wave perturbation leads to much faster convergence. Since the method proposed in this Thesis is based on extensions of PESC, the PESC is therefore analysed in details in the following sections. Since ESC regained research interest in 2000, an improved PESC scheme emerged, see (Krstic 2000, Moura & Chang 2010). Krstic (2000) presents a modified PESC and a generalised framework of PESC for time-varying input.

The modified PESC comprises of a compensator which overcomes the limitation of the standard PESC which strictly require one of the designing parameters (i.e. integrator gain) to be small. The compensator in the modified PESC improves convergence speed compared to the standard PESC. However, similar to the standard PESC, the modified ESC does not converge to the actual MPP. Another improved PESC has been presented by Moura & Chang (2013). In their work, a Lyapunov based switching is added to the standard PESC to minimise limit cycles. PESC has also been extended for global maximum search in the presence of local maxima and is reviewed in detail in Chapter 5. Moreover, PESC has been applied in a wide range of robotics (Calli, Caarls, Jonker & Wisse 2012a, Cistelecan 2008, Ogren, Fiorelli & Leonard 2004). For instance, in (Cistelecan 2008), PESC is used in eye hand arm to maximise the view of the camera by providing an appropriate measurement to the robotic arm. In an ABS

application (Dincmen & Acarman 2012), PESC was applied to search for the extremum point of the tyre force-slip curve. As part of the contribution to their work, the driver steering input was added to the optimisation loop to determine the operation region of the tyres within the characteristic curve between the tyre-force and the slip ratio. In the chilled-water system application (Li, Li, Seem & Li 2013), PESC has been used to minimise the combined energy consumption of the cooling tower fan and the chiller compressor. The performance of PESC was tested under fixed and varying inlet water conditions. Since FC systems also experience variation in the output power due to the variation of internal resistance, tracking the MPP is essential in order to minimise fuel consumption and extract the maximum available power. There are several applications of PESC for the FC systems (Bizon 2010, Bizon 2013, Dan, Bo, Jian, Yi & Yuan 2008). For instance, Bizon (2013) proposed an advanced PESC for MPP search. As compared to the standard PESC, the proposed approach guarantees convergence, a fast tracking speed and fast tracking accuracy.

The advanced scheme uses a band pass filter (BPF) instead of series combination of the LPF and the HPF for gradient search. A gradient estimator within a standard PESC is the key factor in a successful search for the peak point which is normally done using a combination of the LPF and the HPF (Tan, Moase, Manzie, Nesic & Mareels 2010). Henning, Becker, Feuerbach, Muminovic, King, Brunn & Nitsche (2008) presented an improved gradient estimation by the use of the extended Kalman filter (EKF). The main advantage of using the EKF for gradient estimation is that, it uses not only the perturbation signal to estimate the gradient but also the complete input signal (which comprises of an initial input, estimated input and perturbation signal). On the other hand, the standard PESC only uses the initial input and perturbation signal to estimate the gradient (Tan et al. 2010). The main drawback of the gradient estimation based on the EKF is that, the estimate of the gradient is influenced by the closed loop

performance. To overcome this issue Gelberta, Moeck, Paschereit & King (2012) proposed an alternative way to obtain the input which consequently eliminates the influence of the closed loop performance. Gelberta, Moeck, Paschereit & King also extended the application to dual input and single output. Thermo-acoustic instabilities in an atmospheric combustion were used to demonstrate the effectiveness of the proposed scheme by Gelberta, Moeck, Paschereit & King. Benefits of degradation detection in PV systems using square wave perturbation was demonstrated by Lei & Li (2010). When PV systems degrade, the internal resistance changes (i.e. an increase in series resistance and a decrease in shunt resistance). Change in the internal resistance of the PV system due to degradation can affect the rise time in the transient response. Therefore, the change in the rise time is used as a degradation indicator. This benefit however remains inconclusive due to lack of experimental results. Apart from the aforementioned perturbation signals, stochastic signals also have been applied as a source of perturbation (Liu & Krstic 2012, Zhang & Ordonez 2012).

Stochastic based perturbation offers better solutions for systems where predictability associated with the period is difficult (e.g biological systems)(Zhang & Ordonez 2012). For instance, Manzie & Kristic (2009b) and references therein, applied stochastic perturbation to demonstrate its ability to guarantee the convergence of the PESC. Proportional and derivative acceleration terms were incorporated within the feedback loop of a simple PESC to improve the convergence speed (Zhang, Siranosian & Kristic 2009). The modified scheme was applied in Monod and Williams Otto models. Dan et al. (2008), presented PESC for the FC system which uses BPF utilising harmonics of the output signal. It has been stated that inclusion of the third harmonic of the output signal offers better tracking. No benchmark results however were given to demonstrate the effectiveness of the proposed approach. Since the standard PESC is suitable for plants that are open loop stable, Zhang, Siranosian & Kristic (2007) proposed an extension

of the standard PESC to a moderately unstable system based on a phase lag compensator.

Slide mode ESC, Neural network ESC and Approximation based ESC

Early research on the SM-ESC emerged in the 1970s by Korovin & Utkin (1972, 1974) and references therein. Compared to the standard PESC, the SM-ESC is based on a driving signal. This signal is considered as a reference and it is monotonically decreased as the controller converges to the minimum. It is based on the conditions, whereby the SM-ESC tracks the driving signal which decays to a minimum. The SM-ESC by Utkin depends on a high chattering frequency which makes it unsuitable for some applications such as robotics (Calli et al. 2012a). To overcome this problem, Manzie & Kristic (Manzie & Kristic 2009a) and references therein, proposed a different form of control input. The proposed control input is the function of a sine wave and inversely proportional to a tuning parameter which influences the chattering effect. By selecting a large value for the tuning parameter, the chattering effect can be rapidly decreased. The proposed SM-ESC by Manzie & Kristic was applied on ABS systems. Also, SM-ESC is suitable when there are disturbances and uncertainties present in the system (Drakunov, Ozguner, Dix & Ashrafi 1995). Compared to the PESC, excitation of the SM-ESC is done internally. Another scheme of non-constraints based ESC is known as NN-ESC which is based on a minimum peak detector (Hu & Zuo 2005, Hu, Zuo & Li 2006). Similar to SM-ESC, NN-ESC also depends on the reference signal which is monotonically decreased. Like the SM-ESC and the NN-ESC, AP-ESC derives a local representation of unknown function based on past data. AP-ESC uses a gradient based or non-gradient based approach to search for the optimum point (Reisi et al. 2013).

Comparison of non-constraints based ESC

This section summarises the performance of the reviewed non-constraints based ESC methods. Their performance is based on their sensitivity to noise and system dynamics, smooth reference tracking and multivariate extensions. A similar performance is achieved between SM-ESC and NN-ESC when the effect of noise is negligible. However, this is true only when the chattering effect in the SM-ESC is taken into account. The NN-ESC also offers a robust performance due to its hysteresis mechanism, except for small steady state irregularities. SM-ESC is highly sensitive to noise in a transient response and a change in the driving signal causes large amplitudes at steady state. AP-ESC converges much closer to the optimum operating point in the absence of noise. Dynamic effects can cause performance to deteriorate in both, NN-ESC and SM-ESC. In term of SM-ESC, control performance can further be affected by causing the system to drift at steady-state, mainly due to the growth of the driving signal. Since most of the practical systems suffer from noise effect, both SM-ESC and AP-ESC are not the best choices for practical systems.

Compared to all other non-constraints based ESC, it appears that PESC is the least sensitive to noise and is a better choice when the system is affected by measurement noise. However, when applied to systems with negligible measurement noise, its performance (e.g. settling time) reduces significantly. Under the effect of system dynamics, PESC and AP-ESC provide robust performance. On the other hand, SM-ESC and NN-ESC experience minor distortion in the transient. Considering its consistent performance in various circumstances (e.g. noise, system dynamics, multivariate extensions, etc.), PESC has been suggested to be the best choice among the non-constraints based ESC (Calli, Caarls, Jonker & Wisse 2012*b*). Taking account of the findings in the literature, further extension of PESC is proposed in this Thesis.

3.2.1 Non constraints based ESC

Since non-constraints based ESC usually assumes the plant as a black box, this implies some known information of the system or model structure is ignored (Guay & Zhang 2003). This implication can make non-constraints based ESC ineffective for a plant with parameter uncertainties (Guay et al. 2004). There are various research works focused on the design of ESC for plants with parameter uncertainties. These approaches use prerequisite-knowledge of the plant, which allows the determining of parameter uncertainties. When an objective function or a model of the system exists, the controller is referred to as a constraints based ESC. There several research works based on this approach, particularly for bio-processes (Krstic & Bastin 1999, Guay et al. 2004, Zhang et al. 2002) and chemical reactors (Dochain, Perrier & Guay 2011). It is usually difficult to reconstruct the objective function on-line in the presence of parametric uncertainties, hence the true cost can scarcely be calculated. Constraints based ESC considered this scenario in advance, hence making it effective in terms of parameter uncertainties. The proposed scheme guarantees some degree of transient performance whilst achieving satisfactory optimisation when a reasonable objective function is available.

Most of the constraints based ESC methods have been studied for a particular type of plant or system. Having seen the need for a generalised framework for the constraints based ESC, Nesic, Mohammadi & Manzie (2013) proposed a generalised framework for a class of plants with parameter uncertainties. The proposed framework guarantees convergence to the peak point for both static and dynamical systems. The effectiveness of the proposed framework was demonstrated on an ABS example using various estimators. Nesic, Mohammadi & Manzie (2013) also provided a guideline for the parameter tuning of the closed loop ESC. Polymer electrolyte membrane (PEM) FC is a nonlinear time-varying parameter system which makes it difficult to maintain oxygen excess ratio under

all operating conditions. Since the net power of the PEM FC is highly dependent on the oxygen excess ratio in the cathode, the net output power is also affected. To maximise the output of the PEM FC, Chang & Moura (2009) proposed a constraints based ESC. The proposed constraints based ESC incorporated soft constraints based on a quadratic cost function and it is claimed to offer a faster convergence speed to that of the standard PESC.

3.3 PESC concept, analysis and design

This section presents concepts of PESC, detailed analysis and design guidance of the standard PESC scheme. As aforementioned contribution on the Thesis is based on extension of the PESC therefore, analysis presented here can also be found in (Ariyur & Krstic 2010). The concept of PESC is briefly explained followed by the problem description and some key assumptions. Also, the analysis key features of the PESC are included, such as gradient searching, plant dynamics and learning time scale. Gradient search will be presented to demonstrate the ability of the PESC to converge within a small region around the MPP. Also, time scales of plant dynamics and learning time scales will be analysed to investigate time separation between the plant or system and the PESC feedback loop. PESC operates in a closed loop fashion and it comprises a LPF, a HPF, an integrator and a perturbation signal, see Fig. 3.1. The plant or system is considered to be unknown; however it is known that its reference-output map has an extremum point. The gradient search within the PESC is determined by series combination of the HPF and the LPF. The gradient is searched as follows: a perturbation signal with an initial input is modulated and fed to the unknown system. Then the output of the system is filtered through the HPF to remove any DC components. This signal is then demodulated with a perturbation signal and filtered through the LPF to attenuate high frequencies. The initial value of the modulated signal

is then compared with the new value. This is iteratively repeated until the MPP is found at the point which the PESC enters the stable limit cycle. Adaptation within the PESC feedback loop is determined by an integrator gain.

This material has been removed from this thesis due to Third Party Copyright. The unabridged version of the thesis can be viewed at the Lanchester Library, Coventry University.

-

Figure 3.1: Block diagram of perturbation based extremum seeking control (Ariyur & Krystic 2003)

3.3.1 Problem description

Consider a nonlinear system (i.e. unknown system in Fig. 3.1) given as

$$\dot{\chi} = g(\chi, u_c) \tag{3.1a}$$

$$y = h(\chi) \tag{3.1b}$$

where $\chi \in \mathbb{R}^n$ is the state vector, u_c is the smooth control law, $g \in \mathbb{R}^n$ is the nonlinear vector field, h is the output performance map, and $y \in \mathbb{R}$ is the output of the system. Let us assume the smooth control law in (3.1) is known and given as

$$u_c = \Gamma(\chi, u) \tag{3.2}$$

and is parametrised by a scalar input u . It can be stated that the system has been parametrised by u at equilibrium. Also, let us adopt assumptions used in

(Ariyur & Krstic 2010) about the closed loop system in Fig. 3.1.

Assumption 1 *There exists a smooth function $l : \mathbb{R} \in \mathbb{R}^n$ such that*

$$g(\chi, \Gamma(\chi, u)) = 0 \quad (3.3)$$

if and only if $\chi = l(u)$

Assumption 1 signifies that the function is differentiable and the steady-state characteristic is well defined.

Assumption 2 *For each u , the equilibrium $\chi = l(u)$ of the system in (3.1) is exponentially stable*

Assumption 2 ensures that the steady-state characteristic of system in (3.1) is stable.

Assumption 3 *There exists $u^* \in \mathbb{R}$ such that*

$$y' = 0, \quad (3.4a)$$

$$y'' < 0. \quad (3.4b)$$

where $y(u) = h(l(u))$ and scalars $y' = \frac{dy(u^*)}{du}$ and $y'' = \frac{d^2y(u^*)}{du^2}$

Assumption 3 ensures that the steady-state characteristic has a unique maximum (i.e. output equilibrium map $y = h(l(u))$ and is considered to have its maximum point at $u = u^*$). The objective of the PESC is to maximise the steady-state value of y without requiring knowledge of either functions (i.e. h and l) or u^* . Assumptions (1), (2), and (3) were first proposed in (Ariyur & Krstic 2003). A new operator is defined as follows:

Definition 1 $y = F(s)[u]$

It is used to perform different analyses in this Thesis such as gradient search, convergence stability: where the time domain signal y is equal to the time domain signal u filtered with the transfer function $F(s)$. The operator defined in 1 will be used in the remainder of this Thesis.

3.3.2 Gradient search

This section presents a numerical gradient search of the MPP using PESC. For simplicity, the MPP search is considered for a single parameter PESC scheme and the LPF is also removed from the PESC feedback loop (see Fig. 3.2). Prior to the gradient search analysis, let us define the PESC design parameters as shown in Table. 3.1. Output of the high pass filter signal, i.e., $y - \eta$ in Fig. 3.2 is obtained as follows:

This material has been removed from this thesis due to Third Party Copyright. The unabridged version of the thesis can be viewed at the Lanchester Library, Coventry University.

Figure 3.2: Extremum seeking control scheme
(Ariyur & Krstic 2010)

$$\eta = \frac{\omega_h}{s + \omega_h} [y] \quad (3.5a)$$

$$[y] - \eta = [y] - \frac{\omega_h}{s + \omega_h} [y] \quad (3.5b)$$

$$[y] - \eta = \frac{s}{s + \omega_h} [y] \quad (3.5c)$$

Hereafter, high pass filter will be in Fig.3.2 presented using a single block, i.e., $\frac{s}{s+\omega_h}$ where input to the filter will be time domain signal y and output from the filter will be time domain signal $y - \eta$.

A static map of the nonlinear system in (3.1) can be approximated using second order Taylor series expansion as

$$y \approx y^* + \frac{y''}{2} (u - u^*)^2 \quad (3.6)$$

where u is the control input value, u^* is the optimum value at peak, and $y'' < 0$.

	Name	Notation	Unit
	Perturbation gain	β	
	Cut-off frequency of the HPF	ω_h	$\left[\frac{rad}{s} \right]$
	Cut-off frequency of the LPF	ω_l	$\left[\frac{rad}{s} \right]$
	Perturbation frequency	ω	$\left[\frac{rad}{s} \right]$
	Phase angle	φ	$[rad]$
	Integrator gain	k	

Table 3.1: Designing parameters of the PESC

The objective is to minimise the quantity $(u - u^*)$ such that the output function, denoted $f(u)$ approaches its maximum value at y^* (i.e. when $u=u^*$). The estimated value of the unknown u^* is denoted \hat{u} . The perturbation signal $\beta \sin \omega t$ is the input to the plant, which is used for measuring the gradient information of the function $g(u)$. The estimation error of the control input denoted u_e is given

as,

$$u_e = u^* - \hat{u} \quad (3.7)$$

The quantity \hat{u} is modulated by $\beta \sin \omega t$ to obtain u . Note that the difference between u and u^* is given as

$$u - u^* = \beta \sin \omega t - u_e \quad (3.8)$$

Substituting (3.8) into (3.6) the function $h(l(u))$ becomes

$$y \approx y^* + \frac{y''}{2} (u_e - \beta \sin \omega t)^2 \quad (3.9)$$

Expanding (3.9) and replacing $\sin^2 \omega t$ with $\frac{1}{2} (1 - \cos 2\omega t)$ yield to

$$y \approx y^* + \frac{y''}{4} \beta^2 + \frac{y''}{2} u_e^2 - \beta y'' u_e \sin \omega t - \frac{y''}{4} \beta^2 \cos 2\omega t \quad (3.10)$$

The time domain signal y in (3.10) is filtered in order to remove unwanted high frequencies through a high pass filter. The high pass filtered signal becomes

$$\xi \approx \frac{y''}{2} u_e^2 - \beta y'' u_e \sin \omega t - \frac{y''}{4} \beta^2 \cos 2\omega t \quad (3.11)$$

This signal is demodulated by multiplying with a dither signal $\sin \omega t$

$$\xi \approx \frac{y''}{2} u_e^2 \sin \omega t - \beta y'' u_e \sin^2 \omega t - \frac{y''}{4} \beta^2 \cos 2\omega t \sin \omega t \quad (3.12)$$

Replacing the $2\cos 2\omega t \sin \omega t$ term with $(\sin 3\omega t - \sin \omega t)$, the demodulated signal becomes

$$\xi \approx -\frac{\beta y''}{2} u_e + \frac{\beta y''}{2} u_e \cos 2\omega t - \frac{\beta^2 y''}{8} (\sin 3\omega t - \sin \omega t) + \frac{y''}{2} u_e^2 \sin \omega t \quad (3.13)$$

The magnitude of u_e^2 is considered to be small and can be neglected accordingly. Equation (3.13) is then reduced to

$$\xi \approx -\frac{\beta y''}{2}u_e + \frac{\beta y''}{2}u_e \cos 2\omega t - \frac{\beta^2 y''}{8}(\sin 3\omega t - \sin \omega t) \quad (3.14)$$

Equation (3.14) comprises a number of high frequency signals which when passed through the integrator i.e., $\frac{1}{s}[\xi]$, yields to (3.14)

$$\hat{u} \approx -\frac{k}{s} \left[\frac{\beta y''}{2} \right] u_e \quad (3.15)$$

So the derivative of \hat{u} in (3.15) is given as

$$\dot{\hat{u}} \approx -\left(\frac{k\beta y''}{2} \right) u_e \quad (3.16)$$

Given that u^* is constant in (3.7), therefore the derivative of (3.7) is written as

$$\dot{u}_e \approx -\dot{\hat{u}} \quad (3.17)$$

Substituting (3.16) into (3.17) gives

$$\dot{u}_e \approx \left(\frac{k\beta y''}{2} \right) u_e \quad (3.18)$$

Given that $\left(\frac{k\beta y''}{2} \right) < 0$, the system is stable and it can be concluded that $u_e \rightarrow 0$ and \hat{u} converges within a small region of u^* which corresponds to the MPP.

3.3.3 Plant dynamics and learning time scale

The overall PESC feedback loop is considered to have three time scales, namely fastest, medium and slow (Ariyur & Krystic 2003). The plant or system is considered to have the fastest dynamics as compared to periodic perturbation and

filters (i.e. LPF and HPF). On the other hand, periodic perturbation is assumed to have medium dynamics. Filters are considered to have the slowest dynamics. Prior to time separation analysis, let us define how a function can be bounded.

Definition 2 *The big O notation describes the limiting behavior of a function when the argument tends to a particular value or infinity. For example, $O(n^2)$ is any function $g = g(n)$ such that $\left| \frac{g(n)}{n^2} \right|$ remain bounded as $n \rightarrow +\infty$*

In order to analyse the time scale of the PESC scheme, let us begin by determining the overall closed loop system (see Fig. 3.3). The state of the system is given as

This material has been removed from this thesis due to Third Party Copyright. The unabridged version of the thesis can be viewed at the Lanchester Library, Coventry University.

Figure 3.3: Perturbation extremum seeking control
(Ariyur & Krstic 2010)

$$\dot{\chi} = g(\chi, \Gamma(\chi, u)) \quad (3.19)$$

Given that the modulated input $u = \hat{u} + \beta \sin \omega t$, therefore (3.19) can be expressed as

$$\dot{\chi} = g(\chi, \Gamma(\chi, (\hat{u} + \beta \sin \omega t))) \quad (3.20)$$

Also estimated input \hat{u} is obtained when a time domain signal ξ is passed through a low pass filter such that:

$$\hat{u} = \frac{k}{s} [\xi] \quad (3.21a)$$

$$\dot{\hat{u}} = k\xi \quad (3.21b)$$

Output of the low pass filtered signal ξ is determined as follows:

$$\xi = \frac{\omega_l}{(s + \omega_l)} [(y - \eta)] \sin \omega t \quad (3.22a)$$

$$(s + \omega_l) [\xi] = \omega_l [(y - \eta)] \sin \omega t \quad (3.22b)$$

$$\dot{\xi} = -\omega_l [\xi] + \omega_l [(y - \eta)] \sin \omega t \quad (3.22c)$$

Time domain signal y when passed through high pass filter becomes

$$[(y - \eta)] = \frac{s}{(s + \omega_h)} [y] \quad (3.23a)$$

$$s [y] = (s + \omega_h) [(y - \eta)] \quad (3.23b)$$

$$\dot{\eta} = -\omega_h [\eta] + \omega_h [y] \quad (3.23c)$$

Using (3.20), (3.21b), (3.22c) and (3.23c) the overall closed loop system in Fig.3.3 is summarised as

$$\dot{\chi} = g(\chi, \Gamma(\chi, (\hat{u} + \beta \sin \omega t))) \quad (3.24a)$$

$$\dot{\hat{u}} = k\xi \quad (3.24b)$$

$$\dot{\xi} = -\omega_l [\xi] + \omega_l [(y - \eta)] \sin \omega t \quad (3.24c)$$

$$\dot{\eta} = -\omega_h [\eta] + \omega_h [y] \quad (3.24d)$$

ξ term captures the fastest dynamics of system (3.24). The medium fast variations are usually represented by the perturbation signal, i.e., $\beta \sin \omega t$. The learning

process is usually considered to be the slowest and is governed by integrator gain k .

Let us define new coordinate as follows

$$\tilde{u} = \hat{u} - u^* \quad (3.25a)$$

$$\tilde{\eta} = \eta - y(u^*) \quad (3.25b)$$

Using time scale $\tau = \omega t$ and substituting (3.25) into the overall closed system in (3.24), the system can be rewritten as

$$\omega \frac{d\chi}{d\tau} = g(\chi, \alpha(\chi, (\tilde{u} + u^* + \beta \sin \tau))) \quad (3.26)$$

$$\omega \left(\frac{d\tilde{u}}{d\tau} + \frac{du^*}{d\tau} \right) = k\xi \quad (3.27)$$

Given that u^* is fixed parameter for a static map, therefore $\frac{dy(u^*)}{d\tau} = 0$. Equation (3.27) is reduced to

$$\omega \frac{d\tilde{u}}{d\tau} = k\xi \quad (3.28)$$

where k is a design parameter and be selected such that, $k = \omega \delta K'$ (Ariyur & Krystic 2003) where

- ω and δ are small positive constants,
- K' is $O(1)$ positive constant.

Substituting k into (3.28) gives

$$\frac{d\tilde{u}}{d\tau} = \delta K' \xi \quad (3.29)$$

From (3.24c) can be rewritten as

$$\omega \frac{d\xi}{d\tau} = -\omega_l \xi + \omega_l (y - \tilde{\eta} - y(u^*)) \sin \tau \quad (3.30)$$

Given that $y = g(x)$, therefore (3.30) becomes

$$\omega \frac{d\xi}{d\tau} = -\omega_l \xi + \omega_l (h(x) - \tilde{\eta} - y(u^*)) \sin \tau \quad (3.31)$$

From (3.31) ω_l is another designing parameter and can be selected in a similar manner as k , therefore $\omega_l = \omega \delta \omega'_L$ where ω'_L is $O(1)$ positive constant. Substituting ω_l into (3.31) yields to

$$\frac{d\xi}{d\tau} = -\delta \omega'_L \xi + \delta \omega'_L (h(x) - \tilde{\eta} - y(u^*)) \sin \tau \quad (3.32)$$

Also (3.24d) can be rewritten as

$$\omega \left(\frac{d\eta}{d\tau} + \frac{dy(u^*)}{d\tau} \right) = -\omega_h (\tilde{\eta} + y(u^*)) + \omega_h y \quad (3.33)$$

Similarly $y(u^*)$ is fixed parameter, therefore $\frac{dy(u^*)}{d\tau} = 0$. Equation (3.33) is reduced to

$$\omega \frac{d\eta}{d\tau} = -\omega_h (\tilde{\eta} + y(u^*)) + \omega_h y \quad (3.34)$$

Given that $\omega_h = \omega \delta \omega'_H$ where ω'_H is a positive constant. Equation (3.34) can be expressed as

$$\frac{d\eta}{d\tau} = -\omega'_H (\tilde{\eta} + y(u^*)) + \omega'_H y \quad (3.35)$$

Eq. 3.35 can be written as

$$\frac{d\eta}{d\tau} = -\omega'_H \tilde{\eta} + \omega'_H (h(x) + y(u^*)) \quad (3.36)$$

The overall system with time scale $\tau = \omega t$ is summarised using (3.26), (3.29), (3.32) and (3.36)

$$\omega \frac{dx}{d\tau} = g(x, \alpha(x, (\tilde{u} + u^* + \beta \sin \tau))) \quad (3.37)$$

$$\begin{bmatrix} \frac{d\tilde{u}}{d\tau} \\ \frac{d\xi}{d\tau} \\ \frac{d\eta}{d\tau} \end{bmatrix} = \begin{bmatrix} \delta K' \xi \\ -\delta\omega'_L \xi + \delta\omega'_L (h(x) - \tilde{\eta} - y(u^*)) \sin\tau \\ -\delta\omega'_H \tilde{\eta} + \delta\omega'_H (h(x) + y(u^*)) \end{bmatrix} \quad (3.38)$$

From the system in (3.37), based on the assumption that both $\tilde{u} + u^*$ and the perturbation signal, i.e., $\beta \sin\omega t$ are slowly time varying as compared to transients in χ -dynamics, it is possible to obtain the approximate solution of χ as follows

$$x = l(\tilde{u} + u^* + \beta \sin\tau) \quad (3.39)$$

Equation (3.39) can be used to discard fast time response in the χ -dynamics. The time-invariant system which captures the main trend of the learning dynamics can be obtained by averaging out the time variations. For more details in averaging analysis of the PESC feedback loop see (Ariyur & Krstic 2010).

3.3.4 PESC parameter design

This section presents design guidance for a single parameter PESC scheme. The PESC comprises of tuning parameters namely: β , k , ω , ω_h , and ω_l , φ . PESC feedback performance is highly dependent on these parameters. For instance, ω , should be larger with respect to k . However, too large a value for ω may trigger un-modeled dynamics and causes oscillations in the system output Ariyur & Krstic (2003). Also, ω must be large than ω_h and ω_l . On other the hand, ω must have a smaller cut off frequency than the input dynamics to separate the frequencies corresponding to the perturbation signal and the inner dynamics Ariyur & Krstic (2003).

3.4 Limit cycle minimisation

Similar to the other non-constraints based ESC, the PESC also tends to enter a limit cycle within close proximity of the MPP. As a consequence the true MPP can rarely be achieved. Limit cycle minimisation for PESC control have been presented in Wang & Krstic (2000) and (Moura & Chang 2010, Moura & Chang 2013). Wang & Krstic use the Van der Pol oscillator (VPO) to detect and minimise limit cycles. VPO is an dissipative oscillator with a nonlinear damping that dissipates energy at high amplitudes and generates energy at low amplitude. This results in oscillations around a state at which dissipation and generation balance energy (Wang & Krstic 2000). The state at which the oscillations converge is the so called limit cycle. PESC together with VPO it is also called VPO-ESC. Once the PESC enters the stable limit cycle the VPO reduces the amplitude of the output based on the desire of the designer. Contrary to the VPO, Moura & Chang(2013) use a LBS to minimise limit cycles by exponentially decaying the perturbation gain. Both methods for limit cycle minimisation (i.e. VPO and LBS) comprise multiple tuning parameters which increase the optimisation complexity. Since VBS-ESC (the simplified version of the LBS-ESC) also achieves limit cycle minimisation by reducing the amplitude of perturbation gain. A detailed description of the LBS-ESC is given in the following section.

3.4.1 Lyapunov function based switching (LBS) extremum seeking control

This section describes limit cycle minimisation using the LBS-ESC. To minimise limit cycles, Moura & Chang (2010) incorporated a LBS within the PESC feedback loop (see Fig. 3.4). This approach was demonstrated in the PV system. The proposed scheme utilises the LBS exponentially decaying the dither signal amplitude (perturbation amplitude) once the system enters stable limit cycle. The

LBS scheme (see Fig. 3.4) comprises an averaging operator, a quadratic Lyapunov function, a switch and a perturbation signal. The averaging operator is obtained by linearising the entire PESC feedback loop about the MPP. The averaging operator is also referred to as the Jacobian (i.e. average model) that approximates the plant or system dynamics near the equilibrium point. The obtained average model is used to develop a quadratic Lyapunov function denoted by $V(x_\beta)$ to govern the switching process. x_β is the average state variable of the estimated input, LPF output, and HPF output of the PESC feedback loop see Fig. 3.4. x_β is given as

$$x_\beta = \begin{bmatrix} \tilde{u} & \tilde{\xi} & \tilde{\eta} \end{bmatrix} \quad (3.40)$$

where \tilde{u} , $\tilde{\xi}$ and $\tilde{\eta}$ are new coordinates defined based on (3.25). If $V(x_\beta)$ is smaller than the threshold, denoted ϵ_{lbs} , the dither signal with decaying amplitude will be used, otherwise the same dither signal as in the standard PESC will be used. This process will continue until $V(x_\beta)$ drops below ϵ_{lbs} . Once this happens, the integrator resets to its initial condition and the original dither signal will be used. It has been shown in Moura & Chang (2010) that the Jacobian of the closed loop system shown in Fig. 3.4 near the equilibrium is given as

$$J = \begin{bmatrix} 0 & k & 0 \\ \omega_l b_2 \beta_o & -\omega_l & 0 \\ \omega_h b_1 & 0 & -\omega_h \end{bmatrix} \quad (3.41)$$

where, $b_1 = 0$ and $b_2 < 0$. Having obtained the Jacobian of system in Fig. 3.4, the $V(x_\beta)$ used in the LSB is obtained by solving the following Lyapunov equation for P:

$$PJ + J^T P + Q = 0 \quad (3.42)$$

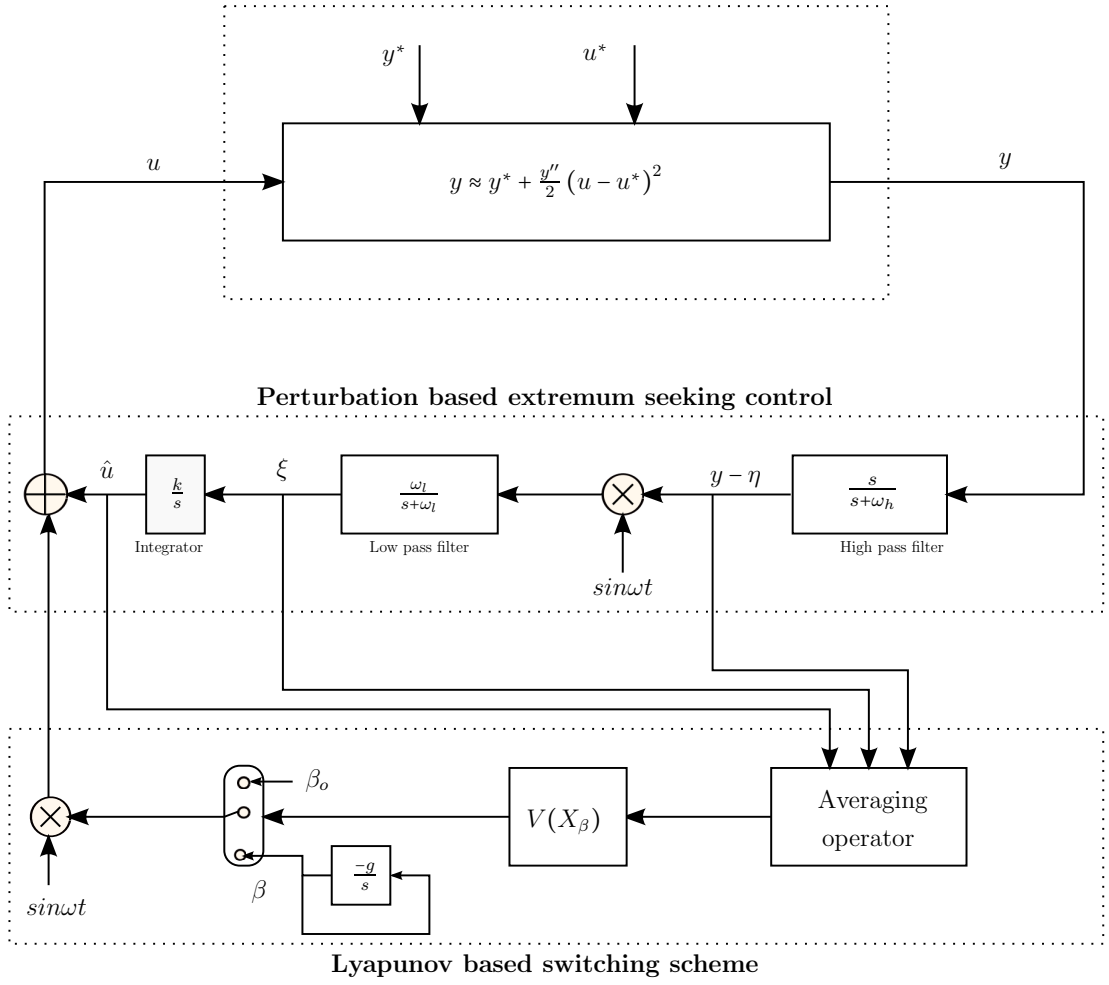


Figure 3.4: PESC with Lyapunov based switching

where Q is considered as the symmetric matrix (i.e. identity). From (3.42), the following Lyapunov function

$$V(x_\beta) = \frac{1}{2} x_\beta^T P x_\beta \quad (3.43)$$

is obtained. $V(x_\beta)$ given in (3.43) is used to develop the control law as follows,

$$u(t) = \begin{cases} \hat{u} + \beta_o \sin \omega t & \text{if } V(x_\beta) > \epsilon_{lbs} \\ \hat{u} + \beta \sin \omega t & \\ \left\{ \begin{array}{l} \frac{d\beta(t)}{dt} = -g\beta(t) \\ \beta(0) = \beta_o \end{array} \right. & \text{Otherwise} \end{cases}$$

where: $u(t)$ denotes the control input signal, \hat{u} denotes the estimated input, β_o denotes the initial perturbation amplitude, β denotes the perturbation amplitude based on exponential decay. Parameters $-g$ and ϵ_{lbs} ensure system stability due to disturbances. $V(x_\beta)$ estimates how close to the MPP the "average model" converges. If $V(x_\beta)$ is within the pre-defined threshold denote ϵ_{lbs} , therefore as $x_\beta \rightarrow 0$ then $V(x_\beta) \rightarrow 0$. As the PESC converges close enough to the MPP, the perturbation signal (i.e. sinusoidal) decays exponentially to zero, hence $u \rightarrow u^*$. However, due to disturbances $V(x_\beta)$ may drift away from the ϵ_{lbs} therefore control law will work as follows: if $V(x_\beta)$ is greater than ϵ_{lbs} then the LBS-ESC will operate as the standard PESC with $u(t) = \hat{u} + \beta_o \sin \omega t$ until the plant converges back to the MPP. On the other hand, if $V(x_\beta)$ drops below ϵ_{lbs} , the integrator will reset the initial condition $\beta(0) = \beta_o$ it will operate with $u(t) = \hat{u} + \beta \sin \omega t$.

3.4.2 Variance Based Switching (VBS) ESC

As aforementioned, both the VPO-ESC and the LBS-ESC comprise multiple tuning parameters, hence this may lead to an increase in complexity for online optimisation. To address these issues, in this Section a simplified VBS-ESC scheme for limit cycle minimisation is proposed (see Fig. 3.5). The proposed scheme is a simplified version of the LBS-ESC and it also retains the simplicity of the PESC. The simplification is achieved by removing the averaging operator hence there is no need for linearising the entire feedback loop. Also, the Lyapunov function integrator within a LBS scheme and its tuning time varying parameter g are removed (see Fig. 3.4). A variance detection sub-system is introduced to minimise limit cycles by detecting variance in the estimated input. The VBS-ESC comprises of the PESC and the VBS scheme (see Fig. 3.5). The VBS is used to reduce the amplitude of oscillations once the PESC has entered stable limit cycle. Detection of the amplitude of oscillations is based on determining the variance of \hat{u} . As the PESC scheme approaches steady-state, the variance of

3.5 Critical appraisal and conclusions

In this chapter, non-constraints based and constraints based ESC have been reviewed. Detailed analysis of several key features of the PESC such as gradient search, learning and dynamic time scale and limit cycle minimisation have been presented. Considering its consistent performance in various circumstances (e.g. noise sensitivity, sensitivity to system dynamics, multivariate extensions, etc.), the PESC has been suggested to be the best choice among the non-constraints based ESC in literature. However, limit cycles due to periodic perturbation makes it more difficult for the true MPP to be achieved using PESC. The improved scheme known as VBS-ESC based on simplification of the LBS-ESC for limit cycle minimisation is presented. VBS-ESC is considered to be simpler based on the following reasons, Compared to the LBS-ESC, it doesn't require linearisation of the entire PESC feedback loop, and it also comprises fewer tuning parameters and it does not require the solving of the Lyapunov function. Although both methods minimise limit cycles in a similar manner, neither of them take into consideration the trade-off between convergence speed and the minimisation of losses. To address these issues an improved PESC scheme known as the SDP-ESC is presented in Chapter 5.

Chapter 4

State dependent parameter (SDP) extremum seeking control

4.1 Introduction

This Chapter presents an advanced control strategy based on an extension of the standard PESC known as SDP-ESC. While the VBS-ESC proposed in Chapter 3 minimises the limit cycle based on variance detection, both the SDP-ESC and the LBS-ESC minimise limit cycles by decaying the perturbation gain exponentially. However, the SDP-ESC approach introduces dependency between the estimated input and perturbation gain which allows the automated exponential decay of the perturbation signal, instead of linearising the entire feedback loop and defining a Lyapunov function as is the case in LBS-ESC. Compared to the LBS-ESC, the SDP-ESC in addition to limit cycle minimisation, also takes into account the trade-off between the convergence speed and the minimisation of losses. For that reason the convergence speed is improved by introducing a compensator (PI controller). Nevertheless, the proposed scheme can be initialised with a large perturbation gain, hence making it possible to achieve the required excitation for the duration of the operation. The main advantages of the SDP-ESC as compared to

LBS-ESC include its simplicity because it does not have a switch (with multiple tuning parameters). It does not require calculating a Lyapunov function as well as not having the need to average the feedback loop. This chapter is organised as follows; intuitive explanation of the proposed scheme is given in Section 4.2. Convergence and stability analysis of the proposed scheme is discussed in Section 4.3 and Section 4.4, respectively. Section 4.5 describes the design procedure of the SDP-ESC for a single parameter scheme. Section 4.6 presents simulation examples for both plant with and without dynamics. The sensitivity analysis of the SDP-ESC is presented in Section 4.7. Section 4.8 presents the critical appraisal and conclusions.

Similar to other traditional ESCs, the PESC also tends to enter a limit cycle due to periodic perturbation. When applied to an MPP search within low carbon technologies (e.g TEGs, PVs, FCs, wind turbines, etc.) the true MPP can hardly ever be achieved. Apart from that, limit cycle is associated with ripple currents across the load and the inductor within DC-DC converter (Chen, Chou & Wu 2005). A large limit cycle indicates high ripple current which can cause the core temperature of the capacitor to rise and hence reduce the electrolyte of the capacitor. Reduction of the electrolyte causes both the capacitance and the equivalent series resistance (ESR) to increase. The ESR is usually used as a health indicator of capacitors (Chen et al. 2005). An increase of the ESR implies the reduction of the remaining useful life (RUL) of a DC-DC converter which may lead to decreased reliability. This justifies the need for a more advanced PESC which can minimise limit cycles, improve convergence speed and reliability whilst preserving the stability and simplicity of the standard PESC.

4.2 SDP-ESC intuitive explanation

The SDP function and the compensator form a modified loop within the PESC. The PESC with the modified loop is shown in Fig. 4.1 and is further referred to as the state dependent parameter (SDP) ESC. It is named SDP-ESC due to the dependence of the perturbation gain parameter on the system state \hat{x} . In this Thesis, the study of limit cycle minimisation and improving speed of convergence via SDP-ESC is considered only for a single parameter scheme in a continuous time domain (see Fig. 4.1). The plant in Fig. 4.1 is considered to have faster dynamics than the SDP-ESC feedback loop. This will ensure that the plant appears as a static non-linearity from the viewpoint of the SDP-ESC feedback loop. A slow perturbation signal will cause time separation between the SDP-ESC feedback loop and the plant and as a consequence the dynamics of the plant will not interfere with the peak seeking scheme. Cut-off frequencies of high and low pass filters are lower than the perturbation frequency ω .

The estimated value \hat{u} of unknown optimal input u^* is modulated with a perturbation signal (sine wave with the gain $f(\hat{x})$) which decays exponentially to a small yet sufficient value to allow the SDP-ESC feedback loop to detect changes in the system input. It should be noted that $f(\hat{x})$ must not be allowed to decay to zero, but rather to a small value close to zero. Allowing $f(\hat{x})$ to decay to zero implies no perturbation to the system and as a consequence, the SDP-ESC will fail to adapt. The rate at which $f(\hat{x})$ decays depends on α . If \hat{u} is on either side of u^* with minimal limit cycle, a periodic response of the output y which is either in-phase or out-of-phase with the perturbation signal will be created. The rate of decay of the perturbation signal depends on the variance of the integrator output \hat{x} . The variance of \hat{x} decays to a small value as the system enters a stable limit cycle. DC components are removed from output y when it passes through the washout filter (i.e. HPF). The output of the filter is then demodulated with a

dither signal (sine wave with a fixed perturbation gain). The LPF removes high frequencies from the demodulated signal. The SDP function should have the slowest dynamics in the closed loop system to allow the SDP-ESC feedback loop via perturbation signal $f(\hat{x})\sin\omega t$ to search for the gradient and reach steady state. Mathematically, $f(\hat{x})$ is expressed as

$$f(\hat{x}) = \begin{cases} \beta e^{\frac{-\alpha}{\mu}} & \text{if } \mu < \alpha \text{ and } \mu \neq 0 \\ \beta & \text{otherwise} \end{cases}$$

where μ is the variance of the state \hat{x} , β is the perturbation gain, $\alpha > 0$ denotes the exponential decay constant. The variance of \hat{x} is calculated as a moving averaging window where the window length is based on a number of samples. Adaptation within the SDP-ESC is achieved via an integrator and a compensator is used to improve the convergence time. As $f(\hat{x})$ decays to a small value the limit cycle is minimised.

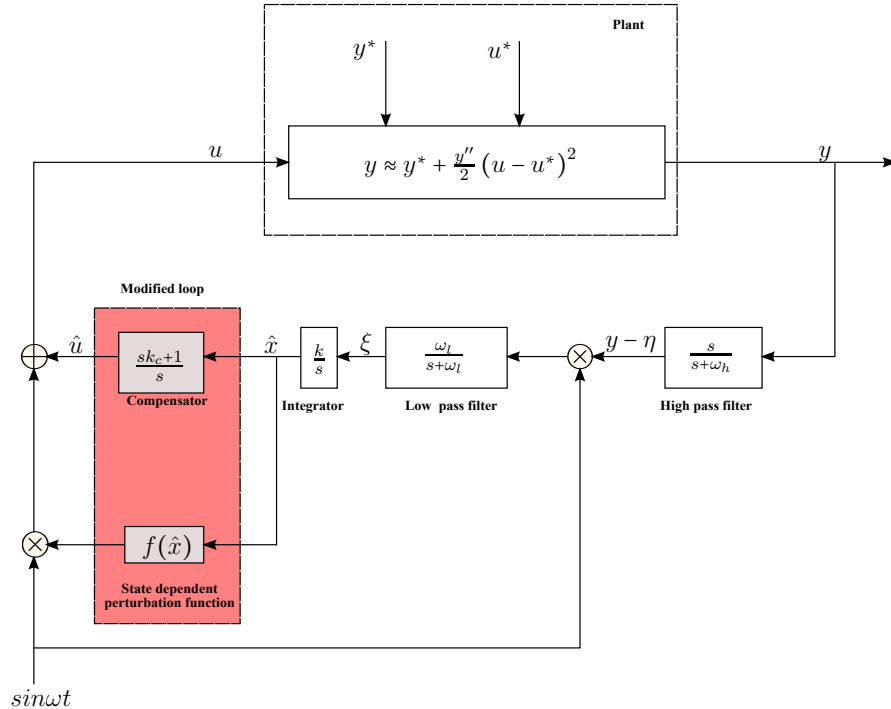


Figure 4.1: Illustrates state dependent parameter (SDP) ESC scheme

4.3 Convergence analysis

It is important to ensure that the developed SDP-ESC scheme is capable of converging to the MPP as well as minimising limit cycles. The convergence analysis using the SDP-ESC is demonstrated using the same problem described in Section 3.3.1. Assumptions 1, 2 and 3 (see Section 3.3.1) are also considered. Convergence analysis for a single parameter SDP-ESC scheme is considered. Before proceeding with the convergence analysis, let us make the following assumption:

Assumption 4 μ is a windowed variance hence γ is considered to be constant for a period of time

Definition 3 γ is a time varying parameter which presents ratio between α and μ

therefore $f(\hat{x})$ can be presented as:

$$f(\hat{x}) = \beta e^{-\gamma} \quad (4.1)$$

4.3.1 SDP-ESC for a static map

Fig. 4.2 presents a simplified form of the SDP-ESC closed loop where the plant dynamics are neglected.

Proposition 1 *The perturbation signal of the system in Fig. 4.2 is sufficiently slow to allow the plant to appear as a static nonlinear map from the SDP-ESC viewpoint. LPF is not essential for convergence analysis since the integrator attenuates high frequencies, however it should be noted that for practical implementation, LPF is required.*

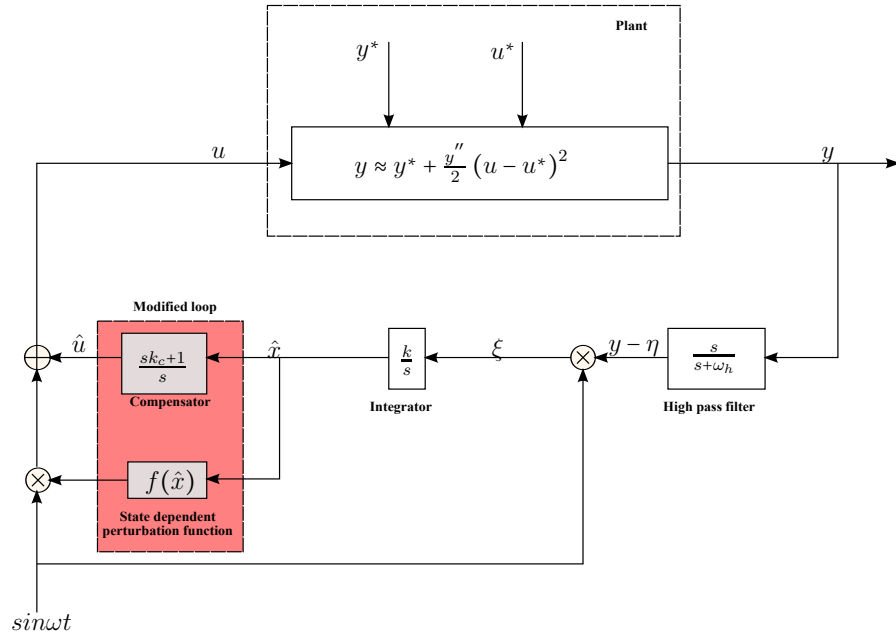


Figure 4.2: Simplified SDP-ESC scheme

Using second order Taylor series expansion, the static nonlinear map of the system in Fig. 4.2 can be approximated as

$$y(u) \approx y^* + \frac{y''}{2} (u - u^*)^2 \quad (4.2)$$

The objective is to minimise quantity $(u - u^*)$, such that $y \approx y^*$.

Denote u_e as the estimation error which is the difference between u^* and \hat{u}

$$u_e = u^* - \hat{u} \quad (4.3)$$

The quantity \hat{u} is modulated by $f(\hat{x})\sin\omega t$ to obtain u . The difference between u and u^* is given as

$$u - u^* = f(\hat{x})\sin\omega t - u_e \quad (4.4)$$

Substitute (4.4) into (4.2) gives

$$y \approx y^* + \frac{y''}{2} (u_e - \beta e^{-\gamma} \sin\omega t)^2 \quad (4.5)$$

Expanding (4.5) and replacing $\sin\omega t$ with $\frac{1}{2}(1 - \cos 2\omega t)$ yield to

$$y \approx y^* + \frac{y'' u_e^2}{2} + \frac{y''}{4} \beta^2 e^{-2\gamma} - y'' u_e \beta e^{-\gamma} \sin\omega t - \frac{y''}{4} \beta^2 e^{-2\gamma} \cos 2\omega t \quad (4.6)$$

The time domain signal y in 4.6 is filtered in order to remove any unwanted slow DC components. The high pass filtered signal becomes

$$\xi \approx \frac{y'' u_e^2}{2} + \frac{y''}{4} \beta^2 e^{-2\gamma} - y'' u_e \beta e^{-\gamma} \sin\omega t - \frac{y''}{4} \beta^2 e^{-2\gamma} \cos 2\omega t \quad (4.7)$$

The signal in (4.7) is demodulated by multiplying with dither signal $\sin\omega t$ to obtain

$$\xi \approx \frac{y'' u_e^2}{2} \sin\omega t + \frac{y''}{4} \beta^2 e^{-2\gamma} \sin\omega t - y'' u_e \beta e^{-\gamma} \sin^2\omega t - \frac{y''}{4} \beta^2 e^{-2\gamma} \cos\omega t \sin\omega t \quad (4.8)$$

Replacing $\cos\omega t \sin\omega t$ with $\frac{1}{2}(\sin 3\omega t - \sin\omega t)$ the demodulated signal in (4.8) becomes

$$\xi \approx \frac{y'' u_e^2}{2} \sin\omega t + \frac{y''}{4} \beta^2 e^{-2\gamma} \sin\omega t - y'' u_e \beta e^{-\gamma} \sin^2\omega t - \frac{y''}{8} \beta^2 e^{-2\gamma} (\sin 3\omega t - \sin\omega t) \quad (4.9)$$

The magnitude of u_e^2 is considered to be small and can be neglected accordingly. Equation (4.9) is then reduced to

$$\xi \approx -\frac{y''}{2} u_e \beta e^{-\gamma} + \frac{y''}{4} \beta^2 e^{-2\gamma} \sin\omega t + \frac{y''}{2} u_e \beta e^{-\gamma} \cos 2\omega t - \frac{y''}{8} \beta^2 e^{-2\gamma} (\sin 3\omega t - \sin\omega t) \quad (4.10)$$

Equation (4.10) comprises a number of high frequency signals which when passed through the integrator i.e., $\frac{1}{s}[\xi]$, yields to 4.11

$$\hat{x} \approx -\frac{k}{s} \left[\frac{e^{-\gamma} \beta y''}{2} \right] u_e \quad (4.11)$$

The approximation of the optimal perturbation signal \hat{u} is obtained by passing the approximated time signal \hat{x} through a compensator, such that:

$$\hat{u} = \frac{sk_c + 1}{s} [\hat{x}] \quad (4.12)$$

substituting (4.11) into (4.12) yields to the approximation of the rate of change of the optimal perturbation signal, i.e.,

$$\dot{\hat{u}} \approx -zk_c u_e - z\dot{u}_e \quad (4.13)$$

where $z = \frac{k\beta e^{-\gamma} y''}{2}$

since u^* is constant in (4.3), its derivative can be written as

$$\dot{u}_e = -\dot{\hat{u}} \quad (4.14)$$

Substituting (4.14) into (4.13) yields to the rate of change of the input estimation error, i.e.,

$$\dot{u}_e = \frac{z}{1-z} k_c u_e \quad (4.15)$$

since $\frac{k\beta e^{-\gamma} y''}{2} < 0$ then the system is stable. As $u_e \rightarrow 0$, and $e^{-\gamma}$ converge to a small region so that $0 < e^{-\gamma} < 1$, then \hat{u} converge within a small region of u^* with minimised limit cycle.

Theorem 1 *For the simplified SDP-ESC scheme given in Fig. 4.2, the output error $y - y^*$ achieves local exponential convergence to an $O(\beta^2 e^{-2\gamma})$ of the origin with minimised limit cycle, provided the exponential decay is $0 < e^{-\gamma} < 1$.*

Proof of theorem 1

From (4.2) output error is expressed as

$$y - y^* \approx \frac{y''}{2}(u_e - \beta e^{-\gamma} \sin \omega t)^2 \quad (4.16)$$

Expanding (4.16) gives

$$y - y^* \approx \frac{y''}{2}u_e - y''u_e\beta e^{-\gamma} \sin \omega t + \beta^2 e^{-2\gamma} \frac{y''}{2} \sin^2 \omega t \quad (4.17)$$

as $u_e \rightarrow 0$ (4.17) reduced to

$$y - y^* \approx \beta^2 e^{-2\gamma} \frac{y''}{2} \sin^2 \omega t \quad (4.18)$$

Using definition (2) in Section 3.3.3, the right hand side term in (4.18) is bounded as follows

$$\beta^2 e^{-2\gamma} \frac{y''}{2} \sin^2 \omega t = O(\beta^2 e^{-2\gamma}) \quad (4.19)$$

hence,

$$y - y^* \approx O(\beta^2 e^{-2\gamma}) \quad (4.20)$$

4.4 Stability analysis

Stability analysis of the SDP-ESC is performed in the continuous time domain. Stability is analysed via the averaging technique which is a suitable method for analysing periodic systems (Ariyur & Krystic 2003). Stability analysis via the averaging technique includes the following steps:

1. transform a system with a new coordinate to obtain a simplified system,
2. use an averaging method to obtain the average of a reduced system and its equilibrium point,
3. compute the Jacobian of the average reduced system,
4. find the determinant of the average reduced system to check whether the system is stable or not.

System transformation:

Consider the non-linear system in Fig. 4.1 presented using state equations as,

$$\begin{bmatrix} \dot{u} = k_d \xi + \hat{x} \\ \dot{\hat{x}} = k \xi \\ \dot{\xi} = -\omega_l \xi - \eta \omega_l \sin \omega t + \omega_l y(u) \sin \omega t \\ \dot{\eta} = -\eta \omega_h + y(u) \omega_h \\ u = \hat{u} + \beta e^{-\gamma} \sin \omega t \end{bmatrix} \quad (4.21)$$

where:

- u is the control input,
- y is the optimal value as the function of control input,
- $k_d = k k_c$ is the product of compensator and integrator gains.

Let us define new coordinates in order to shift the nominal optimal operating point, denoted as:

$$\tilde{u} = \hat{u} - u^* \quad (4.22)$$

$$\tilde{\eta} = \eta - y(u^*) \quad (4.23)$$

Nonlinear system in (4.21) can be translated as follows

$$\begin{bmatrix} \dot{\tilde{u}} = k_d \xi + \hat{x} \\ \dot{\hat{x}} = k \xi \\ \dot{\xi} = -\omega_l \xi - \tilde{\eta} \omega_l \sin \omega t + \omega_l [y(\tilde{u} + u^* + \beta e^{-\gamma} \sin \omega t) - y(u^*)] \sin \omega t \\ \dot{\tilde{\eta}} = -\tilde{\eta} \omega_h - \omega_h [y(\tilde{u} + u^* + \beta e^{-\gamma} \sin \omega t) - y(u^*)] \end{bmatrix} \quad (4.24)$$

Set $\tau = \omega t$ and $V(\tilde{u}_r + \beta e^{-\gamma} \sin \omega t) = y(\tilde{u} + u^* + \beta e^{-\gamma} \sin \tau) - y(u^*)$ to obtain a **reduced system** in the following form

$$\frac{d}{d\tau} \begin{bmatrix} \tilde{u}_r \\ \hat{x}_r \\ \xi_r \\ \tilde{\eta}_r \end{bmatrix} = \frac{1}{\omega} \begin{bmatrix} k_d \xi_r + \hat{x} \\ k \xi_r \\ -\omega_l \xi_r - \omega_l \tilde{\eta}_r \sin \tau + \omega_l V(\tilde{u}_r + \beta e^{-\gamma} \sin \tau) \sin \tau \\ -\omega_h \tilde{\eta}_r - \omega_h V(\tilde{u}_r + \beta e^{-\gamma} \sin \tau) \end{bmatrix} \quad (4.25)$$

Adopting design parameters selection used in (Ariyur & Krystic 2003), normalized parameters are given as

$$k = \omega K = \omega \delta K' = O(\omega \delta) \quad (4.26a)$$

$$k_d = \omega K_d = \omega \delta K'_d = O(\omega \delta) \quad (4.26b)$$

$$\omega_l = \omega \omega_L = \omega \delta \omega'_L = O(\omega \delta) \quad (4.26c)$$

$$\omega_h = \omega \omega_H = \omega \delta \omega'_H = O(\omega \delta) \quad (4.26d)$$

where ω and δ are small positive constants and K'_d, ω'_L , and ω'_H are $O(1)$ positive constants.

$$\frac{d}{d\tau} \begin{bmatrix} \tilde{u}_r \\ \hat{x}_r \\ \xi_r \\ \tilde{\eta}_r \end{bmatrix} = \delta \begin{bmatrix} K'_d \xi_r + \hat{x} \\ K' \xi_r \\ -\omega'_L \xi_r - \omega'_L \tilde{\eta}_r \sin \tau + \omega'_L V(\tilde{u}_r + \beta e^{-\gamma} \sin \tau) \sin \tau \\ -\omega'_H \tilde{\eta}_r - \omega'_H V(\tilde{u}_r + \beta e^{-\gamma} \sin \tau) \end{bmatrix} \quad (4.27)$$

Averaging method

In order to analyse the reduced periodic system in (4.27) an averaging technique is used. The averaging equation is defined as,

$$x_a = \frac{1}{2\pi} \int_0^{2\pi} x(\sigma) d(\sigma) \quad (4.28)$$

where $(\sigma) = \tau$

Note that: the average of $\sin \tau = 0$, hence $\omega'_L \tilde{\eta}_r \sin \tau = 0$

Equation (4.27) can be expressed as

$$\frac{d}{d\tau} \begin{bmatrix} \tilde{u}_r^a \\ \hat{x}_r^a \\ \xi_r^a \\ \tilde{\eta}_r^a \end{bmatrix} = \delta \begin{bmatrix} K'_d \xi_r^a + \hat{x}_r^a \\ K' \xi_r^a \\ -\omega'_L \xi_r^a + \frac{\omega'_L}{2\pi} \int_0^{2\pi} V(\tilde{u}_r^a + \beta e^{-\gamma} \sin \tau) \sin \tau d\tau \\ -\omega'_H \tilde{\eta}_r^a - \frac{\omega'_H}{2\pi} \int_0^{2\pi} V(\tilde{u}_r^a + \beta e^{-\gamma} \sin \tau) d\tau \end{bmatrix} \quad (4.29)$$

The equilibrium of system $(\tilde{u}_r^{a,e}, \hat{x}_r^{a,e}, \xi_r^{a,e}, \tilde{\eta}_r^{a,e})$ presented in (4.29) must satisfy

$$0 = \begin{bmatrix} K'_d \xi_r^{a,e} + \hat{x}_r^{a,e} \\ K' \xi_r^{a,e} \\ -\omega'_L \xi_r^{a,e} + \frac{\omega'_L}{2\pi} \int_0^{2\pi} V(\tilde{u}_r^{a,e} + \beta e^{-\gamma} \sin \tau) \sin \tau d\tau \\ -\omega'_H \tilde{\eta}_r^{a,e} - \frac{\omega'_H}{2\pi} \int_0^{2\pi} V(\tilde{u}_r^{a,e} + \beta e^{-\gamma} \sin \tau) d\tau \end{bmatrix} \quad (4.30)$$

where

$$\xi_r^{a,e} = 0 \quad (4.31a)$$

$$\hat{x}_r^{a,e} = 0 \quad (4.31b)$$

$$\int_0^{2\pi} V(\tilde{u}_r^{a,e} + \beta e^{-\gamma} \sin \tau) \sin \tau d\tau = 0 \quad (4.31c)$$

$$\tilde{\eta}_r^{a,e} = \frac{1}{2\pi} \int_0^{2\pi} V(\tilde{u}_r^{a,e} + \beta e^{-\gamma} \sin \tau) d\tau \quad (4.31d)$$

In view of assumption (3), it is clear that:

$$V(0) = 0 \quad (4.32a)$$

$$V'(0) = y'(u^*) = 0 \quad (4.32b)$$

$$V''(0) = y''(u^*) < 0 \quad (4.32c)$$

Substituting $V(0)$, $V'(0)$ and $V''(0)$ into a Taylor expansion gives :

$$V(x) = V(0) + V'(0)x + \frac{V''(0)}{2!}x^2 + \dots \quad (4.33)$$

Postulating in a similar manner to (Ariyur & Krystic 2003), $\tilde{u}_r^{a,e}$ is expressed as,

$$\tilde{u}_r^{a,e} = a_1\beta + a_2\beta^2 + O(\beta^3) \quad (4.34)$$

Substituting (4.34) into (4.31c) and using (4.33), followed by integrating and equating same power of β yield to,

$$\int_0^{2\pi} V(\tilde{u}_r^{a,e} + \beta e^{-\gamma} \sin \tau) \sin \tau d\tau = \int_0^{2\pi} \frac{V''(0)}{2!} (\tilde{u}_r^{a,e} + \beta e^{-\gamma} \sin \tau)^2 \sin \tau d\tau + \int_0^{2\pi} \frac{V'''(0)}{3!} (\tilde{u}_r^{a,e} + \beta e^{-\gamma} \sin \tau)^3 \sin \tau d\tau = 0 \quad (4.35)$$

$$V''(0)\pi\beta e^{-\gamma}(\tilde{u}_r^{a,e}) + \frac{V'''(0)}{8}\pi\beta^3 e^{-3\gamma} + \frac{V'''(0)}{2}\pi\beta^3 e^{2\gamma}(\tilde{u}_r^{a,e})^2 = 0 \quad (4.36)$$

Simplifying by a bound higher power gives,

$$V''(0)\pi\beta^2 e^{-\gamma} a_1 + V''(0)\pi\beta^3 e^{-\gamma} a_2 + \frac{V'''(0)}{8}\pi\beta^3 e^{-3\gamma} = 0 \quad (4.37)$$

hence,

$$a_1 = 0 \quad (4.38a)$$

$$a_2 = -\frac{V'''(0)}{8V''(0)} e^{-2\gamma} \quad (4.38b)$$

Substituting (4.38) into (4.34) gives

$$\tilde{u}_r^{a,e} = -\frac{V'''(0)}{8V''(0)} e^{-2\gamma} \beta^2 + O(\beta^3) \quad (4.39)$$

Using (4.32) followed by integrating, (4.31d) yields to

$$\tilde{\eta}_r^{a,e} = \frac{1}{2\pi} \int_0^{2\pi} V(\tilde{u}_r^{a,e} + \beta e^{-\gamma} \sin \tau) d\tau = \frac{1}{2\pi} \left[\int_0^{2\pi} \frac{V''(0)}{2!} (\tilde{u}_r^{a,e} + \beta e^{-\gamma} \sin \tau)^2 d\tau \right] + \frac{1}{2\pi} \left[\int_0^{2\pi} \frac{V'''(0)}{3!} (\tilde{u}_r^{a,e} + \beta e^{-\gamma} \sin \tau)^3 d\tau \right] \quad (4.40)$$

$$\tilde{\eta}_r^{a,e} = \frac{1}{2\pi} \left[\frac{V''(0)}{2!} \pi (e^{-2\gamma} \beta^2 + 2(\tilde{u}_r^{a,e})^2) \right] + \frac{1}{2\pi} \left[\frac{V'''(0)}{3!} \pi \tilde{u}_r^{a,e} (3e^{-2\gamma} \beta^2 + 2(\tilde{u}_r^{a,e})^2) \right] \quad (4.41)$$

$$\tilde{\eta}_r^{a,e} = \frac{V'''(0)}{4} e^{-2\gamma} \beta^2 + \frac{V''(0)}{2} (\tilde{u}_r^{a,e})^2 + \frac{V''(0)}{4} e^{-2\gamma} \beta^2 (\tilde{u}_r^{a,e}) + \frac{V'''(0)}{6} (\tilde{u}_r^{a,e})^3 \quad (4.42)$$

Bound higher terms with big O yields to

$$\tilde{\eta}_r^{a,e} = \frac{V''(0)}{4} e^{-2\gamma} \beta^2 + O(\beta^3) \quad (4.43)$$

The equilibrium of the average model in (4.29) in compact form is expressed as

$$\begin{bmatrix} \tilde{u}_r^{a,e} \\ \hat{x}_r^{a,e} \\ \xi_r^{a,e} \\ \tilde{\eta}_r^{a,e} \end{bmatrix} = \begin{bmatrix} -\frac{V'''(0)}{8V''(0)} e^{-2\gamma} \beta^2 + O(\beta^3) \\ 0 \\ 0 \\ \frac{V''(0)}{4} e^{-2\gamma} \beta^2 + O(\beta^3) \end{bmatrix} \quad (4.44)$$

The Jacobian of an average system

The Jacobian of (4.29) can be presented as,

$$J_r^a = \begin{bmatrix} 0 & 1 & K'_d & 0 \\ 0 & 0 & K' & 0 \\ \frac{\omega'_L}{2\pi} \int_0^{2\pi} V'(\tilde{u}_r^a + \beta e^{-\gamma} \sin \tau) \sin \tau d\tau & 0 & -\omega'_L & 0 \\ \frac{-\omega'_H}{2\pi} \int_0^{2\pi} V'(\tilde{u}_r^a + \beta e^{-\gamma} \sin \tau) d\tau & 0 & 0 & -\omega'_H \end{bmatrix} \quad (4.45)$$

Approximate $V'(\tilde{u}_r^a + \beta e^{-\gamma} \sin \tau)$ from (4.45) using (4.33) and taking derivatives of $V(x)$ yields to

$$V'(\tilde{u}_r^a + \beta e^{-\gamma} \sin \tau) = V'(0) + V''(0)(\tilde{u}_r^a + \beta e^{-\gamma} \sin \tau) + \frac{V'''(0)}{2!}(\tilde{u}_r^a + \beta e^{-\gamma} \sin \tau)^2 \quad (4.46)$$

solving $\frac{\omega'_L}{2\pi} \int_0^{2\pi} V'(\tilde{u}_r^a + \beta e^{-\gamma} \sin \tau) \sin \tau d\tau$ from (4.45) yields to

$$\begin{aligned} \frac{\omega'_L}{2\pi} \int_0^{2\pi} V'(\tilde{u}_r^a + \beta e^{-\gamma} \sin \tau) \sin \tau d\tau &= \frac{\omega'_L}{2\pi} \int_0^{2\pi} V''(0)(\tilde{u}_r^a + \beta e^{-\gamma} \sin \tau) \sin \tau d\tau + \\ &\quad \frac{\omega'_L}{2\pi} \int_0^{2\pi} \frac{V'''(0)}{2}(\tilde{u}_r^a + \beta e^{-\gamma} \sin \tau) \sin \tau d\tau \end{aligned} \quad (4.47)$$

For simplicity let higher order terms in (4.47) be bounded as

$$\frac{\omega'_L}{2\pi} \int_0^{2\pi} \frac{V'''(0)}{2}(\tilde{u}_r^a + \beta e^{-\gamma} \sin \tau) \sin \tau d\tau = O(\beta^2) \quad (4.48)$$

Solving (4.47) yields to

$$\frac{\omega'_L}{2\pi} \int_0^{2\pi} V'(\tilde{u}_r^a + \beta e^{-\gamma} \sin \tau) \sin \tau d\tau = \frac{\omega'_L e^{-\gamma}}{2} V''(0) \beta + O(\beta^2) \quad (4.49)$$

Solving $\frac{-\omega'_H}{2\pi} \int_0^{2\pi} V'(\tilde{u}_r^a + \beta e^{-\gamma} \sin \tau) d\tau$ from (4.45) yields to

$$\begin{aligned} \frac{-\omega'_H}{2\pi} \int_0^{2\pi} V'(\tilde{u}_r^a + \beta e^{-\gamma} \sin \tau) d\tau &= \frac{-\omega'_H}{2\pi} \int_0^{2\pi} V''(0)(\tilde{u}_r^a + \beta e^{-\gamma} \sin \tau) d\tau + \\ &\quad \frac{-\omega'_H}{2\pi} \int_0^{2\pi} \frac{V'''(0)}{2}(\tilde{u}_r^a + \beta e^{-\gamma} \sin \tau) d\tau \end{aligned} \quad (4.50)$$

For simplicity let higher order terms in (4.50) be bounded as

$$\frac{-\omega'_H}{2\pi} \int_0^{2\pi} \frac{V'''(0)}{2}(\tilde{u}_r^a + \beta e^{-\gamma} \sin \tau) d\tau = O(\beta^2) \quad (4.51)$$

hence (4.50) become

$$\frac{-\omega'_H}{2\pi} \int_0^{2\pi} V'(\tilde{u}_r^a + \beta e^{-\gamma} \sin \tau) d\tau = -\omega'_H \tilde{u}_r^a V''(0) \beta + O(\beta^2) \quad (4.52)$$

The Jacobian of (4.45) is then expressed as

$$J_r^a = \begin{bmatrix} 0 & 1 & K'_d & 0 \\ 0 & 0 & K' & 0 \\ \frac{\omega'_L e^{-\gamma}}{2} V''(0) \beta + O(\beta^2) & 0 & -\omega'_L & 0 \\ -\omega'_H \tilde{u}_r^a V''(0) \beta + O(\beta^2) & 0 & 0 & -\omega'_H \end{bmatrix} \quad (4.53)$$

The stability can further be investigated by solving the determinant as

$$\det(\lambda I - J_r^a) = \left(\begin{bmatrix} \lambda & 0 & 0 & 0 \\ 0 & \lambda & 0 & 0 \\ 0 & 0 & \lambda & 0 \\ 0 & 0 & 0 & \lambda \end{bmatrix} - \delta \begin{bmatrix} 0 & 1 & K'_d & 0 \\ 0 & 0 & K' & 0 \\ \frac{\omega'_L e^{-\gamma}}{2} V''(0) \beta + O(\beta^2) & 0 & -\omega'_L & 0 \\ -\omega'_H \tilde{u}_r^a V''(0) \beta + O(\beta^2) & 0 & 0 & -\omega'_H \end{bmatrix} \right) \quad (4.54)$$

The determinant of (4.54) can further simplified and expressed as:

$$\det(\lambda I - J_r^a) = (\lambda + \delta \omega'_H) (\lambda^3 + p\lambda^2 + c\beta\lambda + b\beta) + O(\beta^2 \delta^2) \quad (4.55)$$

whereas:

- $c = -\frac{K'_d e^{-\gamma} \omega'_L \delta^2}{2} V''(0)$
- $b = -\frac{K' e^{-\gamma} \omega'_L \delta^3}{2} V''(0)$
- $p = \omega'_L \delta$

In view of $V''(0) = y(u^*) < 0$ parameters c and b are positive. Using the Routh-Hurwitz criterion, expression $(\lambda^3 + p\lambda^2 + c\beta\lambda + b\beta)$ can be solved as follows:

$$\begin{array}{lll} \lambda^3 & 1 & c\beta \\ \lambda^2 & p & b\beta \\ \lambda^1 & \frac{(cp-b)\beta}{p} & \\ \lambda^0 & b\beta & \end{array}$$

Hence it has proven that J_r^a is Hurwitz for $\frac{(cp-b)\beta}{p} \geq 0$

4.5 SDP-ESC design for single parameter scheme

The SDP-ESC comprises of seven main tuning parameters namely: integrator gain k , compensator gain k_c , exponential decay constant α , perturbation gain β , perturbation frequency ω , high pass filter and low pass filter cut off frequencies ω_h , ω_l , respectively. Each parameter independently or dependently, affects overall the performance of the SDP-ESC such as the tracking accuracy and steady-state performance. For instance, tracking accuracy and steady state error are influenced by β , k and α . In order to insure fine-tuning of the SDP-ESC, Section 4.5.1 provides guidance for designing an optimal SDP-ESC for the LTI and the LTV dynamical systems.

4.5.1 Algorithm design guideline

As aforementioned the SDP-ESC comprises of the PI controller (compensator) and the SDP function (see Fig. 4.1). With respect to the choice of parameters themselves, there are a number of consideration that must be made. This Section, therefore provides a suitable way of optimising these parameters to achieve optimal performance.

[1] ω should be selected slightly larger than the plant bandwidth

Firstly, the frequency ω of the perturbation signal must be sufficiently large but not equal to the frequency of any noise components else the tracking error will

increase. The bounded noise is assumed to be uncorrelated with the perturbation signal, therefore the frequency of noise can be bounded as per Eq. 4.56

$$f_n = \lim_{T \rightarrow \infty} \frac{1}{T} \int_0^T n \sin \omega t dt \quad (4.56)$$

where f_n is the noise frequency and T is the period of the perturbation signal.

- [2] *Perturbation gain β must be large enough to excite the plant as well as to achieve a desired convergence speed*

A large β will increase the speed of convergence with minimum oscillations due to the exponentially decaying effect cause by the SDP function. If β is too small it may fail to excite the plant, especially when the SDP-ESC algorithm is applied to low voltage applications. As the SDP function will decay exponentially close to zero, β can be selected to increase the rate of convergence to the extremum, as well as providing sufficient excitation to the plant.

- [3] *Cut-off frequencies for high pass and low pass filter should be selected such that $(\omega_h, \omega_l \ll \omega)$*

The upper corner frequency ω_h and the lower corner frequency ω_l should be chosen after determining the frequency ω of the perturbation signal such that $(\omega_h, \omega_l \ll \omega)$. The upper corner frequency ω_h and the lower corner frequency ω_l should be bounded such that the HPF removes any unwanted DC components. On the other hand, the LPF should attenuate the any unwanted high frequency components. The dynamics of these filters (i.e. HPF and LPF) should be sufficiently fast to respond to the perturbations.

- [4] *Set k_c and k sufficiently large to adapt to the changes in the plant without detecting small variations caused by noise*

MPP tracking by the SDP-ESC depends on k_c and k . These parameters should be selected such that, noise is not detected within the feedback loop. Large k and k_c may increase oscillations due to the continuous detection of every small variation within the feedback loop.

[5] *It is important to select the exponential decaying constant α such that $\text{var}(\hat{x}) < \alpha$*

If $\alpha = 0$, there will be no effect on limit cycle minimisation, and the resulting SDP-ESC will merely provide the same performance as the conventional PESC. Conversely, if $\alpha < 0$ is selected $f(\hat{x})$ will increase exponentially, causing the control system to become unstable. Since the state dependent function $f(\hat{x})$ causes the perturbation gain β to decay exponentially to a small value when $\alpha > 0$ is selected, it is therefore apparent that selecting a large value of β introduces the system neither unwanted oscillations nor sensitivity to noise. In order to successfully minimise limit cycle as well as ensure the system responds correctly, α should be bounded such that $\text{var}(\hat{x}) < \alpha$.

Remark 1 *In order to successfully design the SDP-ESC scheme, one should start by designing the PESC tuning parameters (i.e. β , ω , ω_h and ω_l , φ and k), followed by modified scheme (see Fig. 4.1) parameters (i.e. α and k_c).*

Remark 2 *Depending on the design requirement, the compensator in the modified scheme (see Fig. 4.1) can be designed as $\frac{C_z \cdot s + 1}{C_p \cdot s + 1}$ where: C_z and C_p are compensator zero and compensator pole, respectively. If one sets C_z and C_p equals 1 it implies no compensation effect on the SDP-ESC feedback loop. Other tuning parameters such as β and k can be used to improve the convergence speed.*

4.6 Simulation examples

This section presents simulation studies for a nonlinear plant given in Eq. 3.1. It should be noted that examples used here aim to demonstrate advantages of the SDP-ESC over the standard PESC on limit cycle minimisation, convergence speed and preserving the simplicity of the PESC. Also, these examples aim to verify all the assumptions made in this chapter and chapter 3. Comparison between SDP-ESC with other MPPT algorithms such as the LBS-ESC and the VBS-ESC is therefore presented separately in Chapter 6. The effectiveness of the SDP-ESC has been demonstrated for both systems with and without input/output dynamics. Prior to present simulation results, let us define the following terms.

Definition 4 *The power conditioning unit (PCU) or MPPT converter is the combination of DC-DC converter and MPPT algorithm.*

Definition 5 *The MPPT efficiency or percentage accuracy is the ratio between output power of the PCU and input power of the PCU.*

Definition 6 *PCU efficiency or percentage accuracy of the PCU is the ratio between output power and input power of the converter.*

Definition 7 *The tracking error accuracy refer the amplitude of oscillations between the desired value and the value achieved by MPPT algorithm*

4.6.1 SDP-ESC for LTI system

Consider a LTI system with a static nonlinear map given as

$$j(u) = j^* - (u - u^*)^2 \quad (4.57)$$

where $j^* = 0.8$ is the maximum value of function j and $u^* = 0.8$ is the point at which maximum value is achieved. For the given LTI system, it is considered

that,- there are no dynamics in the input or output. The function in (4.57) is differentiable therefore, it satisfies assumption 1. In addition, the steady-state characteristic of the function in (4.57) is well defined hence, satisfies assumption 2. The static nonlinear map in (4.57) has a unique maximum at $j^* = 0.8$ at steady-state hence, it verifies assumption 3. The system is simulated and performance of the SDP-ESC is compared with the standard PESC (see Fig. 4.3 and Fig. 4.4). Compared to the standard PESC, the SPD-ESC converges much faster to the extremum point as well as minimising limit cycles. Both the standard PESC and the SDP-ESC are optimised with the same tuning parameters for β , ω , ω_h , ω_l , φ and k (see Table. 4.1).

	Name	Notation	PESC	SDP-ESC
	Exponential decay constant	α	-	10^{-6}
	Perturbation gain	β	0.1	0.1
	High pass filter cut-off frequency	$\omega_h \left[\frac{rad}{s} \right]$	2.5	2.5
	Perturbation frequency	$\omega \left[\frac{rad}{s} \right]$	5	5
	Integrator gain	k	5	5
	Phase angle	$\varphi [rad]$	$\frac{\pi}{2}$	$\frac{\pi}{2}$
	Compensator zero	C_z	-	2
	Compensator pole	C_p	-	1

Table 4.1: PESC and SDP-ESC tuning parameters for LTI system

Based on algorithm design guidelines described in Section 4.5.1, ω is selected such that $\omega > \omega_h$. Based on the fact that the variance of \hat{x} reduces close to zero as the system enters stable limit cycles, in order to achieve $|f(\hat{x})| < |\beta|$, a small positive constant α is selected (see Table. 4.1). This ensures limit cycle minimisation once the system has entered stable limit cycle. A moving average variance with $N = 300$, where N is the number of sample, is used. The moving average variance is a windowed and is considered to be constant for a period of time. Hence it satisfies assumption 4. At steady-state the percentage error of the estimated input is reduced to 2% and 10% by the SDP-ESC and the PESC, respectively (see Fig. 4.5).

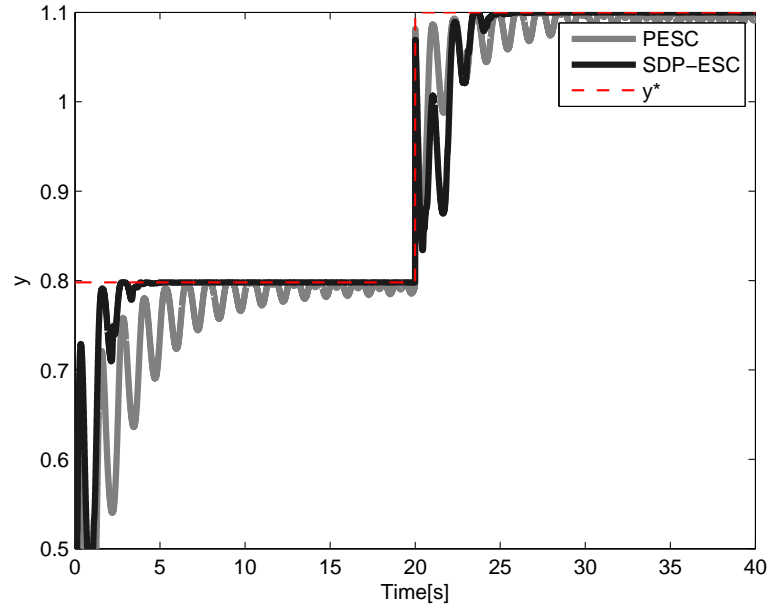


Figure 4.3: Illustrates output of the ESC and the SDP-ESC for LTI system

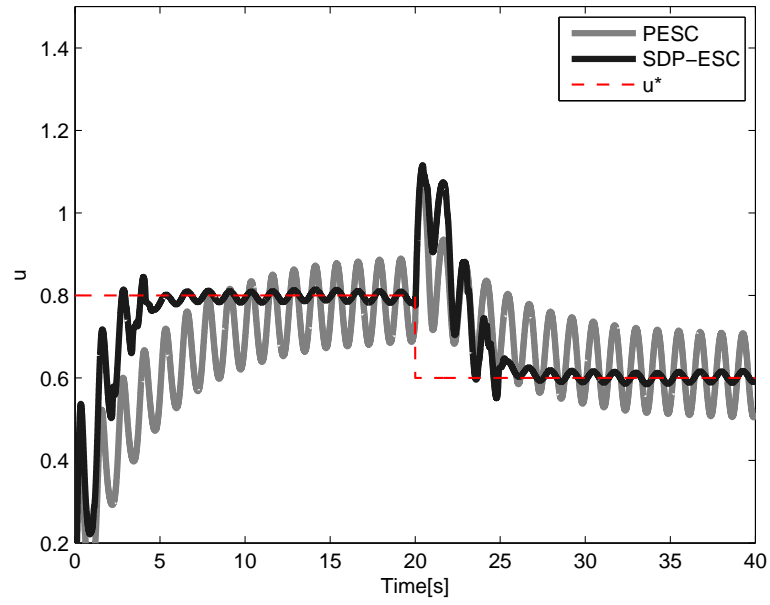


Figure 4.4: Illustrates estimates of the PESC and the SDP-ESC for LTI system

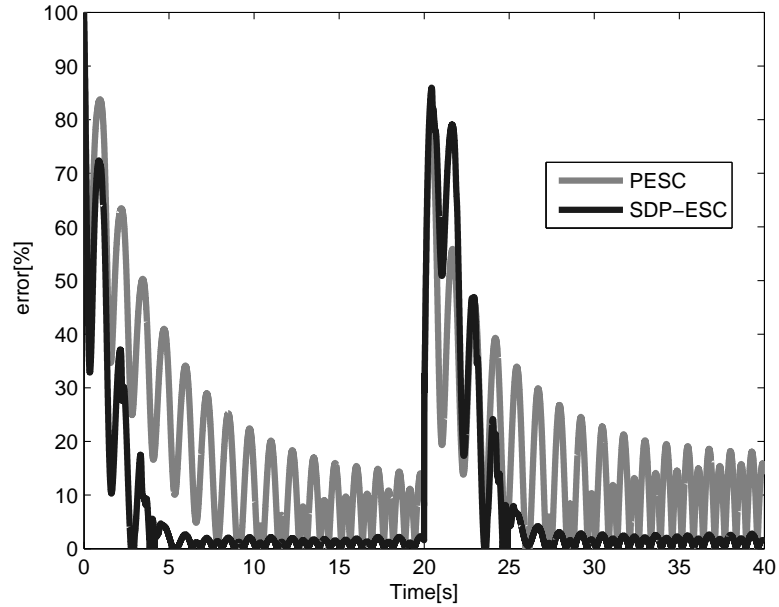


Figure 4.5: Illustrates steady-state percentage error of the estimated input obtained using the PESC and the SDP-ESC, respectively.

4.6.2 SDP-ESC for plant with dynamics

Effectiveness of the proposed SDP-ESC scheme over the standard PESC for plants with dynamics is demonstrated using the system presented in (Ariyur & Krystic 2003). The system behaviour is presented with set of equations as follows,

$$D_i(s) = \frac{s-1}{s^2+3s+2} \quad (4.58a)$$

$$D_o(s) = \frac{1}{s+1} \quad (4.58b)$$

$$j(u) = j^*(t) + (u - u^*(t))^2 \quad (4.58c)$$

$$j^*(t) = 0.01(t-10) \quad (4.58d)$$

$$u^*(t) = 0.01e^{0.01t} \quad (4.58e)$$

$$\lambda_u \Upsilon_u(s) = \frac{0.01}{s-1} \quad (4.58f)$$

$$\lambda_p \Upsilon_p(s) = \frac{0.01e^{-10s}}{s} \quad (4.58g)$$

where

- $D_i(s)$ and $D_o(s)$ denote input and output dynamics, respectively.
- $j^*(t)$ and $u^*(t)$ denote minimum value and point at minimum, respectively.

The PESC is optimised with the same tuning parameters as in (Ariyur & Krystic 2003) as summarised in Table. 4.2. The SDP-ESC is optimised with same tuning

	Name	Notation	PESC	SDP-ESC
Exponential decay constant		α	-	10^{-5}
Perturbation gain		β	0.05	0.05
High pass filter cutoff frequency		$\omega_h \left[\frac{rad}{s} \right]$	5	5
Perturbation frequency		$\omega \left[\frac{rad}{s} \right]$	5	5
Phase angle		$\varphi [rad]$	0.7955	0.7955
Integrator gain		k	107.7	107.7
Compensator pole		C_p		4
Compensator zero		C_z		0.01

Table 4.2: PESC and SDP-ESC tuning parameters for plant with dynamics

parameter values as the PESC with addition parameter α (see Table 4.2), hence validates the simplicity of the proposed scheme. A slide moving average variance with $N = 300$ is used. The minimum output value of the SDP function is limited at 10^{-6} to limit the function to decay to zero. As shown in Fig. 4.6 compared to the PESC, the SDP-ESC converges faster to the optimum value of control input with minimised limit cycle. Fig. 4.7) illustrates output measurement obtained using the PESC and the SDP-ESC. Compared to the PESC, the SDP-ESC converge much faster to the optimum value with smaller overshoot.

4.7 Sensitivity analysis

Robustness and performance of a non constraints based controller is highly dependent on tuning parameters. Also, assumptions of a noise free system is rather unrealistic particularly in practice, as measurement and system noise are always present and can affect the overall performance of a controller. On this basis, this section presents effects of the SDP-ESC tuning parameters, i.e., β , α , k_c , k and

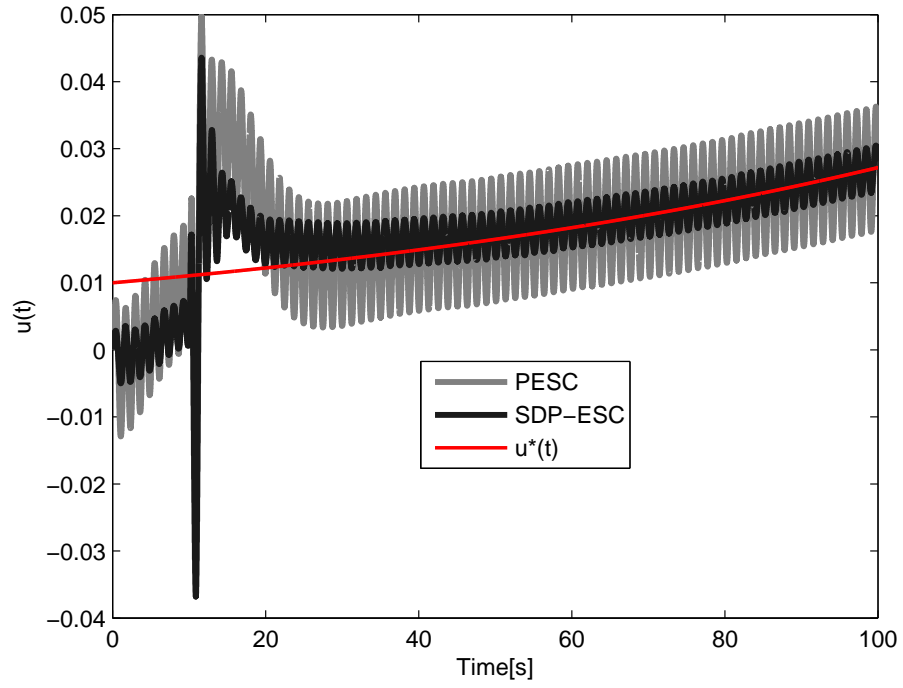


Figure 4.6: u parameter for ESC and SDP-ESC

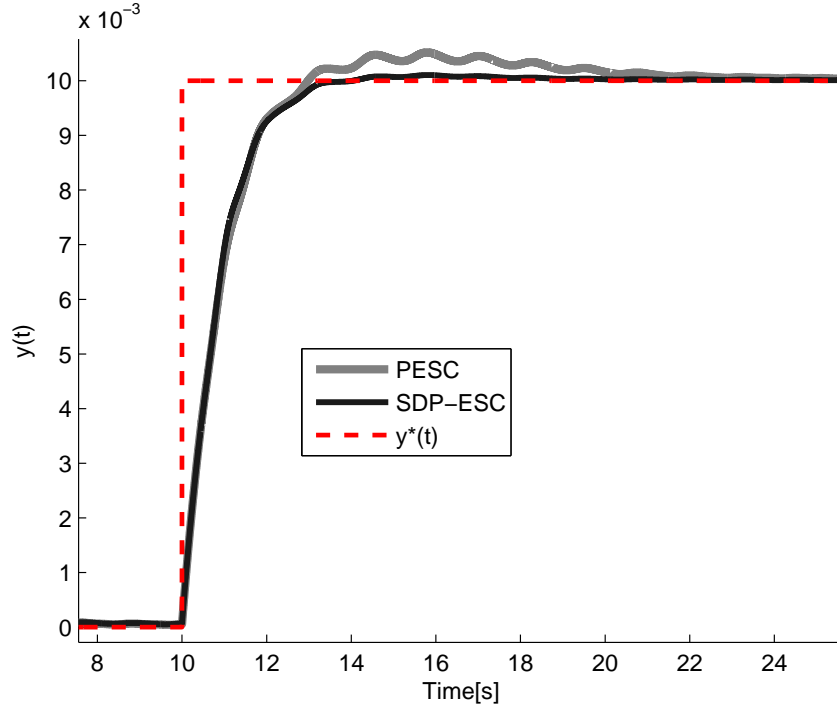


Figure 4.7: Output measurement for PESC and SDP-ESC

noise on convergence speed and limit cycles. The analysis is performed using the system in (4.57).

4.7.1 SDP-ESC tuning parameters

[1] Exponential decay constant and perturbation gain:

α has an effect on both convergence speed and limit cycle minimisation of u and y (see Fig. 4.8 and Fig. 4.9). This is observed by varying α from $5 \cdot 10^{-7}$ to 10^{-6} with the increment of $2.5 \cdot 10^{-7}$, selecting initial $\beta = 0.1$ and setting a minimum variance of $x = 5 \cdot 10^{-7}$. When 10^{-6} is selected, the lowest oscillations occur. However, it takes much longer to reach the steady-state. On the other hand, when $\alpha = 5 \cdot 10^{-7}$ is selected it converges much faster with more oscillations. Perturbation signal (i.e. $f(\hat{x})\sin\omega t$) amplitude depends on α . The lowest amplitude is achieved when $\alpha = 1e^{-6}$ (see Fig. 4.10).

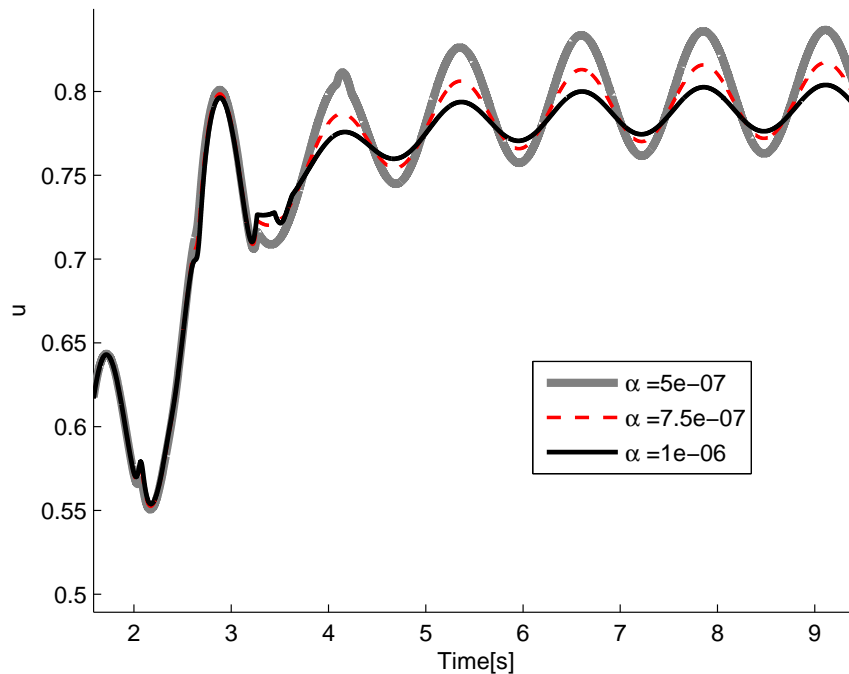


Figure 4.8: Illustrates estimates of the SDP-ESC for different α

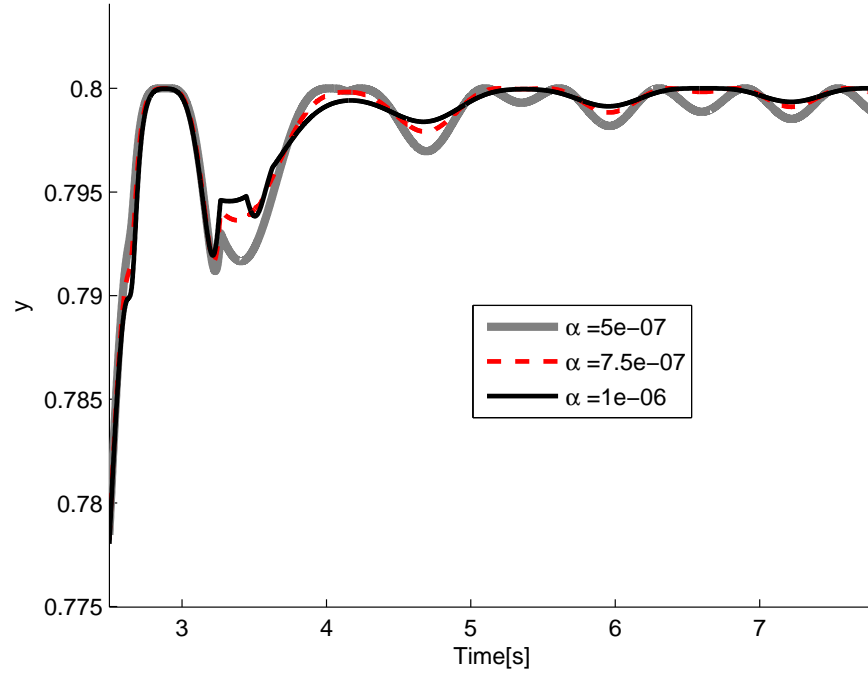


Figure 4.9: Illustrates output of the SDP-ESC for different α

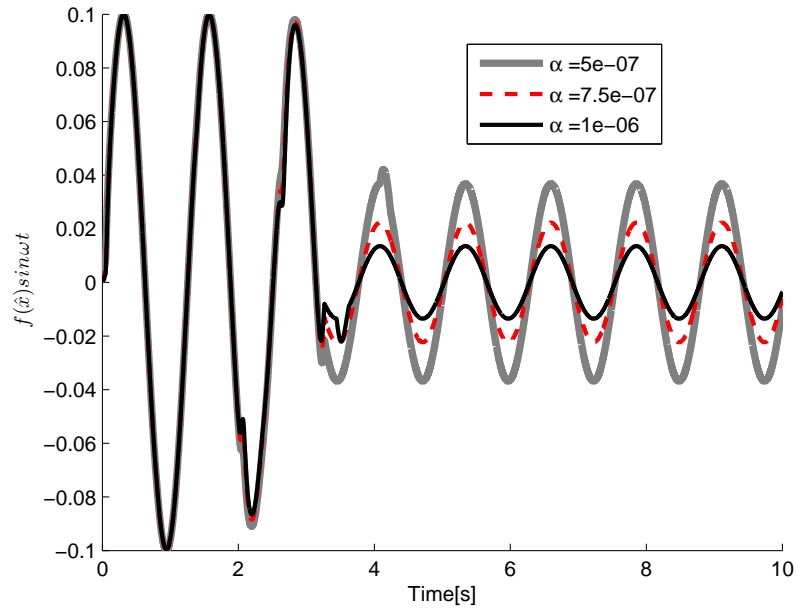


Figure 4.10: Illustrates perturbation gain amplitude of the SDP-ESC for different α

The initial value of β affects the convergence speed and the limit cycle minimisation in a similar manner to α . To guarantee a faster convergence speed as well as enough excitation, the SDP-ESC should be initialised with a sufficiently large value of β .

[2] Integrator and compensator gains:

Large values of k_c and k improves converge speed. k_c is set equal to 2.5 and k is varied from 2.5 to 3.5 with an increment of 0.5 (see Fig. 4.11, Fig. 4.12, and Fig. 4.13). For the SPD-ESC, k_c and k affect only the convergence speed. However these parameters should be carefully selected to avoid failure to converge to true value at steady-state as well as to detect noise in the feedback loop.

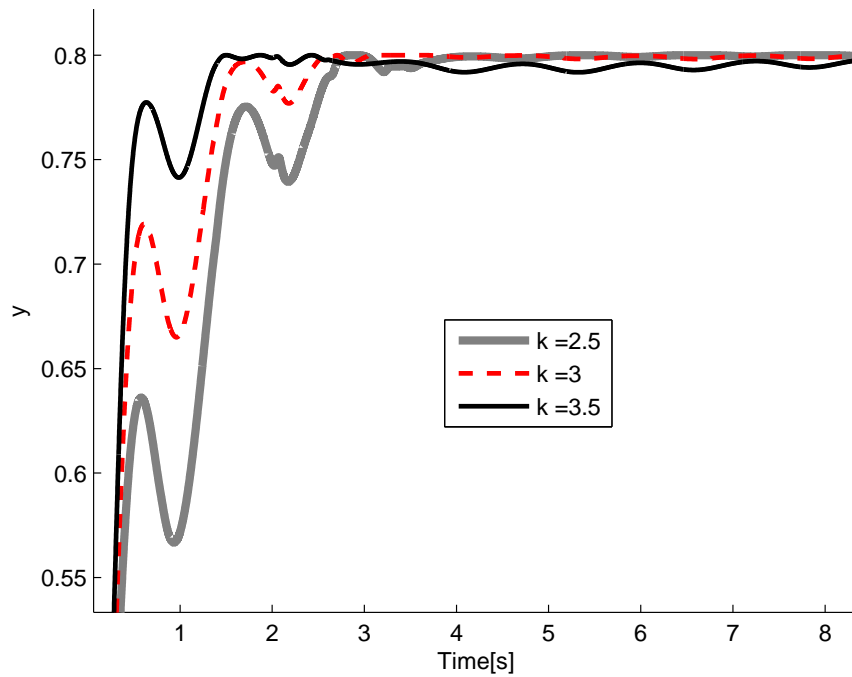


Figure 4.11: Illustrates output of the SDP-ESC for different k

4.7.2 Measurement noise

It is rather difficult to eliminate measurement noise in practice, therefore it is crucial to eliminate its influence. For this example, normally distributed white

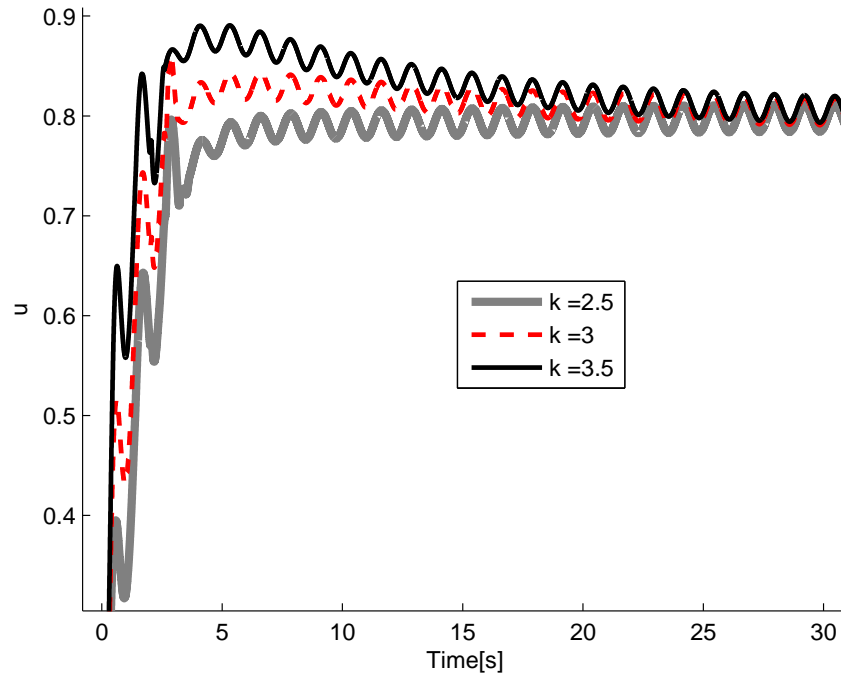


Figure 4.12: Illustrates estimates of the SDP-ESC for different k

noise is considered. Fig. 4.14 illustrates the simulation results of the PESC and the SDP-ESC, corresponding to different noise variances denoted σ^2 . It appeared that as compared to the PESC, the SDP-ESC is affected more by noise. When the variance of noise is low as $\sigma^2 = 1 \cdot 10^{-7}$ the SDP-ESC achieves better performance on both limit cycle minimisation and convergence speed. However, when the variance of noise is as high as $\sigma^2 = 1 \cdot 10^{-6}$ the SDP-ESC performance on tracking extremum point deteriorates. Both controllers are affected when the variance of noise is increased beyond $\sigma^2 = 1 \cdot 10^{-4}$.

Remark 3 *Tracking parameter/control input u is affected more in the SDP-ESC, compared to the PESC due to higher noise sensitivity of tuning parameter α , as a consequence one should carefully select this parameter.*

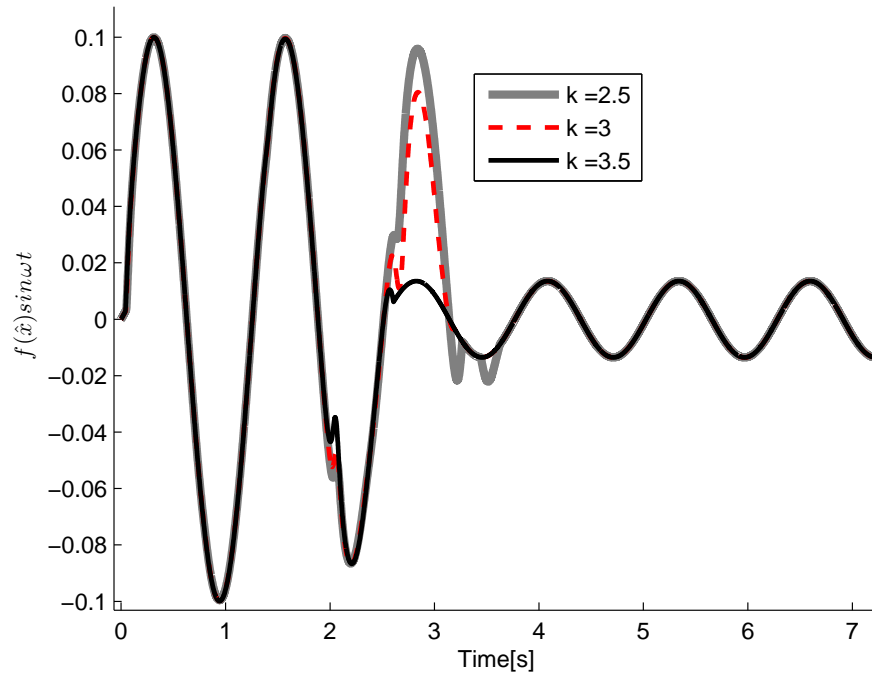


Figure 4.13: Illustrates perturbation gain amplitude of the SDP-ESC for different k

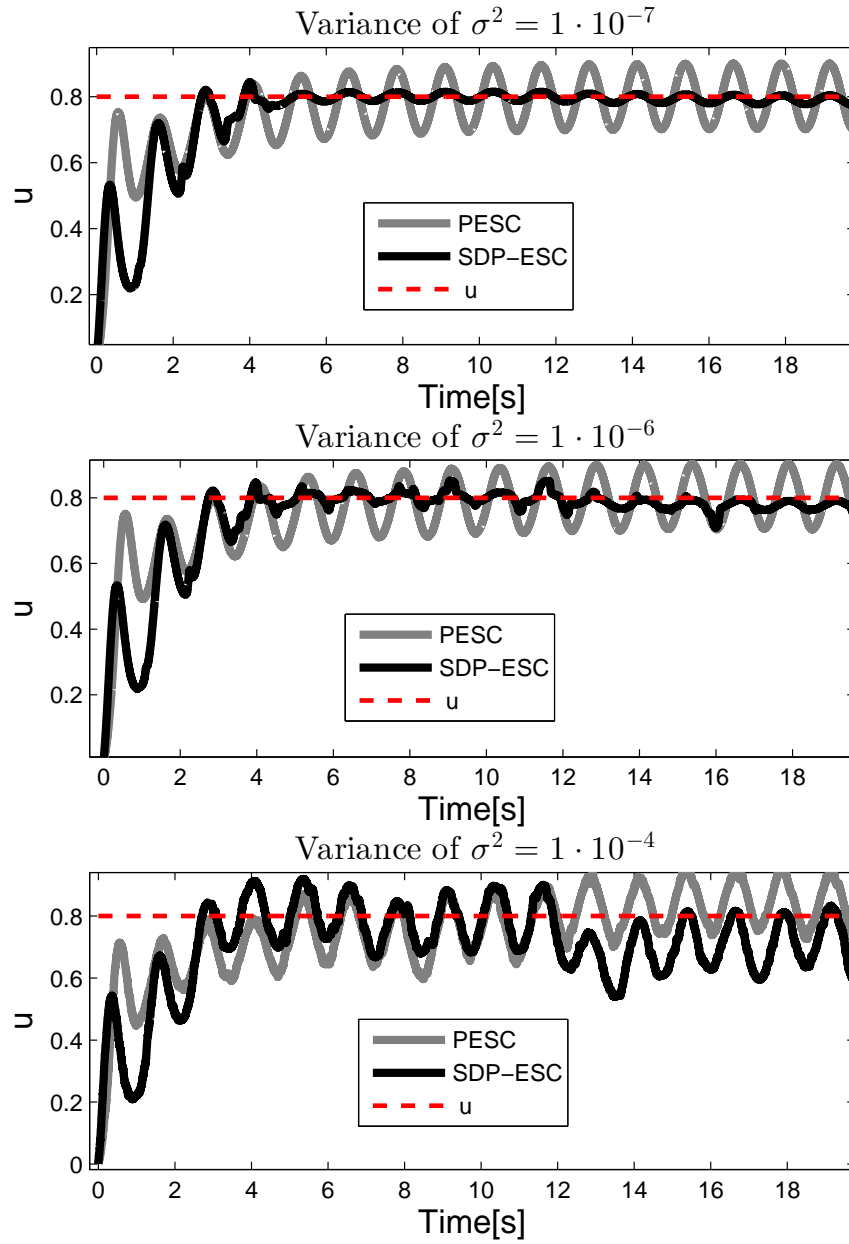


Figure 4.14: Noise level effects on estimates for PESC and SDP-ESC

4.8 Critical appraisal and conclusions

In this chapter a novel scheme for MPPT known as SDP-ESC is proposed. Numerical analysis on the ability of the proposed scheme to converge to the MPP whilst minimising losses has been investigated for a single parameter SDP-ESC scheme. Also, stability analysis of the proposed scheme is investigated using the averaging technique. Moreover, SDP-ESC design guideline and sensitivity analysis are presented. Superiority of the SDP-ESC over the standard PESC on limit cycle minimisation and convergence speed has been demonstrated using simulation examples, i.e., for plants with and without dynamics. It also preserves the stability and simplicity of the standard PESC. Comparison between the SDP-ESC and other algorithms, i.e., the VBS-ESC and the LBS-ESC on the trade-off between the convergence speed and minimisation of losses is presented in Chapter 6. Similar to other schemes such as PESC, LBS-ESC, VBS-ESC, the drawback of the SDP-ESC is its inability to search for the global maximum in the presence of local maxima. To eliminate this issue, an extension of the SDP-ESC is required. Chapter 5 presents a detailed explanation of the extended SDP-ESC.

Chapter 5

Extended SDP extremum seeking control

5.1 Introduction

There are several research developments on the global maximum (GM) search in the presence of local maxima. Most of these advancements have been seen in PV systems. However, as aforementioned in Chapter 1, the GM search is still an open problem. Methods for the GM search reviewed in Chapter 2 are based on stochastic approaches which require pre-training of the system. Therefore, these approaches are considered to be expensive (Tan, Nesic, Mareels & Astolfi 2009). Since this Thesis aim to provide an inexpensive solution for the GM search, the GM is based on an extension of the SDP-ESC proposed in Chapter 4. There are few pieces of literature which the propose extension of the ESC for the GM. ESC which searches for the GM was first proposed by Tan et al. (2009). The proposed scheme is able to converge to the GM if a large set of initial conditions are satisfied. One such condition is to initialise the ESC with a large perturbation gain which will force convergence to the GM (Tan et al. 2009). However, the method proposed by Tan et al. (2009) is shown to be ineffective when Azar, Per-

rier & Srinivasan (2011) use a function with large number of local maxima. For instance, when a 6th order polynomial was considered, the ESC scheme by Tan et al. (2009) failed to locate the GM. Azar, Perrier & Srinivasan (2011) proposed a multi-unit ESC for the GM search. Different static nonlinear functions with multiple maxima were used to verify the ability of the scheme proposed by Azar, Perrier & Srinivasan (2011) to search the GM. The proposed scheme comprises two identical units within a plant or process which operates at different set points and the difference between these set points is referred to as an offset. The finite difference for a given offset is applied to estimate the gradient. It also utilises an integrator within the multi-framework scheme to force the gradient to zero. It has been claimed in Azar, Perrier & Srinivasan (2011), that by starting with a large offset, reducing monotonically to zero and also using switching control strategy, it is possible to search for the GM.

Particle swarms have been combined with ESC to search for the GM (Yu, Chen & Kong 2010). The particle swarm algorithm generates a sequence based on an online cost function which is used to guide the ESC to search for the GM. However, this method has the disadvantage of taking a longer time to compute every loop of the ESC. Khong, Nesic, Manzie & Tan (2013) adopted a DIRECT search algorithm within ESC for a multi-dimensional GM search. DIRECT search is a method for solving optimisation problems that does not require any information about the gradient of the objective function. Apart from that, Doostabad, Keypour & Khalghani (2013) present a modified ESC with a GM search under uniform and non-uniform irradiance conditions. Compared to the standard ESC, the proposed ESC uses a single perturbation signal, hence ripples of lower frequency is achieved. It also uses series configuration of a LPF and a HPF which acts as BPF and allows a certain range of frequency (e.g. the derivative of power and voltage of the PV) to pass through as the results converge directly to the GM. This is also achieved by the inclusion of the partial shading effect detect-

ing algorithm. Under uniform shading the proposed method uses a variable step to allocate the MPP. On the other hand, under partial shading, the proposed method eliminates local MPP and forces the ESC to converge to the GM.

5.2 Problem statement

Searching for the MPP using the standard ESC, the LBS ESC and the SDP-ESC is based on controlling the gradient at zero through an integrator, which make these controllers suitable for systems with only local maxima (e.g TEG, PV system, FC system, wind turbine, etc.). On the other hand, when applied to systems whereby the input-output map experiences multiple maxima, these controllers may become ineffective and as a consequence, fail to converge to the GM. The PV system is one of the example which experiences this phenomenon. When a PV system is shaded this causes multiple maxima to occur. As a consequence, it is crucial to search for the global maximum to make the PV system operate under optimal performance (Doostabad, Keypour & Khalghani 2013). To make the SDP-ESC scheme presented in Chapter 4 suitable for such systems, further extension is required, an extended SDP-ESC scheme that searches for the global maximum in the presence of local maxima is presented. Performance of the proposed scheme is analysed via several static nonlinear functions with multiple maxima. In order to develop a simplified scheme for the GM search based on an extension of the SDP-ESC proposed in Chapter 4, the SDP-ESC scheme is kept intact and a GM scanning scheme is added. Fig. 5.1 illustrates a block diagram of the extended SDP-ESC scheme. The scheme comprises the GM scanning scheme and the SDP-ESC. The GM scanning scheme does not interfere with the closed loop dynamics therefore it is considered that the stability of the closed loop system is not affected by the GM scanning scheme. Since the proposed scheme for the GM is considered to be stable, stability analysis of the extended SDP-ESC is not

presented in this Thesis. The reference signal governs the GM scanning process. The scan process will always restart when a change in the reference is detected. Detailed description of the proposed GM scanning mechanism is presented in Section 5.2.1

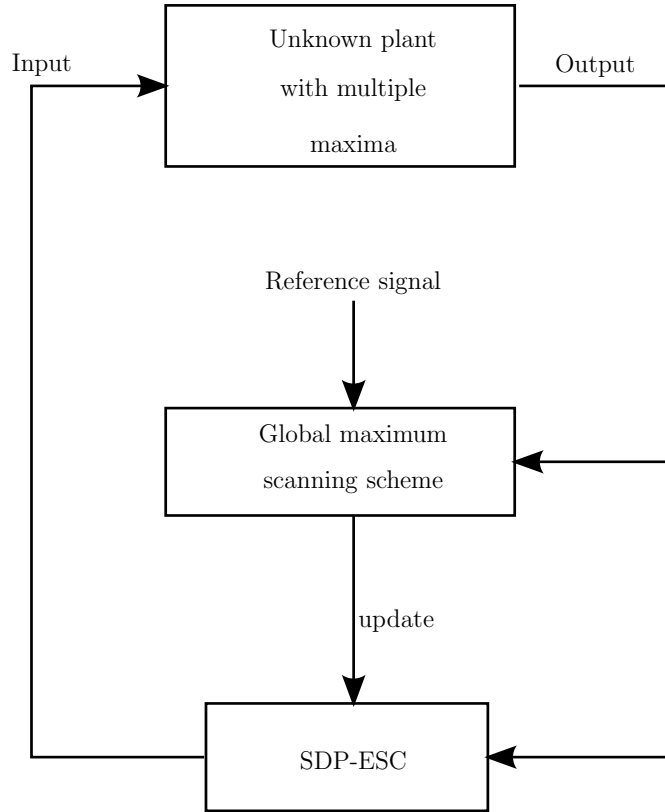


Figure 5.1: Block diagram of the extended SDP-ESC scheme for global maximum search

5.2.1 GM scanning scheme

The GM scanning scheme comprises three subsystems namely: searching window, window control and memory (see Fig. 5.2). Below is the description of each subsystem within a GM scanning scheme:

Searching window:

The function of the searching window within the GM scanning scheme is to initialise the control input of the SDP-ESC denoted \hat{u} at different points. Ini-

tialisation is based on *prior* knowledge of the system's operational range. For instance, a PCU operational range usually has a duty cycle which varies between 0% to 100% and hence the searching window can be initialised between 0 to 1. The searching window can be initialised using a look-up table of data points. However, the GM is efficiently searched when the searching window is treated as a ramp signal. This will allow the scanning of all available maxima. The length of the searching window is determined by the system operational range. For instance, if the system operational range is between 0 to 10 the searching window length will be 10. The minimum value of the searching window denoted W_{min} will be 0 and the maximum value of the searching window denoted W_{max} will be 10. Input to the searching window subsystem is window control denoted W_c and output is the initial point of the control input denoted u_{in} .

Memory block:

The memory blocks stores the measured output denoted y and its corresponding initialisation point at each time step. The amount of stored data depends on the size of the searching window denoted W . Mathematically W is calculated as

$$W = \frac{T_p}{T_s} \quad (5.1)$$

where T_p and T_s denote window period and sampling time, respectively. For instance, if $T_p = 2$ and $T_s = 0.1$ therefore based on (5.1) W will be equal to 20. This implies that 20 data points will be stored in the memory block.

Window control:

It governs the GM searching process by controlling the searching window. Every time the reference signal (denoted as REF in Fig 5.2) such as the irradiance of the PV system etc. changes, the scanning process will resume.

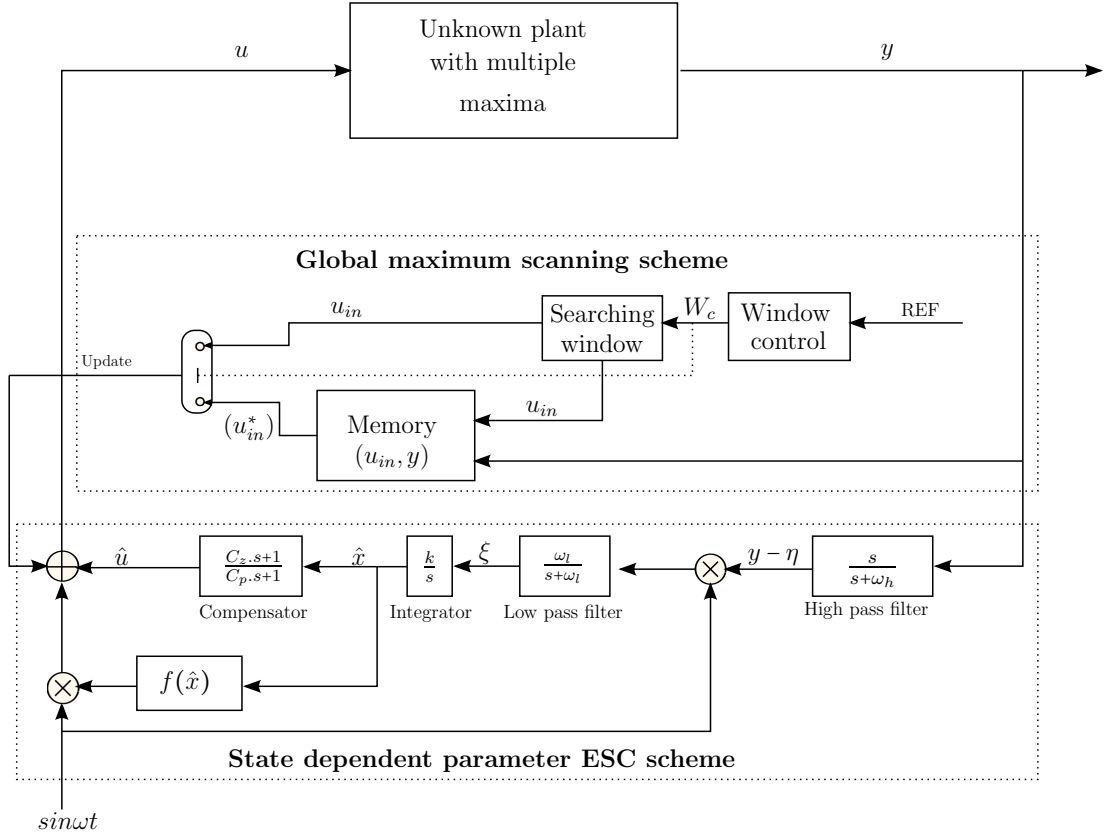


Figure 5.2: Extended SDP-ESC scheme for global maximum search in the presence of local maxima

GM searching process

First, the searching window is initialised with W_{min} . Also, the reference signal is initialised as 0. The initialisation point of the searching window and output measurements of the unknown plant are stored in the memory. If change on reference signal occurs, then the searching window will be reset to W_{min} . On the other hand, if no change is detected in the reference signal the next step will be to check whether the searching window has reached W_{max} . When the searching window equals to W_{max} , the memory block will return the point which corresponds to the GM. This is done by determining the highest value of the output within the searching window period. The index of the searching window corresponding to the highest output value is noted and the SDP-ESC will be updated with u_{in}^* , i.e., the index corresponding to the GM (highest output value).

On the other hand, if the searching window has not reached to W_{max} , then the searching window will be incremented by a chosen step size denoted C . Once the extended SDP-ESC converges to the GM, the searching (scanning) process will stop until change in reference signal is detected causing the scanning process to resume. Convergence speed to the GM is highly dependent on C . If the searching window is incremented by a smaller C this will result in a slow convergence speed to the GM. However, it will usually guarantee convergence to the actual GM.

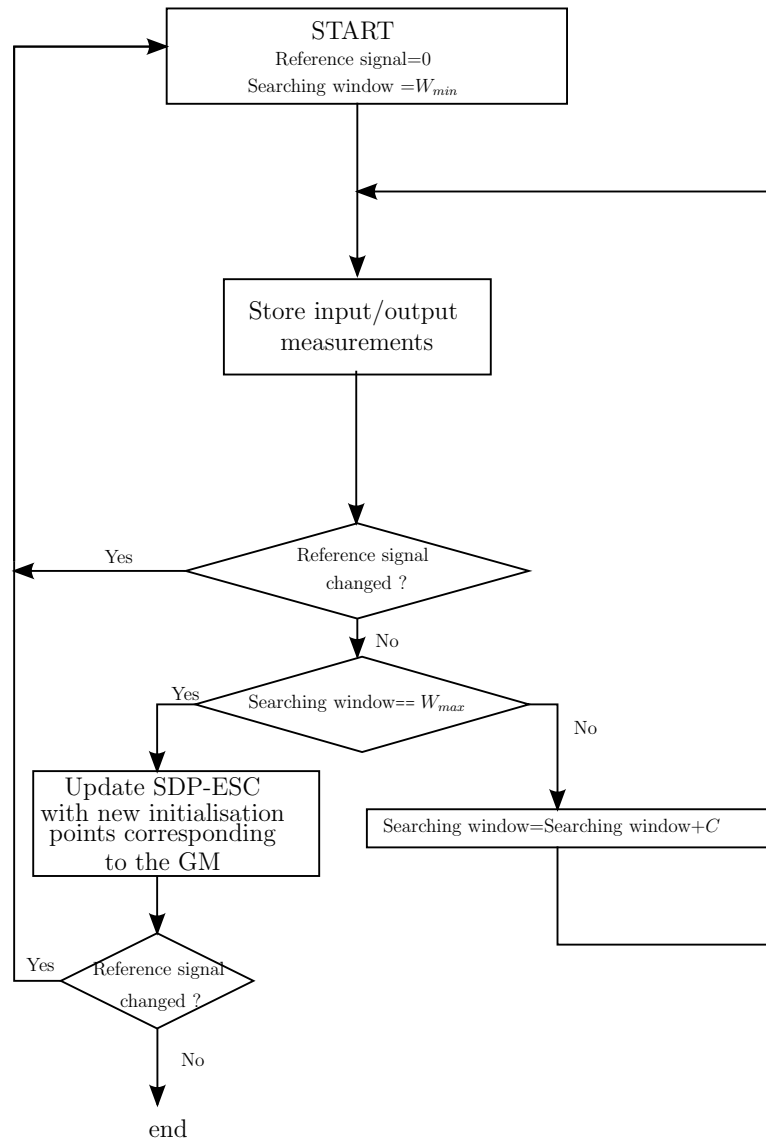


Figure 5.3: Flow chart for global maximum searching using extended SDP-ESC scheme

5.3 Simulation study

This section presents simulation examples of several functions with multiple maxima to demonstrate the ability of the extended SDP-ESC to search the GM in the presence of local maxima. Examples in Sections 5.3.1, 5.3.2 and 5.3.3 are also considered by Tan et al. (2009) and Azar, Perrier & Srinivasan (2011). These examples are based on assumptions that there is no input/output dynamics to the system. A simulation study for a plant with input/output dynamics is presented in Section 5.3.4.

5.3.1 Static nonlinear map: Example 1

Consider a static nonlinear map presented as sum of exponentials as

$$j(u) = e^{\frac{1}{(1+0.2u^2)}} + e^{\frac{1}{(1+5(u-15)^2)}} \quad (5.2)$$

$j(u)$ has two local maxima at $u = 0$ and $u = 15$. The GM is located at $u = 15$. Fig. 5.6 illustrates the input-output map of the system given in (5.2) (i.e., the map searched using the PESC, the SDP-ESC and the extended SDP-ESC). As shown in Fig. 5.4, both the PESC and the SDP-ESC converge to local maximum at $u = 0$. According to Azar, Perrier & Srinivasan (2011), global PESC scheme proposed by Tan et al. (2009) was unable to converge to the accurate GM. On the other hand, the extended SDP-ESC converges to the GM due to its pre-scanning mechanism, which allows to the scanning to all available maxima within a W . Once the extended SDP-ESC has converged to the GM, it thereafter decays exponentially to minimise limit cycles (see Fig 5.5). W of the extended SDP-ESC is incremented as a ramp input and initialised between -1 and 20 . Since both maxima are located between -1 and 15 , the searching period of $20s$ (see Fig. 5.4) is considered enough to the reach maximum value of the W . Given

that $T_s = 0.01s$ and $T_p = 20s$ therefore, maximum size of the W is calculated using (5.1) as: $W = \frac{T_p}{T_s} = \frac{20}{0.01} = 2000$ samples. Table 5.1 illustrates the tuning parameters of the PESC, the SDP-ESC, and the extended SDP-ESC.

Parameter	PESC	SDP-ESC	Extended SDP-ESC
α	-	10^{-6}	$5 \cdot 10^{-6}$
β	0.1	0.1	0.1
$\omega_h \left[\frac{rad}{s} \right]$	2.5	2.5	2.5
$\omega \left[\frac{rad}{s} \right]$	5	5	5
$\varphi [rad]$	$\frac{\pi}{2}$	$\frac{\pi}{2}$	$\frac{\pi}{2}$
$W \left[\frac{T_p}{T_s} \right]$	-	-	2000
k	1	1	1
C_p	-	2	2
C_z	-	1	1

Table 5.1: PESC and SDP-ESC and extended SDP-ESC tuning parameters for the global maximum search of example in Section 5.3.1

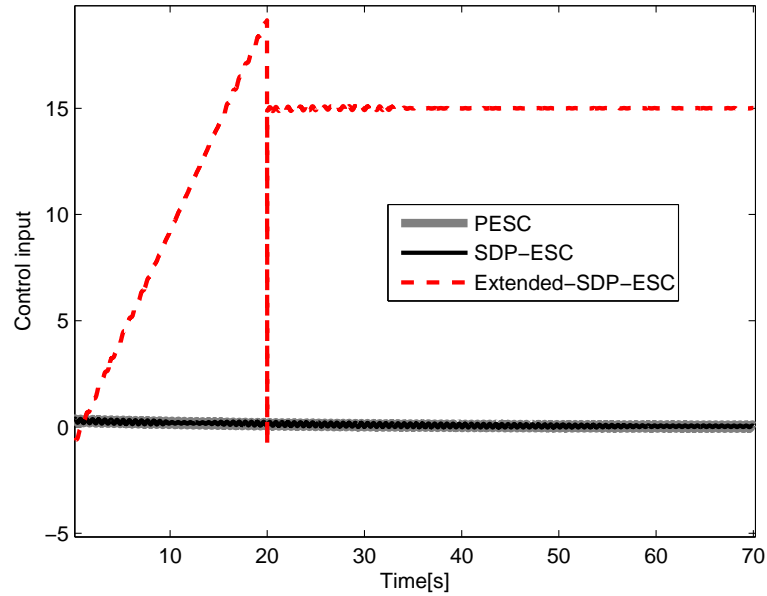


Figure 5.4: Control input for PESC, SDP-ESC and extended SDP-ESC for global maximum search of example in Section 5.3.1

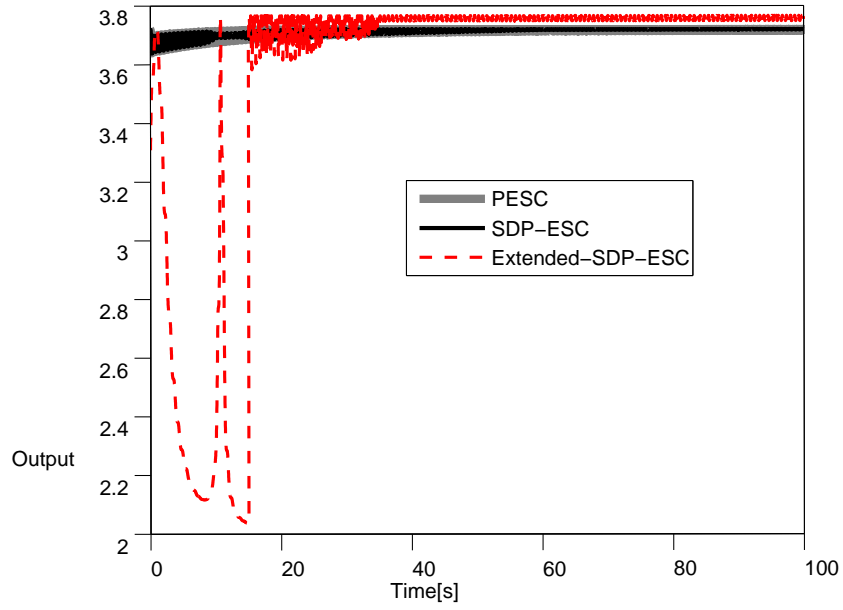


Figure 5.5: Output of example in Section 5.3.1

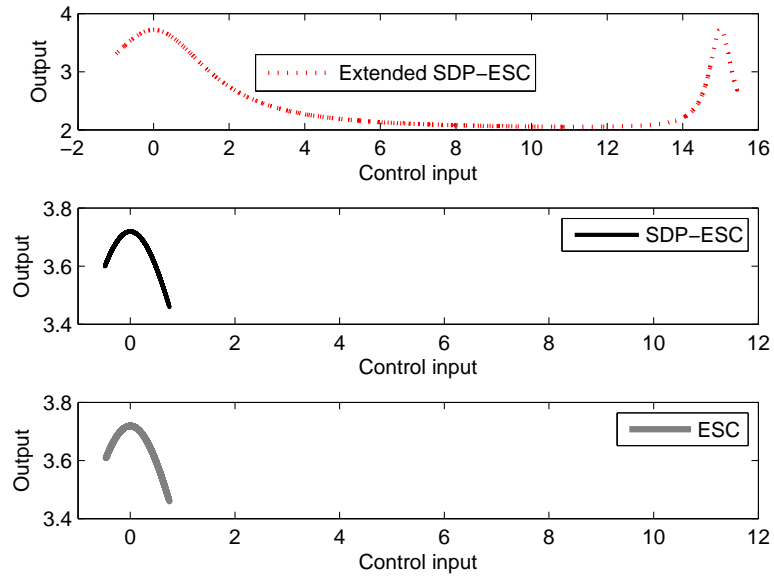


Figure 5.6: Input-output map of example in Section 5.3.1

5.3.2 Static nonlinear map: Example 2

Consider a static nonlinear map of the 6th order polynomial given as

$$j(u) = -u^6 + \frac{1}{10}u^5 + \frac{623}{400}u^4 - \frac{659}{4000}u^3 - \frac{11287}{20000}u^2 + \frac{259}{4000}u + \frac{637}{20000} \quad (5.3)$$

The polynomial given in (5.3) has three maxima at $u = -0.8985$, $u = 0.0$ and $u = 0.8951$. The global maximum is located at $u = -0.8985$. The maxima of (5.3) are located between -1 and 2 . As in example 5.3.1, in 5.3.2 the W is incremented as a ramp input. $T_s = 0.01$ is selected, therefore based on (5.1), $W = 200$ samples. As shown in Fig. 5.7, both the PESC and the SDP-ESC converge to the nearest local maximum at $u = 0$. On the other hand, the extended SDP-ESC converges to the GM at $u = -0.8985$ within 1s. Compared to the PESC and the SDP-ESC, the extended SDP-ESC is able to scan all available maxima (see Fig. 5.9) and accurately converge to the GM (see Fig. 5.8). The tuning parameters (i.e. $\beta, \omega_h, \omega, \varphi, C_p, C_z$) of the PESC, the SDP-ESC, and the extended SDP-ESC for system in (5.3) are the same as the system in (5.2). However, $k = 5$ for controllers, $\alpha = 2.5 \cdot 10^{-6}$ for the SDP-ESC and $\alpha = 3.5 \cdot 10^{-6}$ for the extended SDP-ESC.

5.3.3 Static nonlinear map: Example 3

Consider a static nonlinear map presented as

$$j(u) = -3u^4 + 64\sin^2 u^3 + 12u^2 + 4u - 80 \quad (5.4)$$

The static nonlinear map in (5.4) has several maxima and a unique GM at $u = 1.68$. The maxima of the system in (5.4) are located between -2 to 1 . Similar to the previous examples, $T_s = 0.01$ is selected. Using T_s and T_p therefore $W = 100$ samples. As shown in Fig. 5.10, both the PESC and the SDP-ESC converge to the local maximum at $u = -1.15$. On the other hand, the extended SDP-ESC scheme

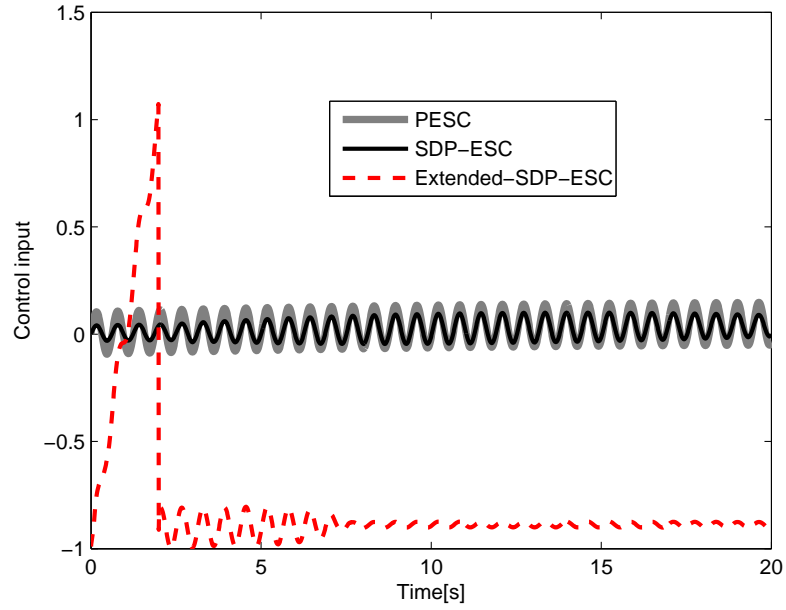


Figure 5.7: Control input for PESC, SDP-ESC and extended SDP-ESC for global maximum search of example in Section 5.3.2

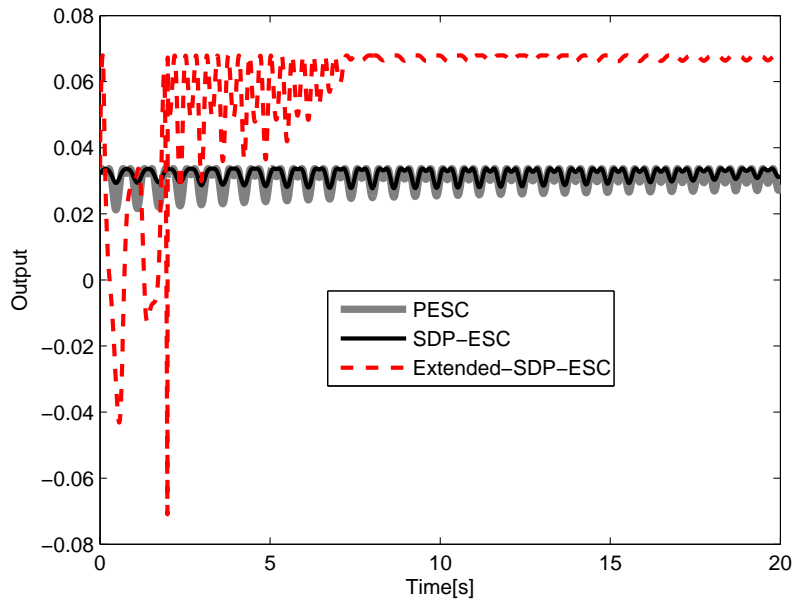


Figure 5.8: Output of example 5.3.2

converges to the GM at $u = 1.68$. Fig. 5.11 illustrates the output of (5.4) with the PESC, the SDP-ESC, and the extended SDP-ESC. It require approximately 2s for

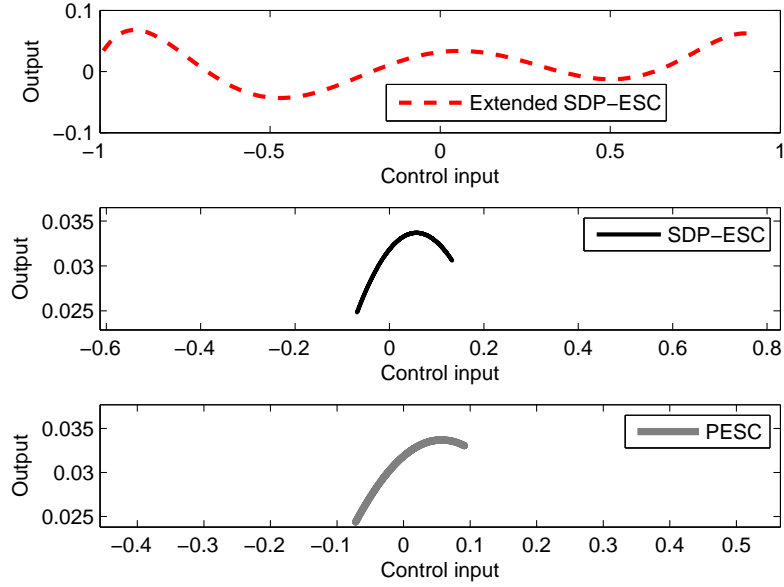


Figure 5.9: Input-output map of example 5.3.2

the extended SDP-ESC to converge to the GM and less than 10s to exponentially decay in order to reduce oscillations. Fig. 5.12 illustrates input-output map of system in (5.4) searched using the PESC, the SDP-ESC and the extended SDP-ESC. Compared to the PESC, the SDP-ESC, the extended SDP-ESC is able to scan all available maxima within operating range and converge to the actual GM.

Remark 4 β of the extended SDP-ESC should be selected such that it is small, but sufficient, to perturb the system. When a large β is selected the extended SDP-ESC may result into large oscillations, i.e., equivalent to those of the standard PESC.

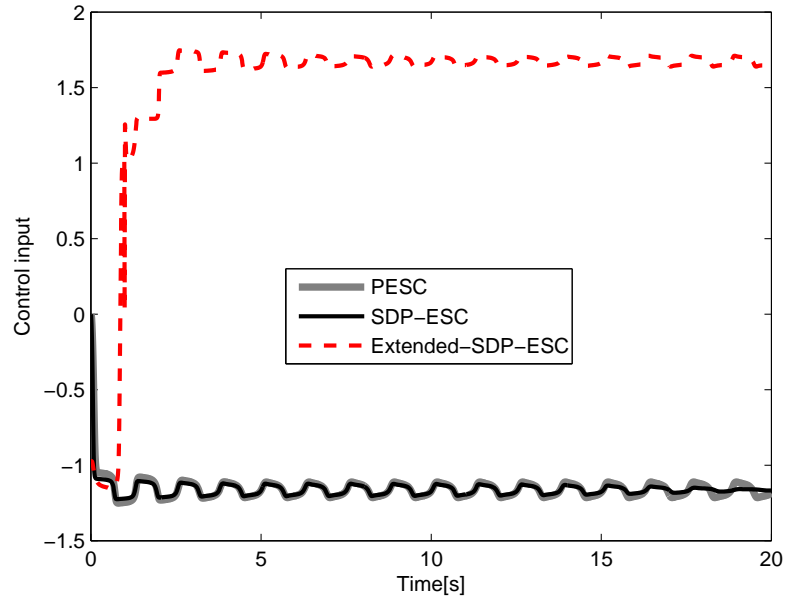


Figure 5.10: Control input for PESC, SDP-ESC and extended SDP-ESC for global maximum search of example in Section 5.3.3

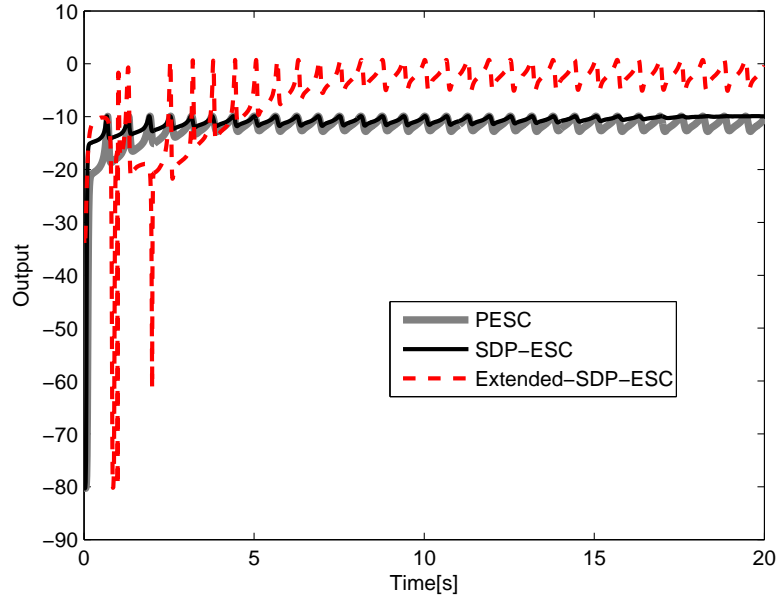


Figure 5.11: Output of example in Section 5.3.3

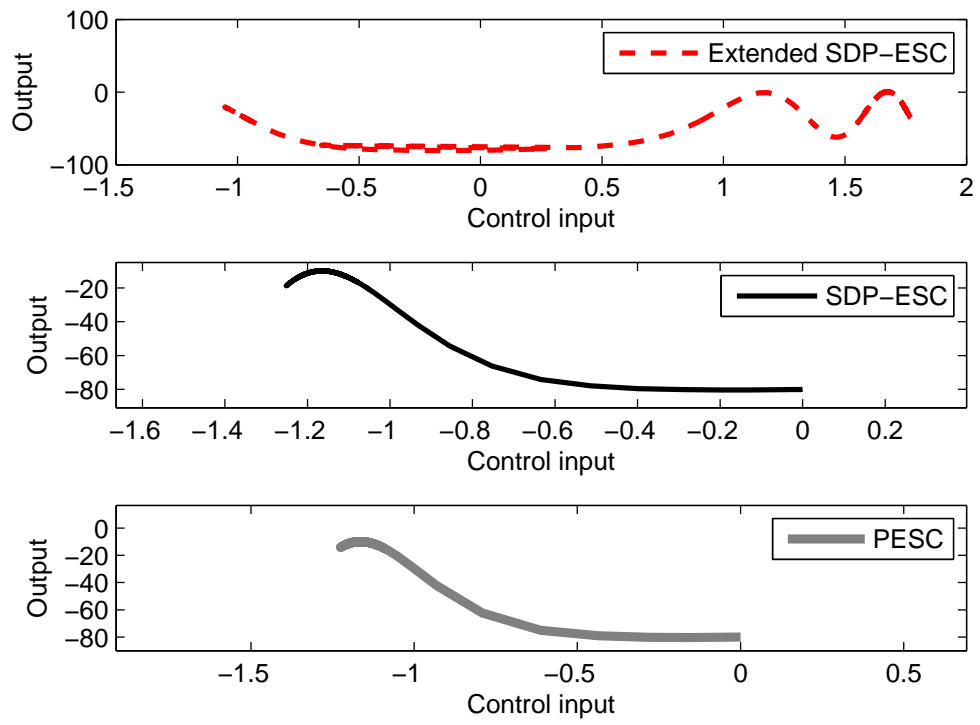


Figure 5.12: Input-output map of example in Section 5.3.3

5.3.4 Plant with dynamics: Example 4

Consider a nonlinear system given as

$$j(u) = -u^6 - 3u^3 + u + 1 \quad (5.5a)$$

$$D_i(s) = \frac{1}{3s + 1} \quad (5.5b)$$

$$D_o(s) = \frac{1}{0.2s + 1} \quad (5.5c)$$

where, $j(u)$ in (5.5a) has two maxima $j_1 = 2.12$ and $j = 1.21$ at $u = -1.11$ and $u = 0.33$, respectively. $D_i(s)$ and $D_o(s)$ are input and output dynamics, respectively. The maxima are located between -2 and 3 . $T_s = 0.01$ is selected, therefore based on (5.1), $W = 300$ samples. As illustrated in Fig. 5.13, both the PESC and the SDP-ESC converge to the neighbourhood maximum at $u = 0.33$. On the other hand, the extended SDP-ESC converges to the GM at $u = -1.11$. As shown in Fig. 5.14, due to the presence of the input/output dynamics, the time taken for the extended SDP-ESC to converge to the GM is increased. It takes approximately $30s$ for the extended SDP to converge to the GM and another $20s$ to exponentially decay the perturbation gain in order to minimise oscillations. Table. 5.2 presents the tuning parameters for the PESC, the SDP-ESC and the extended SDP-ESC.

Parameter	PESC	SDP-ESC	Extended SDP-ESC
α	-	10^{-6}	10^{-6}
β	0.1	0.1	0.1
$\omega_h \left[\frac{rad}{s} \right]$	2.5	2.5	2.5
$\omega \left[\frac{rad}{s} \right]$	5	5	5
$\varphi [rad]$	$\frac{\pi}{2}$	$\frac{\pi}{2}$	$\frac{\pi}{2}$
k	1	1	1
$W \left[\frac{Tp}{Ts} \right]$	-	-	300
C_p	-	2	2
C_z	-	1	1

Table 5.2: PESC and SDP-ESC and extended SDP-ESC tuning parameters for plant with dynamics

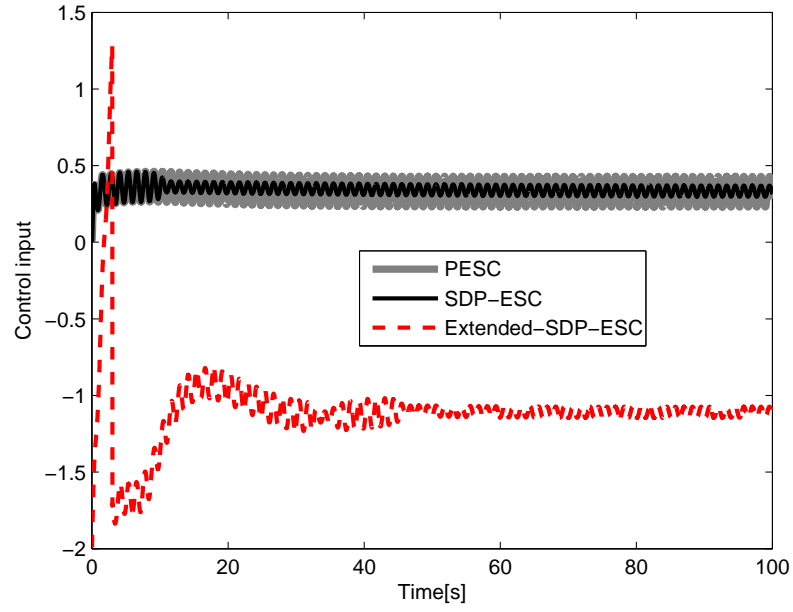


Figure 5.13: Control input for PESC, SDP-ESC and extended SDP-ESC for plant with dynamics

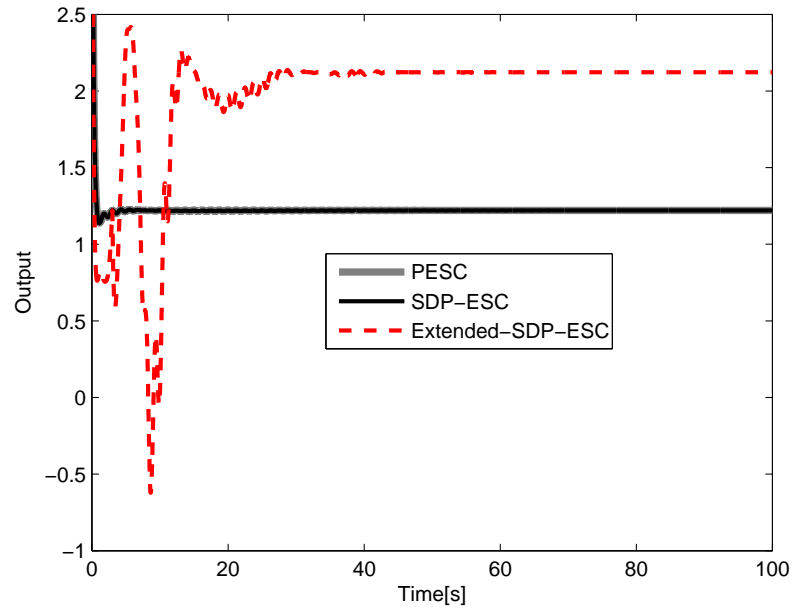


Figure 5.14: Output of example in Section 5.3.4

5.4 Critical appraisal and conclusions

In this chapter, a novel scheme for the GM search in the presence of local maxima has been presented. The scheme is based on an extension of the SDP-ESC scheme presented in Chapter 4. The extended SDP-ESC algorithm has been demonstrated using several examples comprised of multiple maxima. The proposed scheme has been shown to be effective in converging to the GM regardless of the available number of maxima. Some of the advantages of the proposed scheme are: it preserves the stability and simplicity of the SDP-ESC, it converges quickly to the GM, it can be applied for local maxima search, and it does not require any cost function. The convergence period is based on the control input operational range as well as the step size of the searching window. When a large step size is selected, a faster convergence speed to the GM will be achieved. However, when very a large step is selected the extended SDP-ESC may barely converge to the true GM. On the other hand, a smaller step will guarantee convergence to the true GM almost every time. This may however result in a slow convergence.

Chapter 6

Simulation study: Application in thermoelectric generator systems

6.1 Introduction

This Chapter presents simulation studies of the MPPT algorithms discussed in Chapter 2, 3 and 4 in application to the TEG system. Some of the results in this Chapter were also published in Phillip et al. (2013). In the last decade, investigation into TEGs for waste heat recovery in automotive applications has seen several advancements and the operational understanding of TEGs as a system has significantly improved. This is attributed to initial developments of models for the estimation of fuel economy benefits (Hussain, Brigham & Maranville 2009, Stobart & Milner 2009), more in-depth modelling and design of heat exchangers (Crane & Jackson 2002, Esarte, Min & Rowe 2001) and TE module subsystems (Montecucco, Buckle & Knox 2012, Lineykin & Ben-Yaakov 2007), as well as research into material selection (Rowe 2005, Snyder & Toberer 2008). As aforementioned in Chapter 1, despite these advances the science of TEGs still remains open to research in many areas. One such area is the optimisation of the electrical interface between a TEG system and a load for mismatch reduction.

MATLAB/Simulink has been used for the modelling and simulation of the TEG system as well as for the implementation of the control strategy. This chapter is organised as follows: Section 6.2 and Section 6.3 present an overview of the TEG system and modelling of the PCU subsystem, respectively. Section 6.5 and Section 6.6 presents two Phases of simulation studies, i.e., Phase I and Phase II, respectively. Phase I presents advantages of using an MPPT algorithm as well as comparison between P&O and PESC algorithms. Section 6.5.1 presents findings and observations of the simulation study of Phase I. Phase II presents improved results with the use of the VBS-ESC and the SDP-ESC, where PESC and LBS-ESC serves as benchmarks. Section 6.7 presents critical appraisals and conclusions.

6.2 TEG overview

TEGs are devices which use a temperature difference to generate electricity. The conversion is based on the phenomenon known as the Seebeck effect, named after Johann Seebeck who discovered the phenomenon in the early 18th century (Rowe 2005). Essentially such an effect is formed, when two dissimilar metals of N-type and P-type semiconductor material are connected together and give rise to a thermoelectric module (TEM), as shown in Fig. 6.1. By keeping the junction of these metals at different temperatures an electric voltage is generated. However, the generated voltage depends on other factors such as size of the TEM and the types of materials used. Performance of the material is typically quoted using the figure of merit denoted Z (Rowe 2005). The figure of merit Z of the material is given as

$$Z = \frac{\sigma S^2}{k_{th}} \quad (6.1)$$

where, σ denotes electrical conductivity (S/m), k_{th} denotes thermal conductivity [$\frac{W}{m.K}$] and S denote the Seebeck coefficient [$\frac{V}{K}$]. For the intended automotive

This material has been removed from this thesis due to Third Party Copyright. The unabridged version of the thesis can be viewed at the Lanchester Library, Coventry University.

Figure 6.1: Thermoelectric module (TEM)
(Snyder & Toberer 2008)

application, the heat source to provide the hot side is taken from the exhaust as shown in Fig. 6.2. To ensure minimal degradation to engine performance and emissions, the TEG unit is positioned between the catalyst and the muffler, which is also beneficial for packaging purposes. To provide the cold side, either the coolant circuit from the engine is used or in the case of hybrid-electric vehicles, the coolant loop for the power electronics and electric motors can also be used. The converted electrical energy that is generated, given a temperature difference, is used to charge the 12V battery. Due to transient unsteady heat flow, electrical output varies throughout the operation. The steady flow that is required however is made possible by making use of a PCU which contains a DC-DC converter with a MPPT algorithm to regulate the required voltage and simultaneously output

the maximum possible power for the highest PCU efficiency.

This material has been removed from this thesis due to Third Party Copyright. The unabridged version of the thesis can be viewed at the Lanchester Library, Coventry University.

Figure 6.2: Block diagram of waste heat recovery from engine exhaust
(Phillip et al. 2013)

The TEG model developed by Phillip et al. (2013) has been used as a tool to investigate the performance of the developed MPPT algorithms in this Thesis. The TEG model comprises three systems, namely: HX, TEM and PCU. Fig. 6.3 illustrates the input/output relations between the individual subsystems. Inputs to the HX subsystem are: exhaust temperature denotes $T_e(K)$, coolant inlet temperature denotes $T_w(K)$, exhaust mass flow rates denotes $\dot{m}_e \left[\frac{kg}{s} \right]$ and coolant inlet mass flow rates $\dot{m}_w \left[\frac{kg}{s} \right]$. The gas to liquid HX takes these four inputs to simulate the hot and cold side temperatures, $T_h(K)$ and $T_c(K)$, for the TEM. The TEM system utilises hot and cold side temperatures as the input to generate the voltage, $V_{in}(V)$, and current, $I_{in}(A)$ as its outputs. Equations (A.1a) and (A.1b) are used within the TEM to compute V_{in} and I_{in} . V_{in} and I_{in} are used as inputs to the PCU where the voltage, V_{out} and current I_{out} are the outputs. The resulting power out to the load is regulated at 14.4V by a synchronous DC-DC buck-boost converter. The load in this case is the 12V car battery. Based on

the fact that the contributions in this Thesis are focused on the PCU subsystem further more emphasis (details) on modelling of the PCU will be given in the forthcoming sections. Further detailed description of the TEG model in given is appendix A

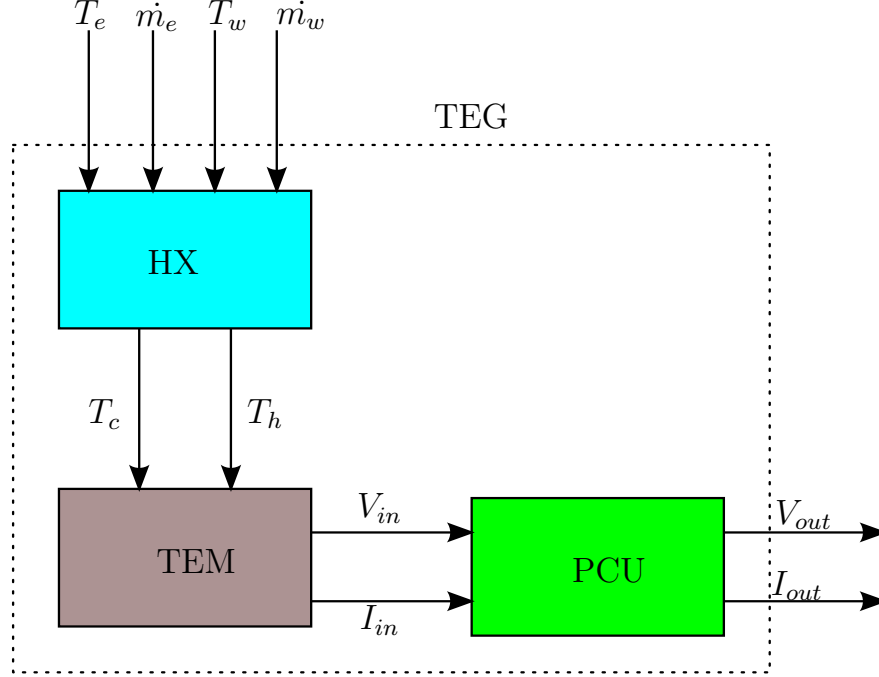


Figure 6.3: TEG model integration of subsystems

6.3 Power conditioning unit (PCU) modelling

As aforementioned in Chapter 1, a PCU comprises the DC-DC converter and the MPPT controller. One of the key factors in designing TEG systems is to match the impedance between the TEG and the load. Mismatch power loss of a TEG system is due to its transient nature and variance in the temperature distribution of the heat source; and also because of the connection topology of the TEMs. If all the TEMs in the system are connected in series, the mismatch in power output occurs due to the drastic change in the temperature gradient along the length of the HX where TEMs at lower temperatures act in a parasitic manner onto the

TEMs at the high temperature region. The need for a PCU is thus essential in a system which comprises of unstable heat sources and loads for outputting power at a fixed voltage.

6.3.1 DC-DC converter modelling

A DC-DC converter is an electronics circuit that converts a source of DC from one voltage level to another (Maganga, Larkowski & Burnham 2012). There are several DC-DC converter topologies which can be used within a PCU. For instance, in Phillip et al. (2012), two DC-DC converters namely the single ended primary inductor capacitor (SEPIC) and the buck-boost converter were used within the PCU where the latter is suggested to provide higher efficiency. Taking into account the advantage of stepping up or down without inverting (reversing terminals) its output voltage as well as having higher efficiency than a standard buck-boost, in this Thesis a synchronous DC-DC buck-boost converter is considered. As shown in Fig. 6.4, a synchronous DC-DC buck-boost comprises of an input filter capacitor denoted C_{in} , a Schottky power diode denoted D4, three metal-oxide-semiconductor field-effect transistors (MOSFETs) denoted M1, M2, M3, and an output filter capacitor denoted C_{out} . The Schottky power diode D4 replaces the commonly used fourth MOSFET to block the reverse current flow and prevent the battery connected at the output from discharging through the converter during discontinuous conduction mode (DCM). Also, M1 and M3 and must be on-state while M2 is in the off-state. The converter provides a controllable and/or constant output DC voltage despite variation of the input voltage.

Similar to the standard buck-boost converter, the synchronous DC-DC buck-boost converter operates in two different modes, namely a continuous conduction mode (CCM) and a DCM. In CCM, the inductor current flows continuously for the entire period and never falls to zero. On the other hand, in the DCM, the in-

This material has been removed from this thesis due to Third Party Copyright. The unabridged version of the thesis can be viewed at the Lanchester Library, Coventry University.

Figure 6.4: Schematic diagram of a synchronous DC-DC buck-boost converter (Maganga et al. 2014)

ductor current reduces to zero and remains at a zero level for the remainder of the period before it begins to rise again (see Fig. 6.5). In this Thesis, the synchronous DC-DC converter is considered to operate in the DCM mode. Advantages of the DCM operation over the CCM are: no zero is located at the right half plane in the s-domain which allows for a higher transient response bandwidth. Zero in the right half plane in s-domain is nearly impossible to compensate. Also, while operating in DCM, the converter is considered to have a single pole transfer function which is easier to compensate for compared to a double pole response. On the other hand, compared to CCM, DCM requires larger inductors/transformers for the same output power. A high-fidelity white-box model of a synchronous DC-DC converter with each component modelled by including its corresponding physical characteristics, is developed in Simulink/Simscape environment. Consequently, it is deemed that this model provides a realistic representation of a real synchronous DC-DC buck-boost converter. Here, a synchronous DC-DC buck-boost converter for a low power application with a variable input voltage and the output voltage regulated at 12V is considered.

In order to design a synchronous DC-DC buck-boost which provides high efficiency, the design criteria plays a major role. One such criteria is the appropriate

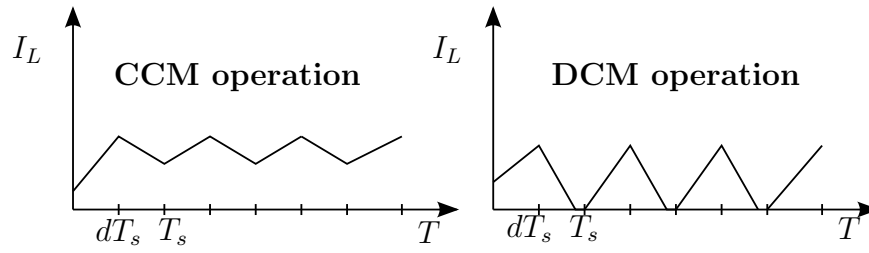


Figure 6.5: Waveform for CCM and DCM, where dT_s denote period when switch is closed and T_s denote switching period

sizing and selection of individual components, in particular, elements that result in low power losses. Here, the component sizing focuses on the selection of the inductor and the output filter capacitance. Components are sized to allow the synchronous DC-DC converter to operate at a switching frequency of $20kHz$. The minimal value of the inductance required, i.e. L_{min} , is calculated as

$$L_{min} = \frac{R_{L(max)}}{2f_s} (1 - d_{min})^2 \quad (6.2)$$

where: $R_{L(max)}$ is the maximal load resistance, f_s is the switching frequency and d_{min} is the minimal duty cycle. The minimal value of the output filter capacitance C_{min} is calculated as follows

$$C_{min} = \frac{d_{min}}{f_s R_{L(min)}} \frac{V_{out}}{V_{rcpp}} \quad (6.3)$$

where: $R_{L(min)}$ is the minimum load resistance, V_{out} is the output voltage and V_{rcpp} the ripple voltage across the filter capacitor. As the V_{out} is considered to be constant, a change in the input voltage V_{in} and the duty cycle d will only affect the output current I_{out} . At steady-state the input current I_{in} and the output current I_{out} are related as

$$I_{out} = \frac{(1 - d)}{d} I_{in} \quad (6.4)$$

	Name	Unit	Value
	Inductor (L)	uH	33
	Input capacitor (C_{in})	uF	470
	Output capacitor(C_{out})	uF	220
	Diode forward voltage(V_D)	V	0.8
	On resistance MOSFET (R_{on})	Ω	0.008

Table 6.1: Design parameters for synchronous DC-DC buck-boost converter model

6.3.2 Control technique modelling:

The control strategy for the MPPT converter is implemented in two different subsystems, namely the pulse width modulator (PWM) and the MPPT controller. The PWM is modelled such that it compares the ramp signal with the variable duty cycle which is generated by the MPPT controller. If the difference of these signals is greater or equal to 0, then the value will be held at the same value for one period and then wait for the new value of the duty cycle. The resultant waveform in Fig. 6.6 illustrates the PWM generated for the variable duty cycle. The MPPT controller is implemented with 5 different control algorithms which are: *P&O*, *PESC*, *LBS-ESC*, *VBS-ESC*, and *SDP-ESC* and their Simulink models are presented in appendix B.

6.4 MPPT performance criterion

There are several ways of assessing the performance of a given system. For instance, the performance can either be assessed based on tracking error, MPPT efficiency or percentage accuracy, etc. (see definition in section) The performance criterion for the MPPT converter can either be measured by energy efficiency, available power or input voltage at the MPP. Energy efficiency at MPP is given as

$$\eta_e = \frac{P_{cov}}{P_{mpp}} 100\% \quad (6.5)$$

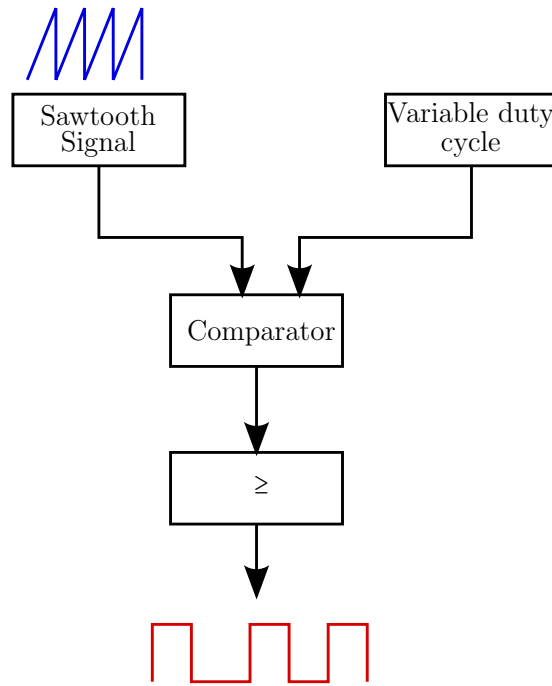


Figure 6.6: Block diagram for the pulse width modulation (PWM)

where: η_e denotes MPPT converter efficiency, P_{cov} denotes power absorbed by the converter and P_{mpp} denotes power available from the TEG. For the TEG it is considered that at MPP, the input voltage is half of the open circuit due to load matching, i.e.,

$$V_{in} = V_{mpp} = \frac{V_{oc}}{2} \quad (6.6)$$

Theoretically the maximum available power from the TEG can be calculated as

$$P_{mpp} = \frac{V_{oc}^2}{4R_{in}} \quad (6.7)$$

where: R_{in} is the internal resistance of the TEG. Hereafter criterion (6.5), (6.6) and (6.7) will be used as the performance index as well as other factors such as speed of convergence and limit cycle minimisation.

6.5 Simulation study: Phase I

This section presents the simulation results of the TEG with the use of a fixed duty cycle, P&O and PESC algorithms. When a MPPT controller is not used within the PCU (i.e. a synchronous DC-DC converter is driven by a fixed duty cycle) this is termed as a fixed duty cycle control. Operating a converter with a fixed duty cycle is aimed to demonstrate the benefits of using a MPPT controller. When the synchronous DC-DC converter is driven at a fixed duty cycle, simulation results show that it is only for the $700K$ to $800K$ temperature range that a reasonable output power is achieved. Table. 6.2 presents a range of fixed duty cycle values for various temperatures as well as corresponding input voltage values at matched load for the specific system configuration. This is considered to be due to the inability of the controller to remove the mismatch of the internal resistance values between the TEG and the DC-DC converter over a wider range of temperatures.

When a fixed duty cycle is used, it implies that the controller will provide optimal performance only at a specific operating point. This justifies the need for an MPPT controller. For the results presented in this Section, the fixed duty cycle has been set to 48.53% for optimal performance at $700K$. At the user's discretion the duty cycle can be changed for high efficiency at different temperature ranges. Knowing the characteristic of a TEG system, a look-up table can be used to store optimal duty cycle values at different operating temperatures. This process, i.e., an empirical process, however only works for a specific configuration. ESC on the other hand, i.e., non-constraints based, can be reconfigured to any system (e.g. a different power source). The duty cycle can be calculated using (6.4) if the DC-DC converter input voltage at match load is known. Table. 6.3 shows the output power of the TEG comparing the implementation of a fixed duty cycle, P&O and ESC (i.e. PESC), as well as the efficiencies of each MPPT method compared to ideal matched load (power at MPP) results. For the simulation

$\Delta T(K)$	V_{mpp}	$d\%$	V_{Bat}
600	10.93	56.85	14.4
700	15.27	48.53	
800	19.68	42.25	
900	24.11	37.39	

Table 6.2: Optimum duty cycle at corresponding temperatures

results presented, the hot side temperature varies from $600K$ to $900K$ and the cold side temperature is maintained at $363K$. Simulation results demonstrate that both the P&O and the PESC converge to a similar output power. When compared to the P&O however, the output power of the PESC converges much faster to the MPP, as is illustrated in Fig. 6.7.

This material has been removed from this thesis due to Third Party Copyright. The unabridged version of the thesis can be viewed at the Lanchester Library, Coventry University.

Figure 6.7: Simulation results for theoretical power, output power with ESC, P&O and Fixed Duty Cycle: Losses reduced to within 5%
(Phillip et al. 2013)

	Power at MPP	Fixed d	Fixed d	P& O	P& O	PESC	PESC
Temp(K)	P(W)	P(W)	$\eta_e\%$	P(W)	$\eta_e\%$	P(W)	$\eta_e\%$
600	47.61	40.80	85.70	46.50	98.19	47.40	99.56
700	90.00	87.40	97.11	88.37	98.18	89.00	98.87
800	144.72	132.60	91.63	141.00	97.43	142.50	98.47
900	210	177.60	83.37	204.40	97.10	206.60	98.15

Table 6.3: TEG results with different MPPT algorithms

6.5.1 Findings and observations

The results obtained in Phase I show that the PESC MPPT algorithm in combination with a synchronous buckboost DC-DC converter is able to condition the output power of the TEG device effectively. This finding reinforces the case for utilising the PESC approach as a candidate for an efficient MPPT algorithm for use in PCUs for TEGs. After conducting experimental work using hardware in the loop (HIL) testing however, these findings were inconclusive. Limitations found in the HIL testing are discussed in detail in Chapter 7. These findings lead to the development of the novel algorithms presented in previous chapters. Upcoming sections present simulation studies of the TEG with novel MPPT schemes.

6.6 Simulation study: Phase II

This Phase presents improved results at both transients and steady-state. Performance of the PESC, the LBS-ESC, the VBS-ESC and the SDP-ESC were analysed using an emulated TEG Simulink model. Convergence speeds of the MPPT algorithms were determined by setting the PSU voltage at $12V$ and $R_{in} = 6.8\Omega$. In order to achieve a fast convergence speed, the SDP-ESC was initialised with a large value of k , therefore no compensator was needed within SDP-ESC feedback loop. The compensator was omitted simply by setting values of C_z and C_p equal to 1. Also, as aforementioned in Chapter 3, the LBS-ESC MPPT algorithm required linearisation (computing its Jacobian) around its equilibrium.

The Jacobian of the LBS-ESC is calculated using the design parameters shown in Table. 6.4. Substituting these parameters in (3.41) in Section (3.4.1), the Jacobian is given as

$$J = \begin{bmatrix} 0 & 20 & 0 \\ -2.5 & -50 & 0 \\ 0 & 0 & -25 \end{bmatrix} \quad (6.8)$$

Utilising (6.8), the P matrix of the Lyapunov function is obtained by solving (3.42) in Section 3.4.1. The P matrix is given as

$$P = \begin{bmatrix} -0.59 & -0.025 & 0 \\ 0.025 & -0.0113 & 0 \\ 0 & 0 & -0.02 \end{bmatrix} \quad (6.9)$$

The symmetric matrix of P , i.e., Q , is selected as identity (i.e.)

$$Q = \begin{bmatrix} -1 & 0 & 0 \\ 0 & -1 & 0 \\ 0 & 0 & -1 \end{bmatrix} \quad (6.10)$$

The Lyapunov function $V(x_\beta)$ governs switching based on the calculation of \tilde{x}_β which comprises of \tilde{u}_β . Inaccurate estimates of \tilde{u}_β may cause the LBS-ESC to fail to satisfy the switching conditions. This can either cause the LBS-ESC to generate into the standard PESC, or fail to adapt the changes due insufficient perturbation to the LBS-ESC scheme. This problem can be avoided by selecting appropriate parameters for ϵ_{lbs} and g . On the other hand, it is relatively difficult to obtain appropriate values for ϵ_{lbs} and g for a wide range. Simulation results shows that while the PESC, the LBS-ESC and the VBS-ESC take around $250ms$ to reach steady-state, the SDP-ESC take only $150ms$ to converge to the steady-state (see

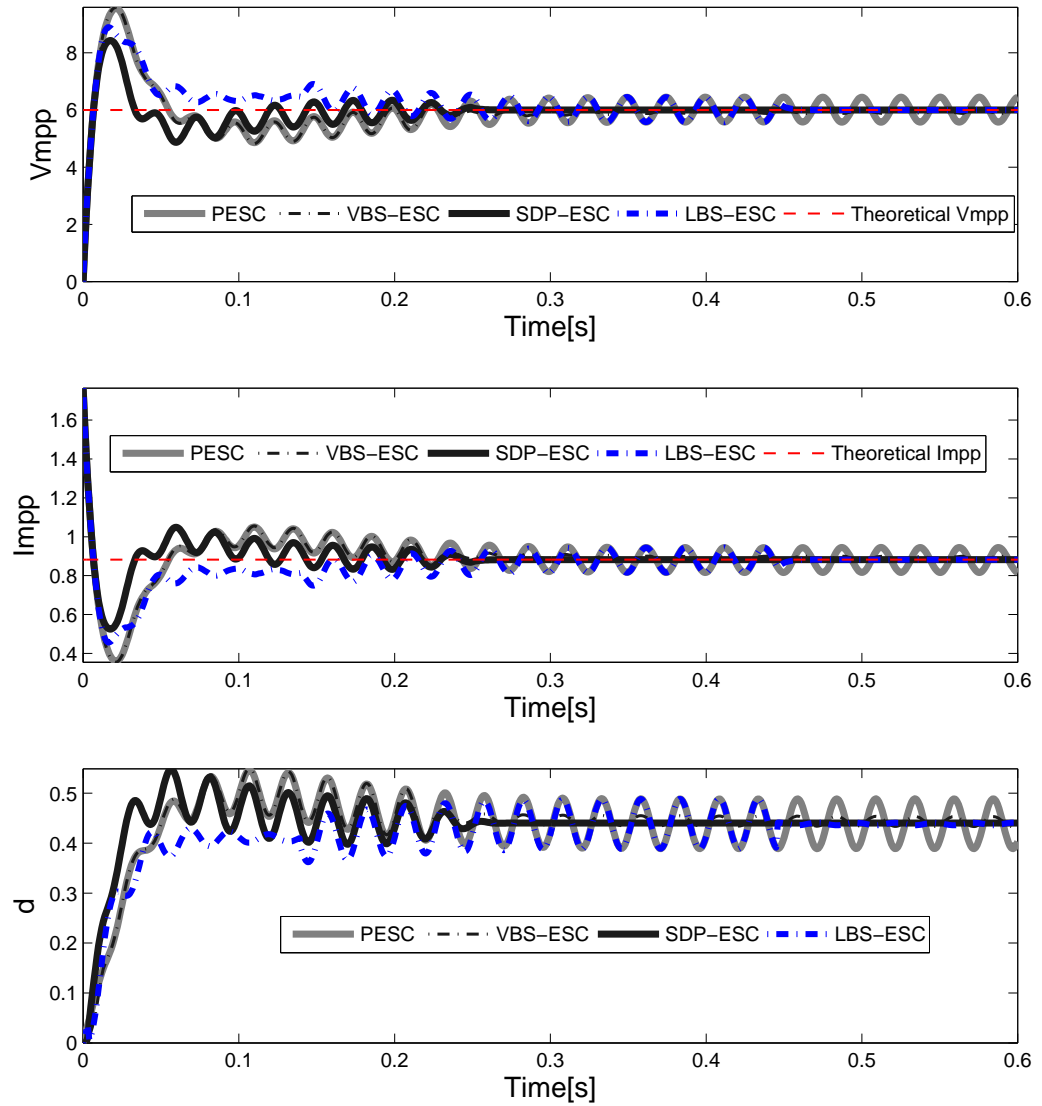


Figure 6.8: Simulation results of V_{mpp} , I_{mpp} and d using PESC, LBS-ESC, VBS-ESC and SDP-ESC MPPT algorithms

Fig. 6.8). Once the SDP-ESC enters stable limit cycle, it then requires another 100ms to decay exponentially in order to minimise electrical losses within the PCU. Although both LBS-ESC and VBS-ESC minimises losses, both require a much longer time to converge compared to the SDP-ESC. Fig. 6.11 illustrates the variance of the state \hat{x} with respect to time. The variance of the signal \hat{x} is

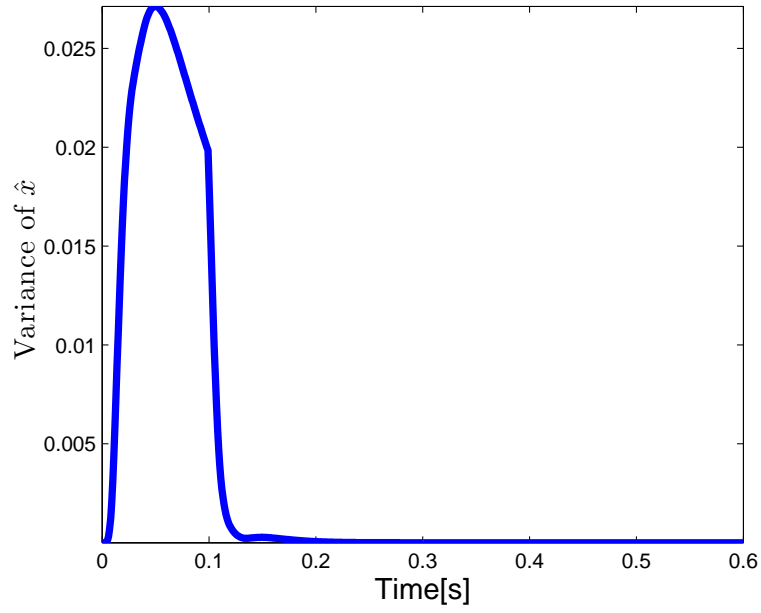


Figure 6.9: Variance of state \hat{x} for SDP-ESC scheme

Parameters	PESC	LBS-ESC	VBS-ESC	SDP-ESC
k	20	20	20	25
β	0.05	0.05	n/a	0.05
β_{max}	n/a	n/a	0.05	n/a
β_{min}	n/a	n/a	0.01	n/a
ω	250	250	250	250
ω_h	25	25	25	150
ω_l	50	50	50	100
ϕ	0	0	0	0
α	10^{-5}	n/a	n/a	n/a
Cp	n/a	n/a	n/a	1
Cz	n/a	n/a	n/a	1
g	-0.05	n/a	n/a	n/a
ϵ_{lbs}	n/a	-0.0565	n/a	n/a
ϵ_{vbs}	n/a	0	$2.5 \cdot 10^{-6}$	n/a

Table 6.4: Tuning parameters for PESC, LSB-ESC, VBS-ESC and SDP-ESC MPPT algorithms

increases rapidly, which indicates that the SDP-ESC scheme starts with a higher perturbation gain, and then decreases in order to minimise oscillations. Also, the performance of the MPPT algorithms at a different voltage range was tested by increasing from 12V to 16V with increment of 2V.

Simulation results shows that compared to the PESC, the VBS-ESC and the

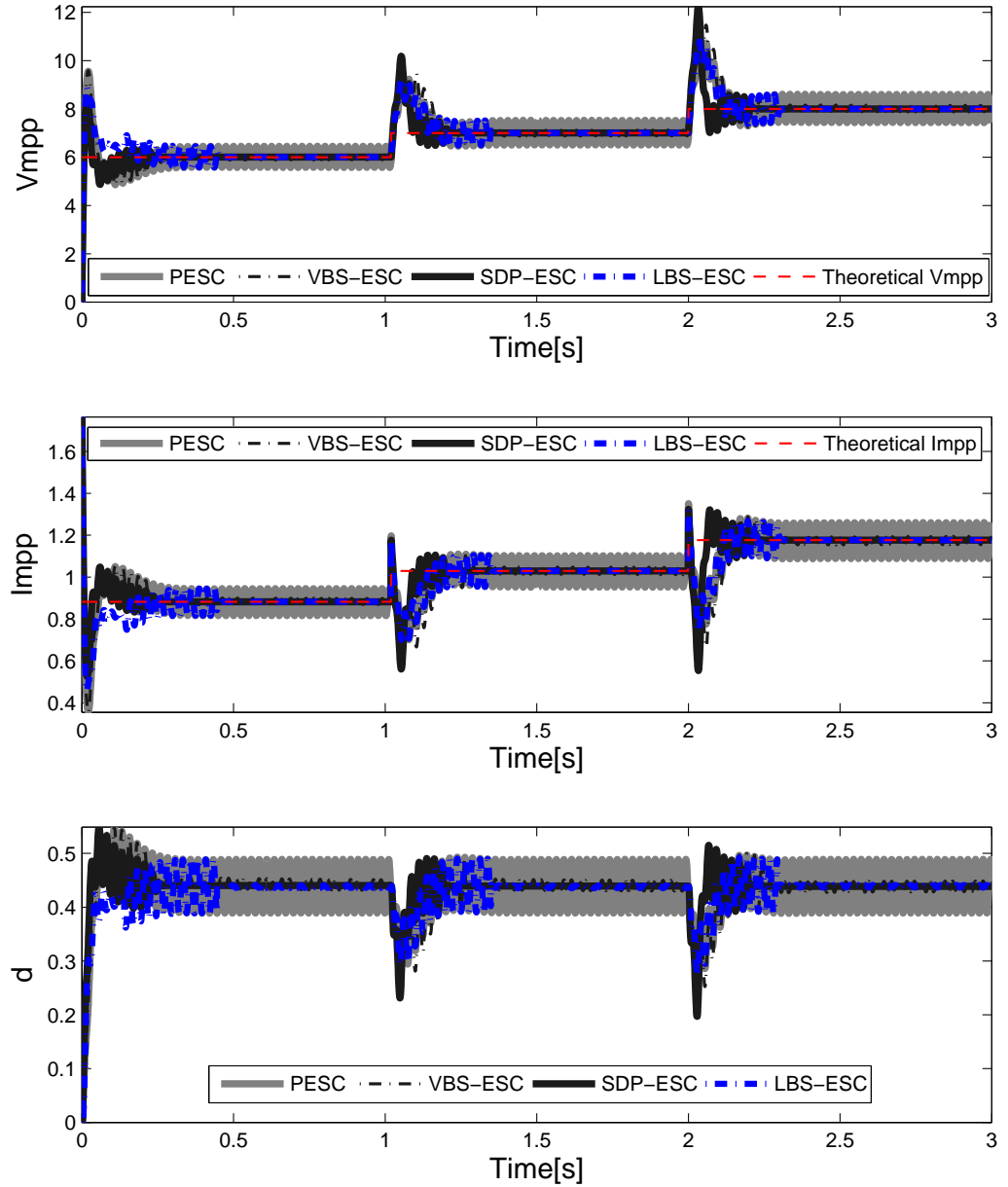


Figure 6.10: Simulation results for PESC, LBS-ESC, VBS-ESC and SDP-ESC MPPT algorithms while PSU voltage increased from 12V to 16V by step increment of 2V

LBS-ESC, the SDP-ESC achieves a faster convergence speed at different voltage ranges (see Fig. 6.10). Although the VBS-ESC and the LBS-ESC achieve a sim-

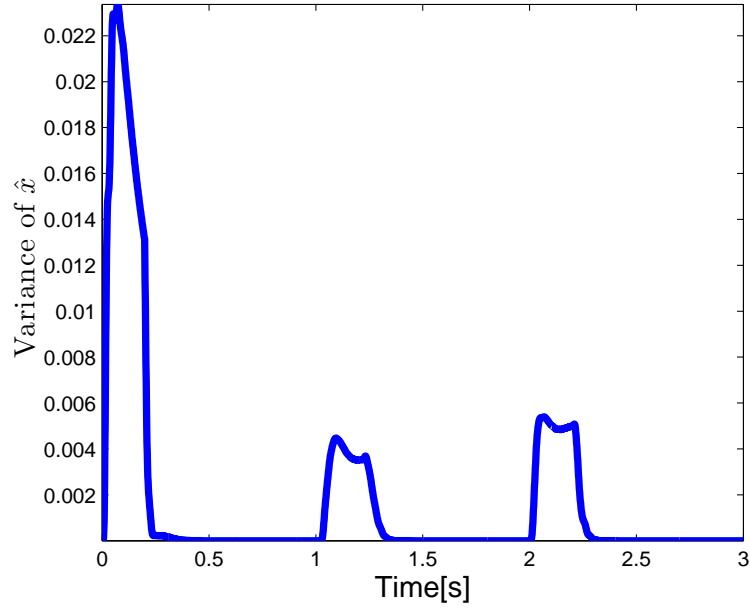


Figure 6.11: Variance of state \hat{x} for SDP-ESC algorithm while PSU voltage increased from 12V to 16V by step increment of 2V

ilar performance on limit cycle minimisation, it is relatively difficult to optimise LBS-ESC for optimal performance, due to its large number of tuning parameters. Based on the fact that the adaptation within SDP-ESC is achieved through an integrator gain when change is detected, the variance will also increase and start to decrease again as the system approaches steady-state. As shown in Fig. 6.11, the variance change of state \hat{x} is detected at three different voltage steps: $V_{oc} = 12V$, $V_{oc} = 14V$ and $V_{oc} = 16V$. Moreover, the performance of the MPPT algorithms for a varying voltage (i.e., increasing or decreasing), was performed by first increasing the PSU voltage from 12V to 16V and then reducing it from 16V to 14V. As shown in Fig. 6.13 Compared to the LBS-ESC, both the VBS-ESC and the SDP-ESC consistently perform for the entire tested range. On the other hand, LBS-ESC was unable to converge to the optimal current and voltage due to the failure of the switch within the LBS-ESC scheme to detect change (see Fig. 6.15).

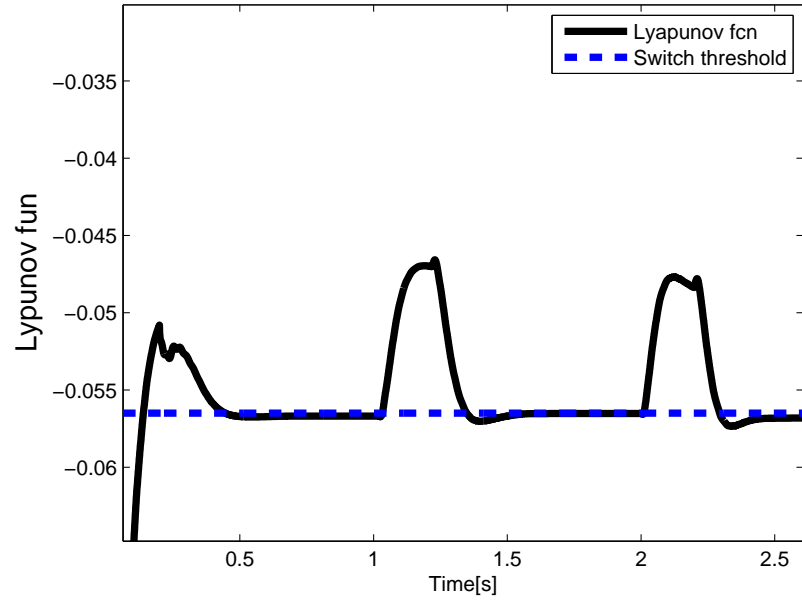


Figure 6.12: Lyapunov function for the LBS-ESC while PSU voltage increased from 12V to 16V by step increment of 2V

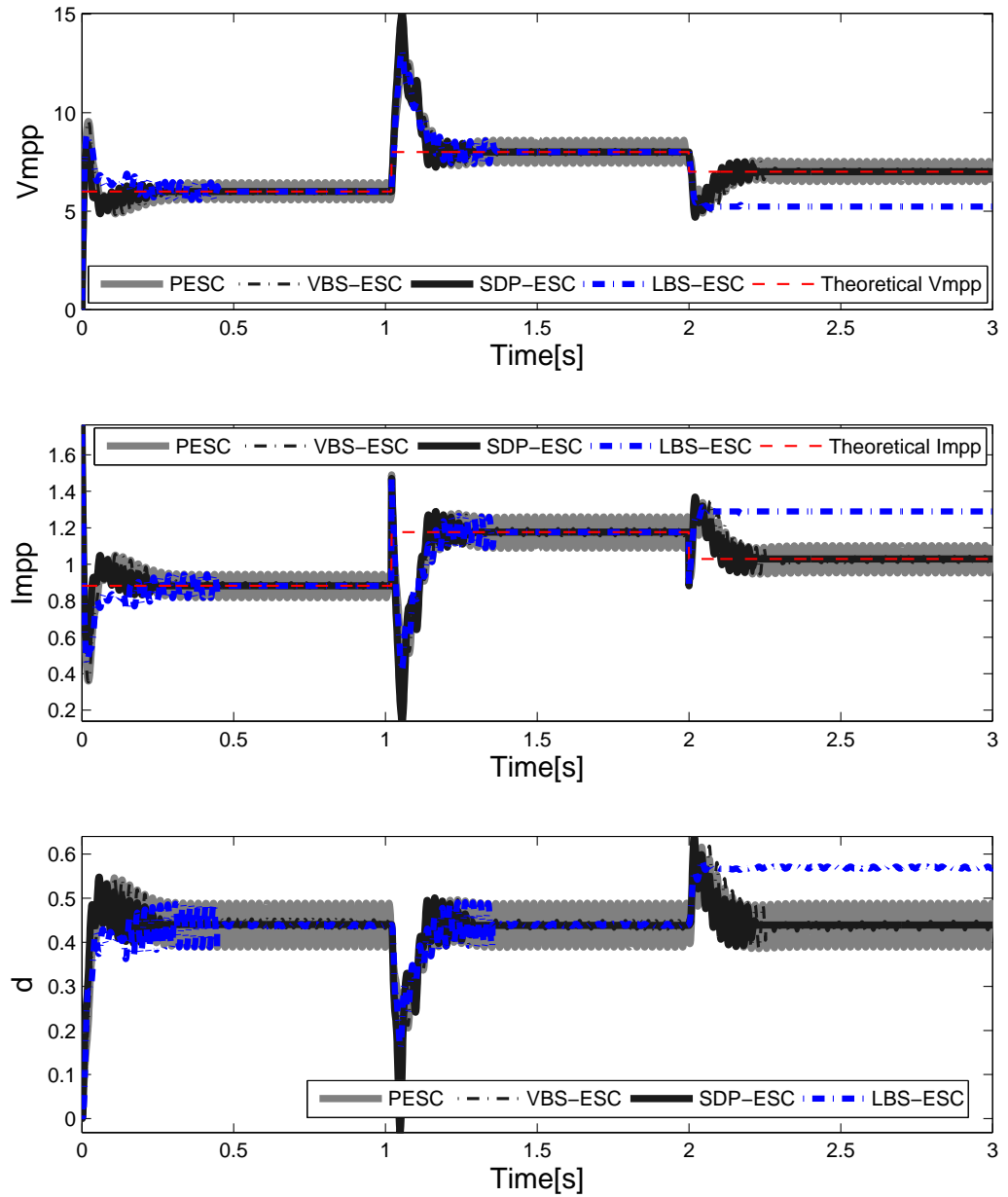


Figure 6.13: Simulation results for PESC, LBS-ESC, VBS-ESC and SDP-ESC MPPT algorithms while PSU voltage increased from 12V to 16V and then reduced from 16V to 14V

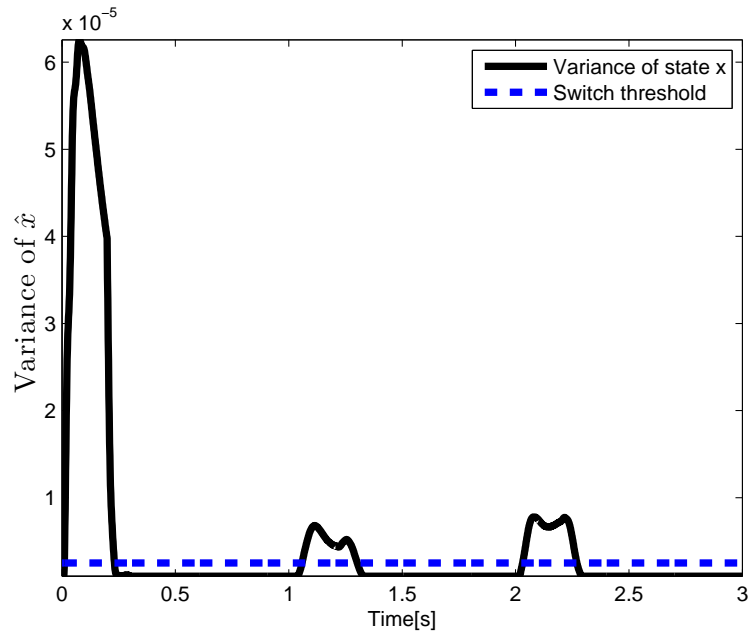


Figure 6.14: Variance of state \hat{x} for VBS-ESC algorithm while PSU voltage increased from 12V to 16V by step increment of 2V

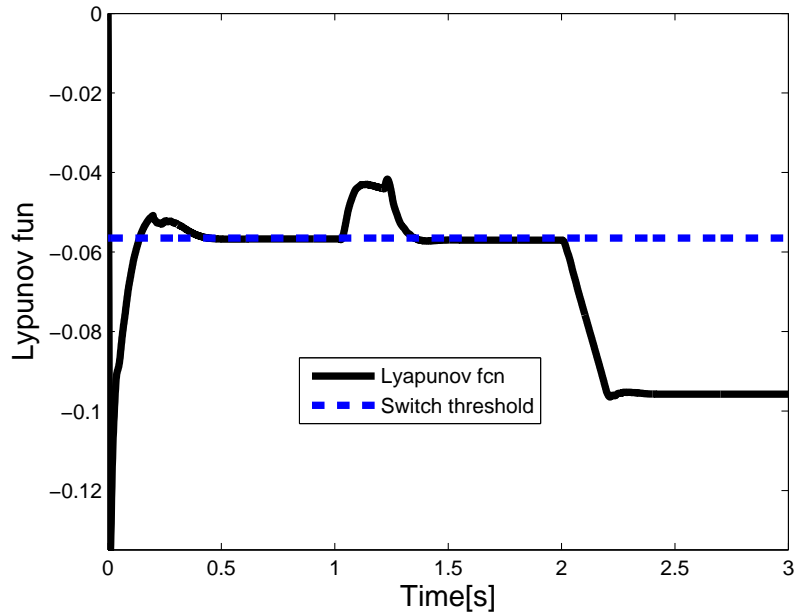


Figure 6.15: Lyapunov function for the LBS-ESC while PSU voltage increased from 12V to 16V and then reduced from 16V to 14V

6.7 Critical appraisal and conclusions

In this Chapter, two phases of simulation studies were presented. In Phase I, simulation results for the P&O and the PESC algorithms for the TEG were presented. Also, the benefit of using MPPT algorithms within the TEG was demonstrated by operating with and without (i.e. fixed duty cycle) MPPT algorithms. Simulation results show that in comparison to P&O, PESC achieves a faster convergence speed. Due to the limitations of the PESC observed in Phase I of hardware 7, Phase II presents improved results using novel MPPT algorithms for both transients and steady-state. The VBS-ESC and the SDP-ESC schemes were compared with PESC and LBS-ESC schemes. Compared to others' schemes, SDP-ESC achieves a faster convergence speed with minimised electrical losses. This is due to an additional compensator as well as the ability to be initialised with a large perturbation gain. Also, compared to LBS-ESC, both VBS-ESC and LBS-ESC consistently perform for a varying source voltage.

Chapter 7

Experimental work

7.1 Introduction

This Chapter presents two Phases of the experimental validation of the simulation results presented in Chapter 6. Phase I demonstrates the performance of current existing MPPT algorithms and their limitations. In this phase, three different analyses were performed, namely, steady-state, transient using emulated TEG and transient via actual TEG. Steady-state analysis is conducted to investigate limit cycles and losses within the PCU. Transient analysis using emulated TEG is aimed to test the performance of the MPPT algorithms and their adaptation capability under rapid variations of terminal voltage. On the other hand, transient analysis with the real TEG system aims to investigate the performance of the MPPT algorithms for the slow dynamics of the TEG. The results of the experimental validation Phase I were published in Maganga et al. (2014). Phase II presents improved results with the use of the VBS-ESC and the SDP-ESC for similar analysis as that of Phase I. This chapter is organised as follows. Section 7.2 provides a description of the experiment-set up for Phase I. Section 7.2.5 and 7.2.6 presents experimental results with emulated TEG and actual TEG, respectively. Section 7.2.7 presents findings and observations of the experimental

Phase I. Section 7.3 describes the set-up of the experimental Phase II. This is followed by experimental results in Section 7.3.2 with emulated TEG and actual TEG in Section 7.3.3, utilising novel algorithms.

7.2 Experiment-setup: Phase I

This section describes the instrumentation and devices used to gather the experimental results obtained with actual TEGs and with an emulation behaviour of the TEGs. The actual TEG is used for transients analysis whereas emulation behaviour of the TEG is used for steady-state and fast transients analysis. Fig. 7.1 illustrates the schematic diagram of the connections between instrumentations and devices used for experimental tests. A battery is emulated using a PSU connected in series with an electronic load in constant-resistance mode, whereas TEG is emulated using a PSU connected in series with a resistor. A synchronous DC-DC buck boost converter is interfaced between the source (TEG/PSU) and the emulated battery. Inputs to the synchronous DC-DC converter are: current and voltage (i.e. V_{in}, I_{in}). Outputs of the converter are: voltage and current (i.e. V_{out}, I_{out}). Inputs and outputs of the converter are fed to dSPACE (i.e. MicroAutobox) as analog inputs which are used to manipulate the control inputs of the converter via MPPT algorithms implemented in MATLAB/Simulink in a PC. The manipulated control input is used to drive the PWM1 and PWM2 (see Fig. 7.1).

7.2.1 Synchronous DC-DC converter

The synchronous DC-DC buck-boost converter provided by Glasgow University was used for testing MPPT algorithms. The schematic of the synchronous DC-DC converter and its principle of operation were presented in Chapter 6. Input and output currents of the converter are sensed through the differential amplification

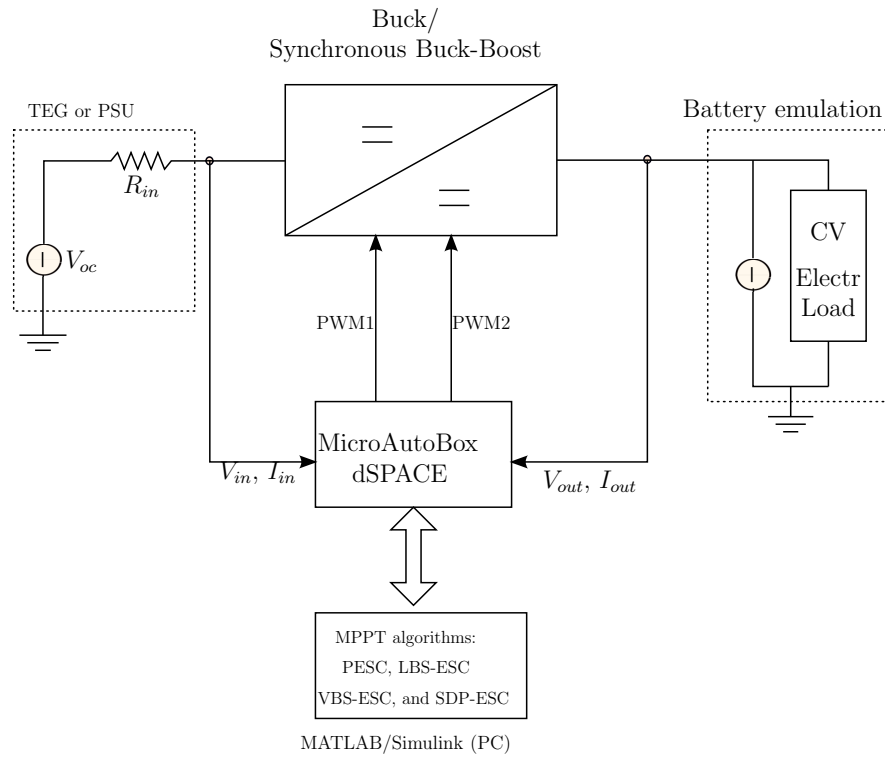


Figure 7.1: Schematic diagram of the connections between instrumentals and devices used for the experimental tests

of the voltage across high precision/ power sense resistors placed in series with the converter's input and output terminals. The nominal input power of the converter is $35W$ at $17.5V, 2A$. Its electrical efficiency at $34W$ input power ($11.35V, 3A$) is 88.2% . The converter's printed circuit board (PCB) is shown in Fig. 7.2.

Sensor accuracy

The synchronous DC-DC buck boost converter (see the schematic diagram in C.2) comprises of two current sensors: one for the input and one for the output current measurements. Each of the sensor has $\pm 10\%$ error. A small value of sensing resistor is used in order to keep the voltage drop on it small (with minimal losses). The voltage drop across the resistor is then amplified by a factor of 100 by a differential amplifier. The differential amplifier has a differential input voltage offset (in millivolts) that constitutes an error. This error is the which is amplified

This material has been removed from this thesis due to Third Party Copyright. The unabridged version of the thesis can be viewed at the Lanchester Library, Coventry University.

Figure 7.2: Picture of the top layer of the converters PCB. The bottom layer hosts the inductor and the capacitors.

by the differential amplifier, resulting in a fixed offset error in both input and output measurements.

7.2.2 dSPACE interface

The MicroAutoBox is a portable dSPACE hardware used for real-time application to perform various rapid control prototyping. MicroAutoBox is used in Phase I for hardware in the loop (HIL) testing. It comprises of multiple in-built PWM channels of which two are used to drive the MOSFET gate drivers of the synchronous buck-boost the DC-DC converter. Via the 'drives control center aligned' feature in the MicroAutoBox a dead-band of $400ns$ between PWM1 and inverted PWM2 is initialised. It provides a maximum switching frequency f_s of 20 kHz

which is used as the switching frequency for the converter. Four of the analog to digital converter (ADC) channels in the MicroAutoBox are used for obtaining measurements (V_{in} , V_{out} , I_{in} and I_{out}).

7.2.3 TEG test rig and electrical characterisation

In Phase I, the test rig provided by Glasgow University was used for testing the MPPT algorithm testing. Two commercial 40mm x 40mm TEG modules (GM250-127-14-10) were used in the experimental tests. Both TEG modules were tested separately to obtain their individual electrical characteristics at a constant mechanical load in the test fixture of 1920N, for three different temperature gradients: 100°C, 150°C and 200°C. The cold block water supply was maintained at 20°C for all Phase I testing. The assumptions proposed in chapter 3 and verified in chapter 4 are confirmed by the experimental work in chapter 7. In particular it can be observed on Fig. 7.3 that the TEG characteristics has a unique maximum as stated in Assumption 3, is differentiable as stated in Assumption 1 and the steady-state characteristic of the TEG is stable as stated in Assumption 2. The resulting V-I and P-I curves for TEG 2 are presented in Fig. 7.3, while Table. 7.1 lists the important electrical parameters for both TEG modules. The last column of Table. 7.1, namely variance, shows that the performance variance between the power output of the modules tested is less than 1%. This slight difference may be due to a small thermal impedance mismatch in the experimental apparatus or due to TEG manufacturing tolerances. A consequence of this difference is that when connected in series their combined output power will be slightly less than the sum of the individual powers. It must also be noted that the true MPP might be between two measured load values. The difference in power produced however will always be less than 0.5%. Considering these factors and the variance data in Table. 7.1, it can be concluded that the performance values provided in Table. 7.1 have a worst-case accuracy of 1% where $Var_{P_{mpp}} = |P_{mpp1} - P_{mpp2}|$.

Figure 7.3: Electrical characterisation for TEG-2 and for three different temperature gradients: 100 °C, 150 °C, and 200 °C between the hot and cold sides of the thermoelectric module.
(Maganga et al. 2014)

$\Delta T(^{\circ}C)$	$R_{in}(\Omega)$	$V_{oc}(V)$	$P_{mpp}(W)$	$R_{in}(\Omega)$	$V_{oc}(V)$	$P_{mpp}(W)$	<i>Variance</i>
100	1.81	4.52	2.82	1.79	4.51	2.83	0.6
150	2.01	6.91	5.91	1.97	6.86	5.92	0.2
250	2.16	8.83	8.97	2.14	8.83	9.04	0.8

Table 7.1: Electrical characteristics of the two TEG modules for three different temperature gradients: 100 °C, 150 °C, and 200 °C

7.2.4 Steady state analysis

The steady-state performance of the two MPPT algorithms was measured at three different temperature gradients: $\Delta T = 100^{\circ}C, 150^{\circ}C, 200^{\circ}C$. Fig. 7.4 illustrates the comparison of the P&O and the PESC algorithms with the experimental maximum TEG output power for the steady-state operation. Clearly, both algorithms are able to accurately track the MPP within 5% of the maximum output. These

results however are conservative and the power extracted by the two MPPT algorithms is often even closer to the MPP. When compared to the simulated outputs, the experimental results have a slightly lower accuracy which is due primarily to the various losses not incorporated within the simulation model, as well as the electrical noise present on the acquired data. Despite these issues, the algorithms are shown to perform in an accurate manner at steady-state.

This material has been removed from this thesis due to Third Party Copyright. The unabridged version of the thesis can be viewed at the Lanchester Library, Coventry University.

Figure 7.4: Steady-state performance of perturb and observe and ESC algorithms for 100 °C, 150 °C, and 200 °C temperature difference
(Maganga et al. 2014)

7.2.5 TEG emulation: fast transients analysis

The transient performance of the two MPPT algorithms is investigated using a PSU in series with a fixed value (6.8Ω) power resistor to emulate the behaviour of the TEG. The experimental set-up using the PSU is illustrated in Fig. 7.1. This experiment demonstrates the ability of the P&O and the PESC to converge to the MPP after fast changes in the open-circuit voltage. The PSU voltage is

programmed to increase from 12V to 18V in 3V steps within 1 second. Figures 7.5 and 7.6 illustrate the results for P&O and PESC, respectively.

This material has been removed from this thesis due to Third Party Copyright. The unabridged version of the thesis can be viewed at the Lanchester Library, Coventry University.

Figure 7.5: Converter's operating input voltage during PSU open-circuit voltage transients (12V, 15V, 18V) with the perturb and observe controller. Expected theoretical input voltage would be: 6V, 7.5V, 9V. Time *div.* = 100ms; voltage *div.* = 1V
(Maganga et al. 2014)

It is evident that for each PSU voltage both controllers converge to a value very close to the MPP. Whilst P&O provides a smaller limit cycle oscillation around the MPP, the PESC acquires the MPP faster, in around 50ms, compared to 200ms for the P&O. Also, it can be observed in Fig.7.5 and Fig.7.6, that the steady-state characteristics of the TEG system is stable as stated in Assumption 2. Whilst transient performance is assessed via experiment, due to the limitations of the switching frequency f_s in the MicroAutoBox, comparison of convergence between P&O and PESC is not conclusive. As aforementioned, in order to converge faster to the MPP, high values of β and k should be selected. This may however introduce ripples to the input voltage. The ripples are more significant when switching at a lower frequency. To avoid this problem, lower values of β

and k were chosen, as a consequence, poorer convergence but good steady state performance was observed.

This material has been removed from this thesis due to Third Party Copyright. The unabridged version of the thesis can be viewed at the Lanchester Library, Coventry University.

Figure 7.6: Converter's operating input voltage during PSU open-circuit voltage transients (12V, 15V, 18V) with the ESC. Expected theoretical input voltage would be: 6V, 7.5V, 9V. Time *div.* = 100ms; voltage *div.* = 1V

(Maganga et al. 2014)

7.2.6 Transient analysis with actual TEG

The last two tests aimed to compare the operating points chosen by the MPPT algorithms to the maximum estimated TEG power during a long temperature gradient transient across the TEGs. In Fig. 7.7 the converter is running the P&O algorithm. The TEGs are rapidly heated from $\Delta T = 100^\circ\text{C}$ to $\Delta T = 200^\circ\text{C}$ in 420s. In Fig. 7.8 the converter is running the PESC algorithm and the TEG electrical connection is unchanged. The TEGs are cooled from $\Delta T = 200^\circ\text{C}$ to $\Delta T = 100^\circ\text{C}$ in 410 seconds. As aforementioned, the estimated TEG power provided by the mathematical fitting technique has a worse-case accuracy of 5% and

this uncertainty range has been marked in the plots, denoted by P_{max} and P_{min} . In both figures, the average temperature difference across both TEG modules is also plotted for reference as "Temp Diff AVG". Some points related to the power extracted by the P&O and the PESC fall outside the $P_{max} - P_{min}$ boundary. The reason for this is that the two multimeter units used to measure voltage and current were not synchronized, therefore the V-I values taken for each point might not be referenced to the same time instant. The transient response time of the MPPT algorithms is several orders of magnitude faster than the thermal response time of the system; therefore this experiment effectively corresponds to setting numerous steady-state thermal operating points. The results presented show that both algorithms track the maximum available power with efficiency close to 100%.

This material has been removed from this thesis due to Third Party Copyright. The unabridged version of the thesis can be viewed at the Lanchester Library, Coventry University.

Figure 7.7: Thermal transient test of the TEGs from $\Delta T = 100^\circ\text{C}$ to $\Delta T = 200^\circ\text{C}$, connected to the converter with the perturb and observe MPPT algorithm. Tracking with accuracy around 5% the transient maximum estimated TEG.

(Maganga et al. 2014)

Figure 7.8: Thermal transient test of the TEGs from $\Delta T = 200^\circ\text{C}$ to $\Delta T = 100^\circ\text{C}$, connected to the converter with the ESC MPPT algorithm. Tracking with accuracy around 5% the transient maximum estimated TEG.

(Maganga et al. 2014)

7.2.7 Findings and observations

In this phase of the experiment, multiple problems were observed. For instance, the PESC was unable to excite the system with a smaller perturbation gain. Large perturbations were therefore used to excite the system, which results into large oscillations. Also, the advantage of the PESC over P&O seen in the simulation study was inconclusive. This is thought to be due to the limited switching frequency of the MicroAutoBox hardware used to implement the MPPT algorithms, as well as the difficulty in obtaining the optimal PESC tuning parameters and the effects of electrical noise during the data acquisition. In order to overcome these issues, an additional phase of experiments was conducted. The latter sections describe the experimental set-up and the improved results.

7.3 Experimental set-up: Phase II

7.3.1 TEG test rig and electrical characterisation

A similar set-up as that of Phase I was also adopted in Phase II. Based on the findings presented in Section 7.2.7, however, the MicroAutobox was replaced by dSPACE board ds1104 in order to overcome the limitation of the switching frequency. In this phase, a switching frequency of $50kHz$ was used to drive PWM1 and PWM2 of the synchronous DC-DC converter. Also, four commercial 62mm x 62mm TEMs provided by European Thermodynamics Ltd. (GM250-127-28-12) were used in the experimental tests. Each of these modules is rated at $P = 25W$, $V_{oc} = 5.6V$ for $\Delta T = 220^\circ C$. For more details on characteristics of the GM250-127-28-12 see appendix C.3. From Fig. 7.9, A-denotes the control box, B-denotes the thermocouple, C-denotes the heater block, D-denotes TE modules, E-denotes the outlet channel, F-denotes the inlet channel, G-denotes the top end of the cold plate and H denotes the inner side of cold plate. As shown in Fig. 7.9 the cartridge heater block (10mm x 150mm) rated at 300W (see more details in appendix C.1) was fitted at the bottom end of the rig and the coolant loop was created using 2mm pipes. Water from the chiller was supplied to the test rig via 5-inlet and 5 outlet channels. Fig. 7.10 illustrates the schematic diagram of the coolant loop of the rig used in this phase of the experiments. To improve the thermal conductivity of the TEMs, graphite sheets were placed between both the cold end and the TEMs and the hot end and TEMs. The TEMs were placed in a device designed from a sandwich maker (see Fig. 7.9). Three thermocouples were used for reading cold and hot side temperatures. Two of the thermocouples were fitted at the rear and the front of the heater block, whereas one was fitted at the cold end. The heater block was controlled by the control box (more details are given in appendix C.1). The control box allows the temperature of the heater to be regulated at a certain range depending on the desire of the user. As compared to Phase I, in Phase II

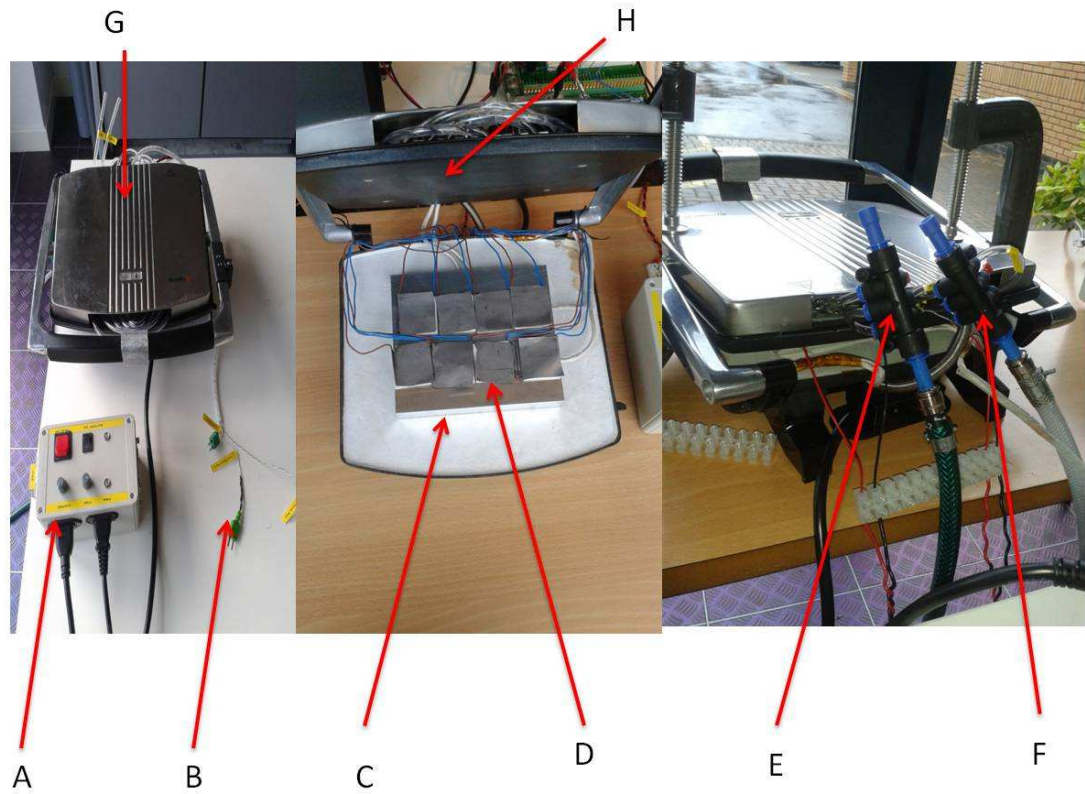


Figure 7.9: Rig provided by ETL used for experiment tests phase II

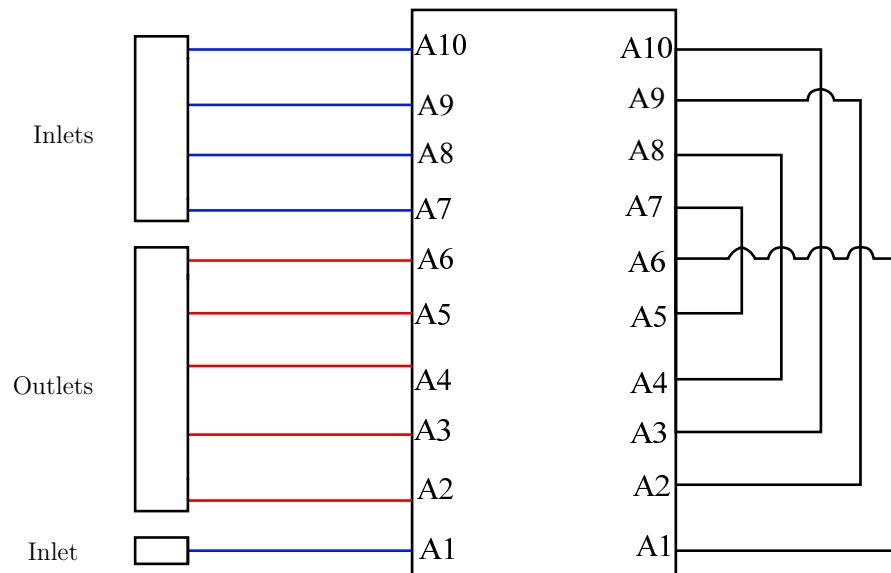


Figure 7.10: Schematic diagram of coolant of the rig used in experiment phase II

all modules were characterised as a group of four TEMs connected electrically in series. Electrical characterisations of the TEMs was performed for 20 different temperature gradients: 50°C to 140°C with increments of 5°C between the hot and cold side of the TEMs. Table. 7.2 presents electrical characterisation of four TEMs connected in series.

Th(°C)	Tc(°C)	$\Delta T(^{\circ}\text{C})$	$V_{oc}(V)$	$V_{mpp}(V)$
202	62	140	5.6	2.8
195	60	135	5.5	2.75
189	59	130	5.4	2.7
183	58	125	5.3	2.65
176	56	120	5.2	2.6
170	55	115	5.18	2.59
164	54	110	5	2.5
158	53	105	4.8	2.4
151	51	100	4.6	2.3
145	50	95	4.47	2.235
138	48	90	4.3	2.15
132	47	85	4.18	2.09
126	46	80	3.9	1.95
120	45	75	3.7	1.85
116	46	70	3.5	1.75
110	45	65	3.3	1.65
105	45	60	3.1	1.55
98	43	55	2.8	1.4
91	41	50	2.5	1.25

Table 7.2: Electrical characterisation of four TEMs electrically connected in series

7.3.2 TEG emulation via power supply unit

The aim of this test is to validate the steady-state performance of the TEG seen in Chapter 6. Also, it aims to demonstrate the ability of the SDP-ESC to track fast transient of the TEG. For these purposes the PESC serves as benchmark. For the steady-state analysis, the PSU was connected in series with a resistor $R_{in} = 3.2\Omega$ and its voltage was maintained at 9.20V which is equivalent to the open circuit voltage.

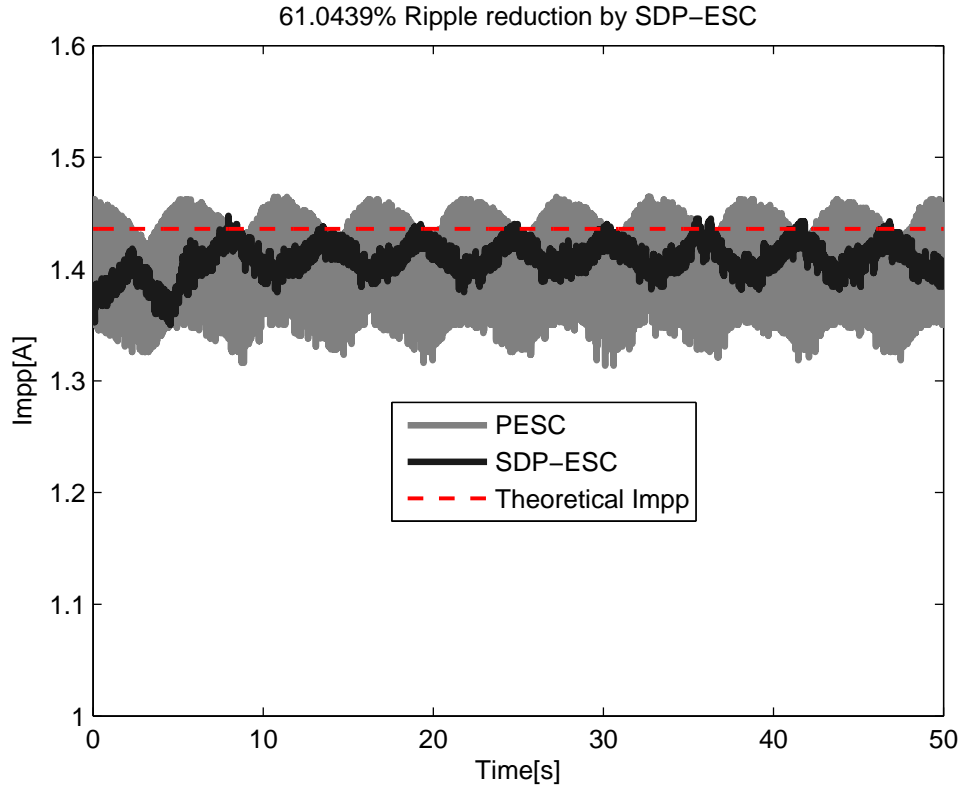


Figure 7.11: Input current at MPP for emulated TEG at steady-state operation

Using (6.6) and (6.7) in Section 6.4, the theoretical power and input voltage at MPP is given as

$$V_{mpp} = \frac{9.2}{2} = 4.6V$$

$$P_{mpp} = \frac{9.2^2}{4 * 3.2} = 6.61W$$

Using values of V_{mpp} and P_{mpp} , the theoretical input current at MPP can be calculated as $I_{mpp} = \frac{6.61}{4.6} = 1.436A$. Fig. 7.11 shows a steady-state comparison of a conventional PESC scheme and an SDP-ESC scheme. At steady-state conventional PESC results in large oscillations. Conversely, the SDP-ESC results in significantly smaller oscillations (61.04% current ripple reduction) for I_{mpp} at steady-state. Similarly, SDP-ESC also achieves smaller oscillation for V_{mpp} (67.97% voltage ripple reduction) at steady-state, see Fig. 7.12. Fig. 7.13 illus-

trates the duty cycle for both the PESC scheme and the SDP-ESC scheme while the emulated TEG is operating at steady-state. Compared to the PESC, the SDP-ESC achieves significantly smaller oscillations.

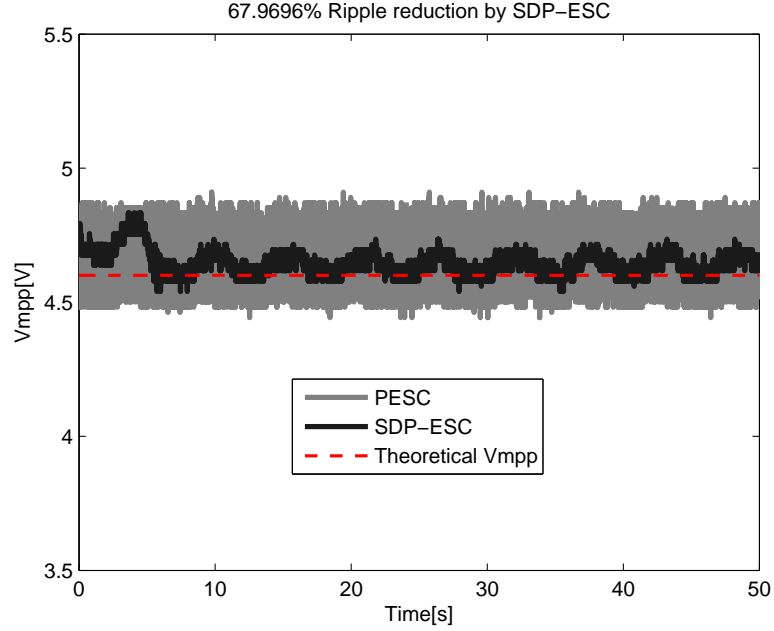


Figure 7.12: Input voltage at MPP with emulated TEG at steady-state operation

Also, the PSU voltage was varied between 10V to 13.0V. Fig. 7.14 shows a comparison of a typical input voltage for a conventional PESC scheme and an SPD-ESC scheme. The upper plot in Fig. 7.14 shows the voltage at the extremum V_{mpp} for the TEG system using conventional PESC and the lower plot shows the voltage at the extremum V_{mpp} for the TEG system using an SDP-ESC. As can be seen in Fig. 7.14, there is significantly less noise for the SDP-ESC than for the PESC. This is due to the oscillations introduced by the PESC system when large initial amplitudes are used. These oscillations hinder the performance of the system and thus the SDP-ESC is clearly an improvement over the conventional PESC method. Fig. 7.16 shows that similar performance is also achieved for the current at the extremum I_{mpp} .

As shown in Figures 7.14 and 7.15, compared to conventional PESC, the SDP-

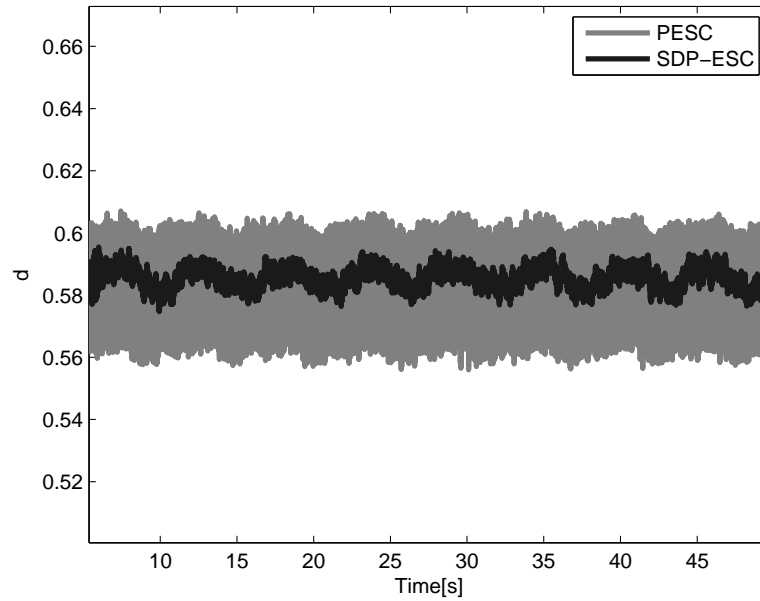


Figure 7.13: Illustrates duty cycle for a standard ESC and SDP-ESC

ESC showing it is capable of keeping the consistency of oscillations minimisation at different voltage levels see. Fig. 7.16 show a comparison of a typical input voltage duty cycle for a conventional PESC and an SDP-ESC. Both the PESC and SDP-ESC suffer from large oscillations in the duty cycle initially. However, the oscillations on the SDP-ESC curve are reduced in a relatively short period of time while the oscillations on the PESC curve remain relatively constant over time.

7.3.3 Transients analysis with real TEG system

In order to perform transient analysis with the actual TEG, four TEMs (GM250-127-28-12) were connected in series and placed between the rig (see Fig. 7.9). However, the rig generates both low open circuit voltage and power (i.e. $V_{oc} = 5.2V, P = 2.5W$ at $\Delta T = 140^\circ C$) which is far lower than expected. This is due to poor heat transfer across the module as well as failure of the cold end of the module to extract enough heat from the TEMs. Since the objective of the Thesis

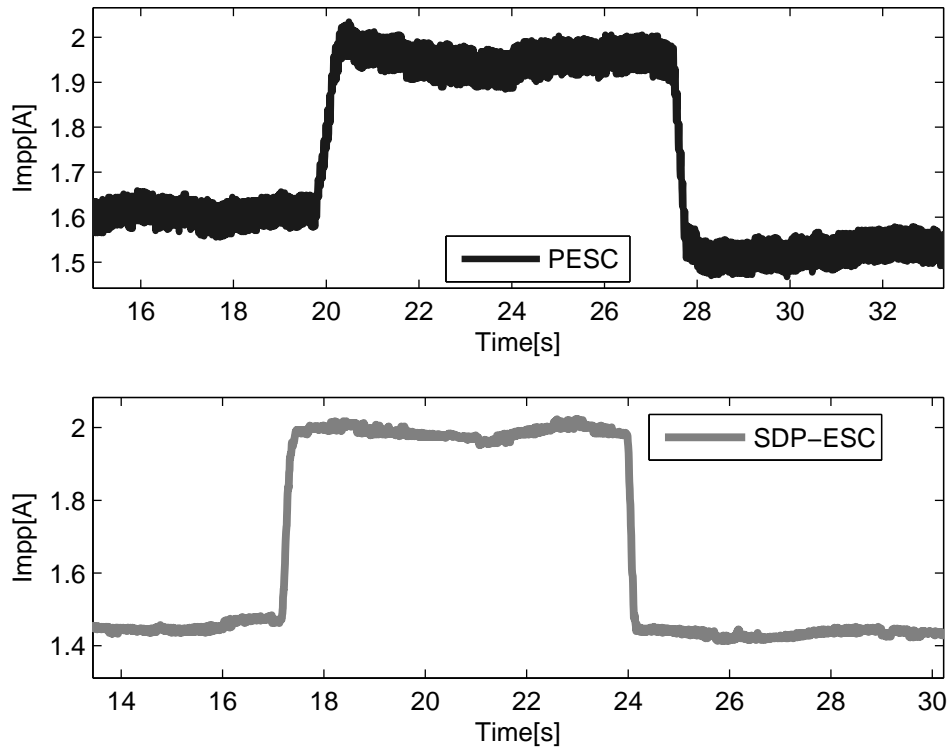


Figure 7.14: Zoomed input current at MPP (I_{mpp}) for variable open circuit voltage

is to maximise power generated by the TEG as well as minimise losses, however, the low power generated by the TEG did not hinder the investigation of the performance of novel algorithms proposed in this Thesis.

Two MPPT controllers namely; PESC and SDP-ESC were tested. The transients performance of the proposed SDP-ESC at a much lower power was tested. The modules were heated up in open loop and once the temperature on hot end reached 200°C and 60°C on cold end then the heater blocks were turned off to allow the modules to cool and one controller at a time was turned on. The significance of such test was to determine performance of the proposed MPPTs during TEG thermal cooling.

Fig. 7.17 illustrates the hot side temperature measurements for the real TEG system with the conventional PESC and the SDP-ESC algorithms. Due to the

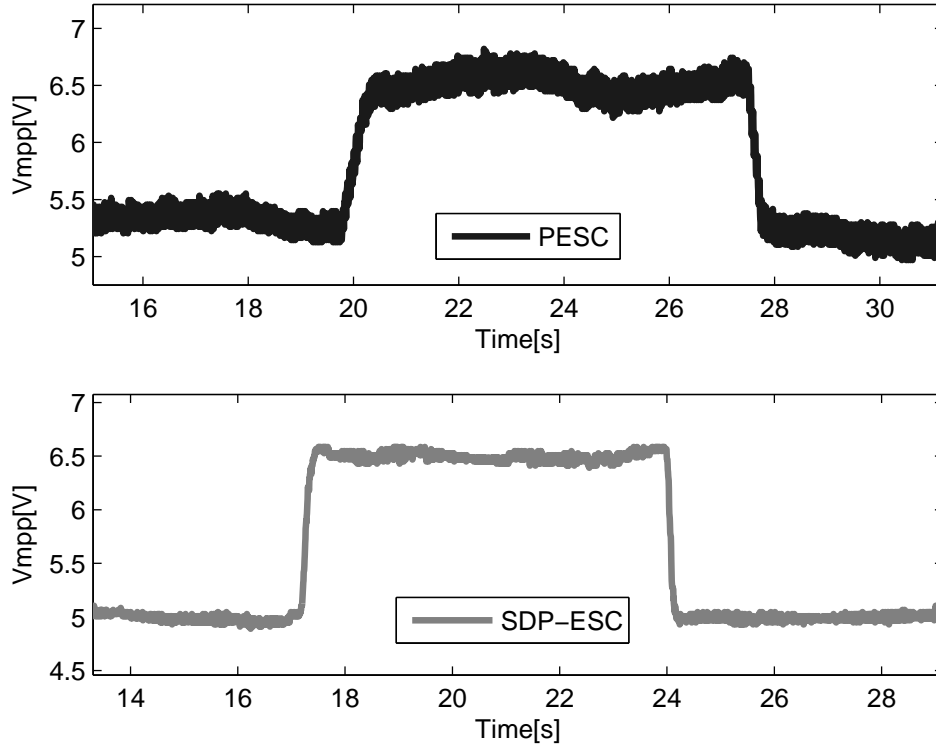


Figure 7.15: Zoomed input voltage at MPP (V_{mpp}) for variable open circuit voltage

ability of the SDP-ESC to minimise losses between the TEG system and the synchronous DC-DC converter, it results in a higher temperature gradient (approximately 5°C over 600 seconds) compared to the conventional PESC.

Fig. 7.18 illustrates the cold side temperature measurements for the TEG system with conventional PESC and the SDP-ESC MPPT algorithms. SDP-ESC achieves a higher temperature gradient (approximately 10°C over 600 seconds). Fig. 7.19 illustrates the temperature difference ΔT measurements for the real TEG system with the conventional PESC and the SDP-ESC. As observed previously, due to the ability of the SDP-ESC to minimise oscillations results in a higher temperature difference ΔT than the conventional PESC. The difference between ΔT 's for the PESC and the SDP-ESC is slightly larger between 200s to 400s. This is due to effect observed at the cold side end temperature.

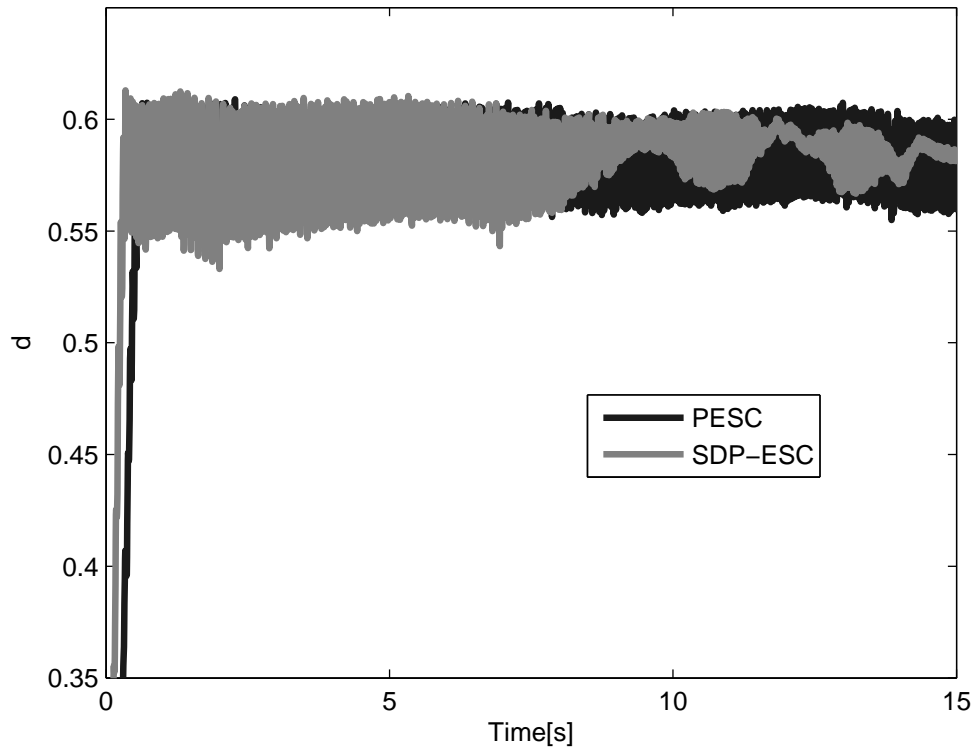


Figure 7.16: Transient response of emulated TEG with PESC and SDP-ESC MPPT algorithms

Table. 7.3 illustrates the tuning parameters of the PESC and the SDP-ESC. Both controllers have been optimised with the same k , ω , ω_l , ω_h and φ . PESC was perturbed with a large β in order to excite the system, which results in large oscillations in both d, I and V . As shown in Fig. 7.20, both the PESC and the SDP-ESC initially suffer from larger oscillations in the duty cycle d_{mpp} at the MPP. However, the oscillations on the SDP-ESC curve are reduced in a relatively short period (approximately 150 seconds) while the oscillations on the PESC curve remain relatively constant over 600 seconds.

Fig. 7.21) shows a comparison of a typical voltage at extremum (V_{mpp}) for the PESC and the SDP-ESC algorithms. As can be seen by comparing transient performance's of the two MPPT's, there is a significantly less oscillations when SDP-ESC is used. These oscillations are introduced by the PESC when a large

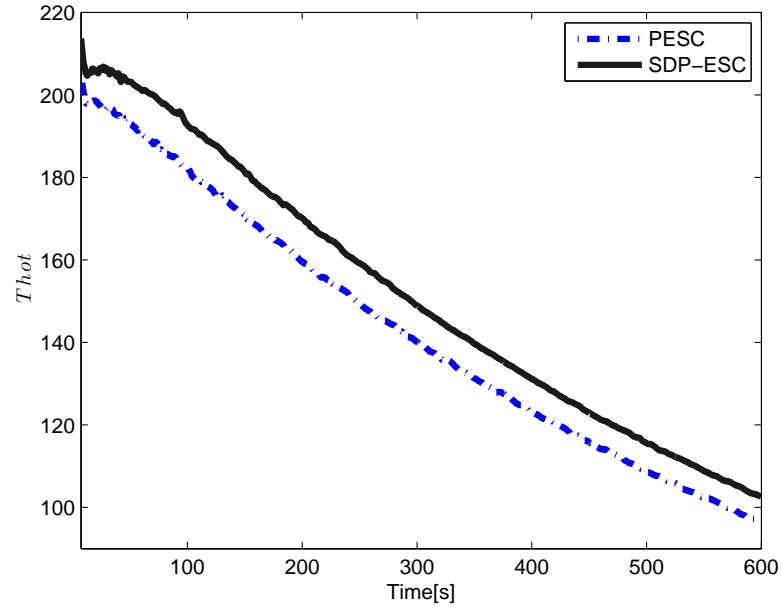


Figure 7.17: Hot side temperature measurements for the real TEG system with PESC and SDP-ESC MPPT algorithms

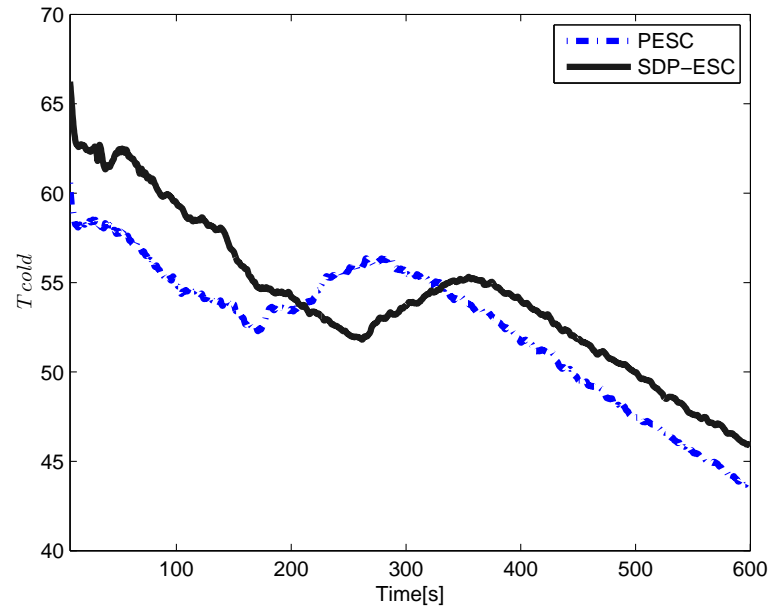


Figure 7.18: Cold side temperature measurements for the real TEG system with PESC and SDP-ESC MPPT algorithms

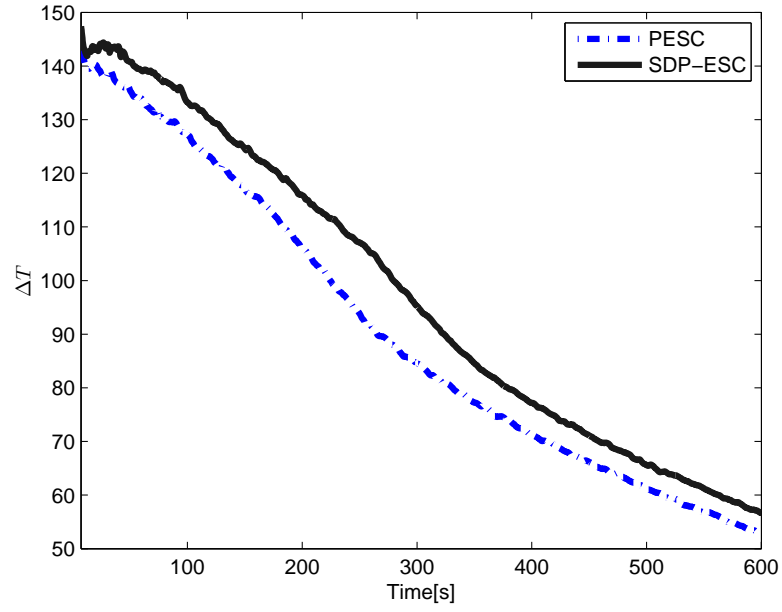


Figure 7.19: Temperature difference (ΔT) measurements for the real TEG system with PESC and SDP-ESC MPPT algorithms

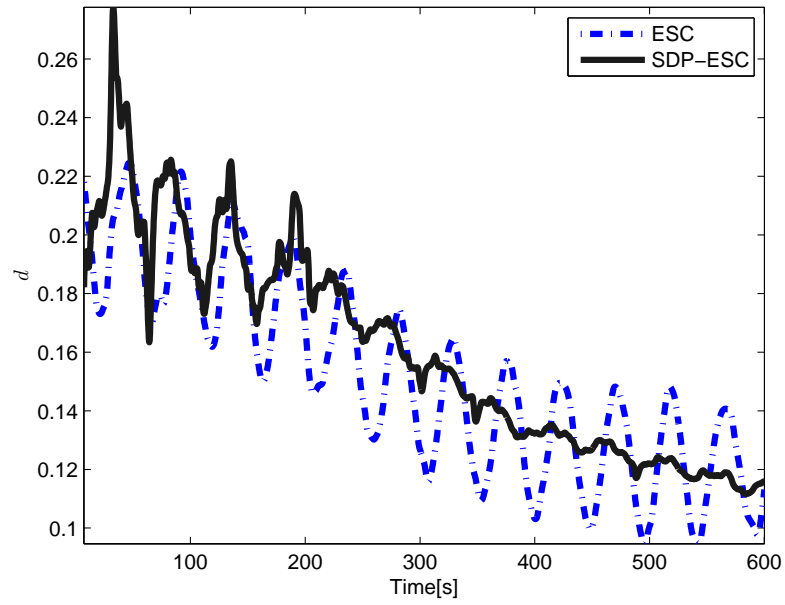


Figure 7.20: Duty cycle measurements for the real TEG system with the use of PESC and SDP-ESC MPPT algorithms

initial amplitudes signal is used to excite the system. These oscillations limit the performance of the system and thus the SDP-ESC is clearly an improvement over the conventional PESC algorithms.

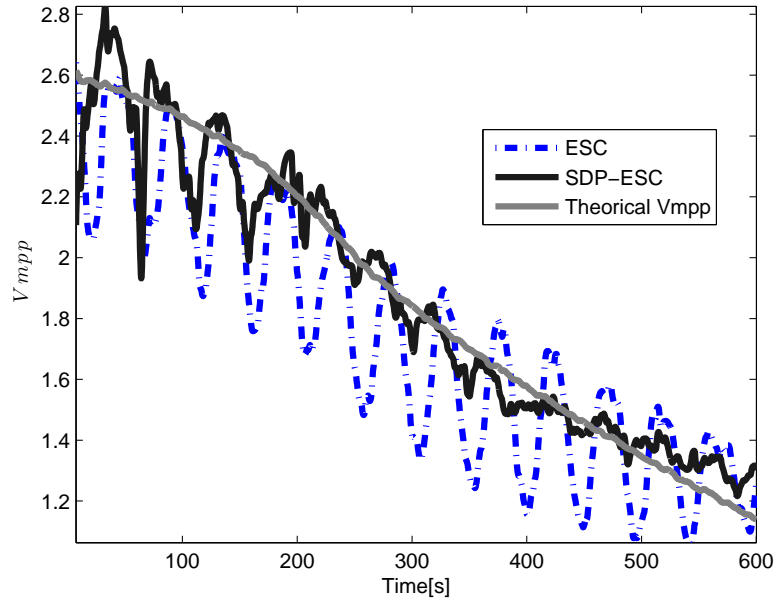


Figure 7.21: Input voltage at MPP (V_{mpp}) for the real TEG system with PESC and SDP-ESC MPPT algorithms

The ability of the SDP-ESC to minimise limit cycle at transients was performed by comparing its performance with that of the PESC algorithm. The test was investigated by first tracking the MPP using the PESC followed by the SDP-ESC. From 0s – 200s, MPP was tracked with the PESC and from 200 seconds to 600 seconds the SDP-ESC was used to track the MPP. As shown in Fig. 7.22 when the PESC was used the oscillations were much higher due to the large initial perturbation required to excite the system. On the other hand, when the SDP-ESC is used the oscillations are significantly reduced (tracking with an accuracy around of 4% of the transient maximum estimated TEG) due to its ability to exponentially decay the perturbation signal.

Parameter	PESC	SDP-ESC
k	1	1
β	0.025	0.1
$\omega \left[\frac{rad}{s} \right]$	25	25
$\omega_h \left[\frac{rad}{s} \right]$	1.5	1.5
$\omega_l \left[\frac{rad}{s} \right]$	1.5	1.5
$\varphi(rad)$	0	0
α	-	$3.5 \cdot 10^{-6}$
C_p	-	5
C_z	-	1

Table 7.3: Tuning parameters for PESC and SDP-ESC used to obtain transient performance for the real TEG system

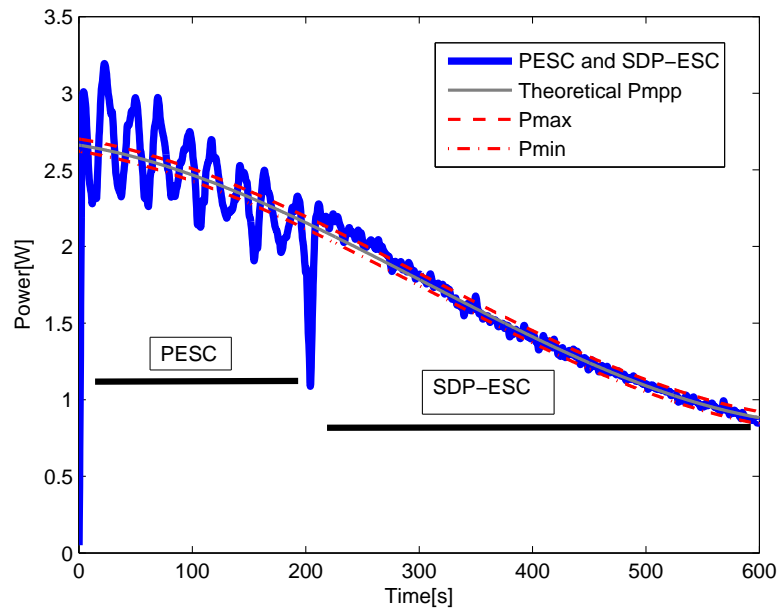


Figure 7.22: Comparison of limit cycle minimisation between PESC and SDP-ESC MPPT algorithms when applied to the real TEG system. SDP-ESC tracking with an accuracy around of 4% of the transient maximum estimated TEG

7.4 Critical appraisal and conclusions

This Chapter presented two phases of experimental work which compared performances of the controllers simulated in Chapter 6. Two different HIL set-ups with the use of MicroAutoBox and ds1104 dSPACE were performed. These set-ups include: TEG emulation via PSU in series with a resistor and real TEG system. Using these two set-ups, three different analyses were performed in both phases which are: steady-state, fast transients using emulated TEG, and actual transients with real TEG. Experiment Phase I presented a comparison of the P&O and the PESC MPPT algorithms. Whilst the results show that the MPPT algorithms accurately track the MPP, the perceived advantage of the PESC seen in simulation was inconclusive. This is thought to be due to the limited switching frequency of the MicroAutoBox hardware used to implement the MPPT algorithms as well as the difficulty in obtaining the optimal PESC tuning parameters and the effects of electrical noise during data acquisition. In Phase II, the MicroAutoBox was replaced by ds1104 in order to increase the switching frequency. One of the issues accounted for in experiment Phase II is that the power generated by the rig was much lower than expected. This is due to poor heat transfer across the TEMs as well as the inability of the coolant loop to extract enough heat from the TEMs. Despite this issue the performance of the proposed MPPT controllers were successfully tested. Compared to the PESC, the SDP-ESC achieved both fast convergence speed as well as smaller oscillations. The VBS-ESC and the LBS-ESC were not experimentally tested as ETL decided to replace the rig with a much better optimised one.

Chapter 8

Conclusions and Further work

8.1 Conclusions and Further work

This Section summarises key achievements of the research work undertaken in this Thesis.

8.1.1 VBS-ESC for local maxima search

In Chapter 3, the scheme for limit cycle minimisation known, as variance based switching extremum seeking control (VBS-ESC) has been proposed. One of the issues addressed in this chapter are limit cycles which are caused by continuous perturbation within a perturbation based extremum seeking control (PESC). VBS-ESC minimises oscillations based on variance detection. VBS-ESC is usually initialised with a large perturbation gain. As the output of the system enters a stable limit cycle, no change in variance will be detected. Once no variance is detected the VBS-ESC will switch to the smaller perturbation gain, hence oscillations will be reduced. As compared to other schemes proposed by Moura & Chang (2010) and Wang & Krstic (2000), the VBS-ESC is simpler and comprises fewer tuning parameters. In terms of limit cycle minimisation both schemes achieve similar output results, hence the proposed method can be viewed as an extension

which provides a simplified scheme for limit cycle minimisation. Including the VBS-ESC, all proposed methods do not take into account the trade-off between convergence speed and minimisation of electrical losses within the power conditioning unit (PCU). To address this issue, an improved PESC scheme known as the state dependent parameter extremum seeking control (SDP-ESC) is presented in Chapter 4.

8.1.2 SDP-ESC for local maxima search

In Chapter 4 a SDP-ESC based on the extension of PESC is proposed. It is similar to the method known as Lyapunov based switching extremum seeking control (LBS-ESC) proposed by Moura & Chang (2010) which linearises the entire feedback loop, defining a Lyapunov function, and using a switch to control the decay process. The proposed scheme introduces a dependency between the perturbation gain and the estimated input which allows an automated exponential decay of the perturbation signal. As compared to VBS-ESC as well as methods proposed by Moura & Chang (2010) and Wang & Krstic (2000), the proposed SDP-ESC is not limited only to limit cycle minimisation. It also takes into account the trade-off between the convergence speed and the minimisation of electrical losses within the PCU. For that reason, the convergence speed is improved by introducing a proportional integral (PI) controller within the SDP-ESC loop. The proposed scheme therefore can be initialised with a large perturbation gain, making it possible to achieve excitation of the system at almost all times. Other advantages of the SDP-ESC as compared the aforementioned schemes include: ability to track adaptively (auto) as well as preserve the stability and simplicity of a standard PESC.

Similar to PESC, VBS-ESC, and LBS-ESC, the drawback of the SDP-ESC is its inability to search for the global maximum in the presence of local maxima. This is based on fact that these methods search the extremum point by control-

ling the gradient at zero through the integrator. Once the nearest peak is found they will converge to it. To eliminate this issue, an extension of the SDP-ESC is proposed in Chapter 5.

8.1.3 Extended SDP-ESC for global maximum search

In Chapter 5, a novel scheme for the global maximum (GM) search in the presence of local maxima has been presented. The scheme is based on an extension of the SDP-ESC scheme presented in Chapter 4. A searching window mechanism has been incorporated within the SDP-ESC in order to effectively search for the GM. The searching window is designed such that the control input of the SDP-ESC is initialised at different operating points. Initialisation of the control input is based on designer knowledge and it can be initialised with either data stored in a look-up table or as a ramp signal. In this Thesis, the scanning window has been initialised using a ramp signal where the range of the ramp signal is based on the operational range. Initialising the SDP-ESC at a different operating point will allow the scanning of all available maxima. Once the true GM has been found, the controller will be switched back to the initialisation point which corresponds to the GM. The scheme has been demonstrated using several examples comprising multiple maxima. Some of the examples presented by Tan et al. (2009) and Azar, Perrier & Srinivasan (2011) were used to demonstrate the ability of the proposed scheme to search the GM. The proposed scheme was shown to be effective in converging to the GM regardless of available number of maxima. Some of the advantages of the proposed scheme are: it preserves the stability and simplicity of the SDP-ESC, it converges faster to the GM, it can be applied for both the GM and local maxima search and it is model-free. The convergence period depends on the operational range of the system as well as the step size of the searching window. When a large step size is selected, faster convergence speed to the GM will be achieved. When a very large step is selected however, the extended SDP-

ESC may barely converge to the true GM. On the other hand, a smaller step will usually guarantee convergence to the true GM. This may however result in a slow convergence speed to the GM.

8.1.4 Modelling, simulation and experimental validation: TEG

In Chapters 6 and 7, the simulation studies and experimental work of novel maximum power point tracking (MPPT) algorithms has been presented. First, a simulation study of perturb and observe (P&O) and PESC was applied to the thermoelectric generator (TEG) as part of the research work undertaken in this Thesis. The simulation results showed that the PESC converged much faster to the maximum power point (MPP) with a 5% reduction of electrical losses. Following this achievement, the experimental work was carried out. Three different analyses were performed which are: steady-state, fast transient with emulated TEG, and transient with the actual TEG. Whilst the results show that the MPPT algorithms accurately track the MPP, the perceived advantage of the PESC seen in simulation was inconclusive. This is thought to be due to the limited switching frequency of the MicroAutoBox hardware used to implement the MPPT algorithms, as well as the difficulty in obtaining the optimal PESC tuning parameters and the effects of electrical noise during the data acquisition. The dSPACE MicroAutoBox hardware however, does allow the user to investigate the hardware implementation of the MPPTs. These limitations led to the development of novel algorithms (i.e. VBS-ESC and SDP-ESC) which incorporated adaptability of the parameters to ensure optimal performance in both transient and steady-state operations. In addition, the dSPACE MicroAutobox was replaced with ds1104 dSPACE which allowed the switches of a synchronous direct current (DC)-DC converter to be driven at a much higher switching frequency.

Performance of the VBS-ESC and the SDP-ESC were compared with the PESC and the LBS-ESC in simulation study Phase II. To validate these findings, experimental test Phase II was conducted. Similar types of tests conducted in Phase I were repeated in Phase II. SDP-ESC achieved both fast convergence speed to the MPP as well as reduced oscillations compared to the PESC when an emulated TEG was used.

Actual transient analysis was performed using the rig provided by European Thermodynamics (ETL), however, the rig was unable to generate the required power as expected. This is due to poor heat transfer across the modules as well as the inability of the coolant loop to extract heat from the thermoelectric modules (TEMs). Since the objective is investigating the performance of the algorithms therefore, this limitation was considered as minor and did not hinder the experiment. However, in order to give sufficient excitation, both the PESC and the SDP-ESC were perturbed with large perturbation gains. As compared to the PESC, the SDP-ESC achieved relatively smaller oscillations due to its ability to exponentially decay the perturbation gain. Due to the low power generated by the rig, rather than characterising each TEM individually, the electrical characterisations of all TEMs connected in series was performed. Open circuit measurements at different temperatures were taken. As aforementioned, for the TEG, the maximum available power is achieved when the input voltage is half of the open circuit voltage. Smaller limit cycles indicate less degradation to the components. Other MPPT controllers (i.e. VBS-ESC and LBS-ESC) were not tested experimentally.

8.2 Further work

This Section, proposes some directions which could be taken for further improvements.

8.2.1 Constrained VBS-ESC/SDP-ESC scheme

Both the VBS-ESC and the SDP-ESC are model-free which assumes no *a priori* knowledge of the plant or system (neither model nor cost function is available). Based on these assumptions, there are no constraints imposed to the system. These controllers seemed to give optimal performance when applied to the TEG system. Experiments carried out in this Thesis however were conducted under well-controlled environmental conditions. On the other hand, when applied to systems where uncertainties are significant, the proposed MPPT controllers may result in less optimal performance than that seen in the laboratory. To address these concerns it may be useful to further investigate the possibilities and advantages of imposing constraints particularly for systems where prior knowledge exists.

8.2.2 Experimental validation global maximum searching scheme

Simulation studies showed that the extended SDP-ESC scheme proposed in this Thesis is able to search for the GM regardless of the number of maxima. As compared to stochastic based approaches for the GM, this is considered to be inexpensive solution as it is model-free. It will therefore be beneficial to validate these findings experimentally as well as imposing constraints to the extended SDP-ESC if needed. One possible example which can be used to validate these findings is PV systems due to shading effects which causes multiple maxima to occur.

8.2.3 Embedding VBS-ESC/SDP-ESC for stand-alone operation

Experimental work carried out through hardware in the loop (HIL) testing demonstrates the ability of the SDP-ESC to minimise limit cycle as well as converging faster to the MPP compared to the standard PESC. It will therefore be useful to implement the SDP-ESC for stand-alone operations. The SDP-ESC algorithm can be embedded into a microcontroller, further integrated within a TEG and tested in a complete drive cycle. This will validate the robustness of the SDP-ESC particularly under harsh driving conditions and other uncertainties (e.g. noise, disturbances, etc.).

8.2.4 Degradation of PCU components

Limit cycles are associated with the degradation of components (e.g. electrolyte capacitors) within a PCU. Large ripples may increase the equivalent series resistance as well as decrease the capacitance of the capacitor. It will be beneficial to investigate the performance of the novel MPPT algorithms as the components degrade. One possible way to achieve this is by incorporating degradation effects within the DC-DC converter. Based on performance of the MPPT algorithm, necessary improvements can be performed.

References

- Ariyur, K. & Krstic, M. (2010), *Real-Time Optimization by Extremum-Seeking Control*.
- Ariyur, K. & Krystic, M. (2003), *Real-Time Optimization by Extremum-Seeking Control*, John Wiley & Sons.
- Azar, F., Perrier, M. & Srinivasan, B. (2011), ‘A global optimization method based on multi-unit extremum-seeking for scalar nonlinear systems’, *Computers and Chemical Engineering* **35**.
- Bizon, N. (2010), ‘On tracking robustness in adaptive extremum seeking control of the fuel cell power plants’, *Applied energy* **87**, 3115–3130.
- Bizon, N. (2013), ‘Fc energy harvesting using the mpp tracking based on advanced extremum seeking control’, *International Journal of Hydrogen Energy* **38**(4), 1952–1966.
- Calli, B., Caarls, W., Jonker, P. & Wisse, M. (2012a), ‘Comparison of extremum seeking control algorithms for robotic applications’, *International Conference on Intelligent Robots and Systems* **39**, 3195–3202.
- Calli, B., Caarls, W., Jonker, P. & Wisse, M. (2012b), Comparison of extremum seeking control algorithms for robotic applications, *in* ‘Intelligent Robots and Systems (IROS), 2012 IEEE/RSJ International Conference on’, pp. 3195–3202.

- Champier, D., Favarel, C., Bdcarrats, J., Kousksou, T. & Rozis, J. (2013), ‘Prototype combined heater/thermoelectric power generator for remote applications’, *Journal of Electronic Materials* **42**(7), 1888–1899.
- Chang, Y. & Moura, S. (2009), Air flow control in fuel cell systems: An extremum seeking approach, *in* ‘American Control Conference, 2009. ACC ’09.’, pp. 1052–1059.
- Chen, Y., Chou, M. & Wu, H. (2005), Electrolytic capacitor failure prediction of lc filter for switching-mode power converters, *in* ‘Fortieth IAS Annual Meeting’.
- Cho, S., Kim, N., Park, S. & Kim, S. (2010), A coreless maximum power point tracking circuit of thermoelectric generators for battery charging systems, *in* ‘Solid State Circuits Conference (A-SSCC), 2010 IEEE Asian’, pp. 1–4.
- Cistelecan, M. (2008), Power control in mobile wireless networks using sliding mode extremum seeking control implementing bifurcations, *in* ‘Control Applications, 2008. CCA 2008. IEEE International Conference on’, pp. 67–72.
- Crane, D. & Jackson, G. (2002), Systems-level optimization of low-temperature thermoelectric waste heat recovery, *in* ‘Energy Conversion Engineering Conference, 2002. IECEC ’02. 2002 37th Intersociety’, pp. 583–591.
- Dan, Z., Bo, H., Jian, X., Yi, G. & Yuan, R. (2008), ‘Adaptive maximum power point tracking control of fuel cell power plants’, *Journal of Power Sources* **176**(1), 259–269.
- Daraban, S., Petreus, D. & Morel, C. (2014), ‘A novel mppt(maximum power point tracking) algorithm based on a modified genetic algorithm specialized on tracking the global maximum power point in photovoltaic systems affected by partial shading’, *Energy* **74**(0), 374 – 388.

- Dincmen, Erkin., G. B. & Acarman, T. (2012), ‘Extremum-seeking control of abs braking in road vehicles with lateral force improvement’, *IEEE Transactions on Control Systems Technology* **22**, 230–237.
- Dochain, D., Perrier, M. & Guay, M. (2011), ‘Extremum seeking control and its application to process and reaction systems: A survey’, *Mathematics and Computers in Simulation* **82**(3), 369–380.
- Doostabad, H., Keypour, R. & Khalghani, M. (2013), ‘A new approach in mppt for photovoltaic array based on extremum seeking control under uniform and non-uniform irradiances’, *Solar Energy* **94**.
- Drakunov, S., Ozguner, U., Dix, P. & Ashrafi, B. (1995), ‘Abs control using optimum search via sliding modes’, *Control Systems Technology, IEEE Transactions on* **3**(1), 79–85.
- Draper, C. & Li, Y. (1951), ‘Principles of optimizing control systems and an application to the internal combustion engine’.
- D’Souza, N., Lopes, L. & Liu, X. (2005), An intelligent maximum power point tracker using peak current control, *in* ‘Power Electronics Specialists Conference, 2005. PESC ’05. IEEE 36th’.
- Eakburanawat, J. & Boonyaroonate, I. (2006), ‘Development of a thermoelectric battery-charger with microcontroller-based maximum power point tracking technique’, *Applied Energy* **83**(7), 687–704.
- Elobaid, L., Abdelsalam, A. & Zakzouk, E. (2012), Artificial neural network based maximum power point tracking technique for pv systems, *in* ‘IECON 2012 - 38th Annual Conference on IEEE Industrial Electronics Society’, pp. 937–942.

- Esarte, J., Min, G. & Rowe, D. (2001), ‘Modelling heat exchangers for thermoelectric generators’, *Journal of Power Sources* **93**(12), 72 – 76.
- Esrām, T. & Chapman, P. (2007), ‘Comparison of photovoltaic array maximum power point tracking techniques’, *Energy Conversion, IEEE Transactions on* **22**(2), 439–449.
- Gelberta, G., Moeck, J., Paschereit, C. & King, R. (2012), ‘Advanced algorithms for gradient estimation in one-and two parameter extremum seeking controllers’, *Journal of Process Control* **22**, 700–709.
- Guay, M. (2014), ‘A time-varying extremum-seeking control approach for discrete-time systems’, *Journal of Process Control* **24**, 98–112.
- Guay, M., Dochain, D. & Perrier, M. (2004), ‘Adaptive extremum seeking control of continuous stirred tank bioreactors with unknown growth kinetics’, *Automatica* **40**(5), 881–888.
- Guay, M. & Zhang, T. (2003), ‘Adaptive extremum seeking control of nonlinear dynamic systems with parametric uncertainties’, *Automatica* **39**, 1283–1293.
- Gurvich, L. (2004), Fuzzy logic base extremum seeking control system, in ‘Electrical and Electronics Engineers in Israel, 2004. Proceedings. 2004 23rd IEEE Convention of’, pp. 18–21.
- Haskara, I., Zhu, G. & Winkelman, J. (2006), Multivariable egr/spark timing control for ic engines via extremum seeking, in ‘American Control Conference, 2006’.
- Henning, L., Becker, R., Feuerbach, G., Muminovic, R., King, R., Brunn, A. & Nitsche, W. (2008), ‘Extensions of adaptive slope-seeking for active flow control’, *Journal of Systems and Control Engineering* **222**, 309–322.

- Hiyama, T., Kouzuma, S. & Imakubo, T. (1995), ‘Identification of optimal operating point of pv modules using neural network for real time maximum power tracking control’, *Energy Conversion, IEEE Transactions on* **10**(2), 360–367.
- Hu, Y. & Zuo, B. (2005), ‘An annealing recurrent neural network for extremum seeking control’, *International Journal of Information Technology* **11**.
- Hu, Y., Zuo, B. & Li, X. (2006), The application of an annealing recurrent neural network for extremum seeking algorithm to optimize uav tight formation flight, in ‘Computational Engineering in Systems Applications, IMACS Multiconference on’, Vol. 1, pp. 613–620.
- Hussain, Q. E., Brigham, D. R. & Maranville, C. W. (2009), Thermoelectric exhaust heat recovery for hybrid vehicles, Technical report, SAE Technical Paper.
- Irisawa, K., Saito, T., Takano, I. & Sawada, Y. (2000), Maximum power point tracking control of photovoltaic generation system under non-uniform insolation by means of monitoring cells, in ‘Photovoltaic Specialists Conference, 2000. Conference Record of the Twenty-Eighth IEEE’, pp. 1707–1710.
- Jain, S. & Agarwal, V. (2004), ‘A new algorithm for rapid tracking of approximate maximum power point in photovoltaic systems’, *Power Electronics Letters, IEEE* **2**(1), 16–19.
- Kamarzaman, N. & Tan, C. (2014), ‘A comprehensive review of maximum power point tracking algorithms for photovoltaic systems’, *Renewable and Sustainable Energy Reviews* **37**, 585 – 598.
- Khong, S., Nesic, D., Manzie, C. & Tan, Y. (2013), ‘Multidimensional global extremum seeking via the direct optimisation algorithm’, *Automatica* **49**.

- Killingsworth, N. & Krstic, M. (2006), ‘Pid tunings using extremum seeking: on-line, model-free performance optimization’, *IEEE Control Systems Magazine* **26**, 70–79.
- Kim, K., Kasnakoglu, C., Serrani, A. & Samimy, M. (2008), Extremum-seeking control of subsonic cavity flow, *in* ‘Proceedings of the 46th AIAA aerospace science meeting and exhibit’.
- Kim, K., Kasnakoglu, C., Serrani, A. & Samimy, M. (2009), ‘Extremum-seeking control of subsonic cavity flow’, *AIAA* **47**, 195–205.
- Kim, R. & Lai, J. (2008), ‘A seamless mode transfer maximum power point tracking controller for thermoelectric generator applications’, *Power Electronics, IEEE Transactions on* **23**(5), 2310–2318.
- Kim, S., Cho, S., Kim, N., Baatar, N. & Kwon, J. (2011), ‘A digital coreless maximum power point tracking circuit for thermoelectric generators’, *Journal of Electronic Materials* **40**(5), 867–872.
- King, R., Petz, R. & Lemke, O. (2006), ‘Adaptive flow control using slope seeking’, *Mediterranean Conference on Control and Automation* **14**.
- Kobayashi, K., Takano & Sawada, Y. (2006), ‘A study of a two stage maximum power point tracking control of a photovoltaic system under partially shaded insolation conditions’, *Solar Energy Materials and Solar Cells* **90**(1819), 2975 – 2988. 14th International Photovoltaic Science and Engineering Conference 14th International Photovoltaic Science and Engineering Conference.
- Koizumi, H. & Kurokawa, K. (2005), A novel maximum power point tracking method for pv module integrated converter, *in* ‘Power Electronics Specialists Conference, 2005. PESC ’05. IEEE 36th’, pp. 2081–2086.

- Korovin, S. & Utkin, V. (1972), ‘Use of the slide mode in problems of static optimization’, *Automatic and Remote Control* .
- Korovin, S. & Utkin, V. (1974), ‘Using sliding modes in static optimization and nonlinear programming’, *Automatica* **10**.
- Krstic, M. (2000), ‘Performance improvement and limitations in extremum seeking control’, *Systems and Control Letters* **39**, 313–326.
- Krstic, M. & Bastin, G. (1999), ‘Optimizing bioreactors by extremum seeking’, *International Journal of Adaptive Control and Signal Processing* **13**, 651–669.
- Laird, I., Lovatt, H., Savvides, N., Lu, D. & Agelidis, V. (2008), Comparative study of maximum power point tracking algorithms for thermoelectric generators, in ‘Power Engineering Conference, 2008. AUPEC ’08. Australasian Universities’, pp. 1–6.
- Laird, I. & Lu, D. (2013), ‘High step-up dc/dc topology and mppt algorithm for use with a thermoelectric generator’, *Power Electronics, IEEE Transactions on* **28**(7), 3147–3157.
- Leblanc, M. (1922), ‘Sur l’electrification des chemins de fer au moyen de courants alternatifs de frquence leve’, *Revue Generale delElectricit* .
- Lee, J., Bae, H. & Cho, B. (2006), Advanced incremental conductance mppt algorithm with a variable step size, in ‘Power Electronics and Motion Control Conference, 2006. EPE-PEMC 2006. 12th International’, pp. 603–607.
- Lei, P. & Li, Y. (2010), ‘Extremum seeking control based integration of mppt and degradation detection for photovoltaic arrays’, *American Control Conference* pp. 3536–3541.

- Li, X., Li, Y., Seem, J. & Li, P. (2013), ‘Dynamic modeling and self-optimizing operation of chilled water systems using extremum seeking control’, *Energy and Buildings* **58**, 172–182.
- Lineykin, S. & Ben-Yaakov, S. (2007), ‘Modeling and analysis of thermoelectric modules’, *Industry Applications, IEEE Transactions on* **43**(2), 505–512.
- Liu, B., Duan, S., Liu, F. & Xu, P. (2007), Analysis and improvement of maximum power point tracking algorithm based on incremental conductance method for photovoltaic array, in ‘Power Electronics and Drive Systems, 2007. PEDS ’07. 7th International Conference on’, pp. 637–641.
- Liu, S. & Krstic, M. (2012), *Stochastic Averaging and Stochastic Extremum Seeking*.
- Maganga, O., Larkowski, T. & Burnham, K. (2012), Model complexity reduction of a dc-dc buck-boost converter, in ‘22nd International Conference on Systems Engineering (ICSE)’.
- Maganga, O., Phillip, N., Burnham, K. J., Montecucco, A., Siviter, J., Knox, A. & Simpson, K. (2014), ‘Hardware implementation of maximum power point tracking for thermoelectric generators’, *Journal of Electronic Materials* **43**(6), 2293–2300.
- Manzie, C. & Kristic, M. (2009a), Extremum-seeking control via sliding mode with periodic search signals, in ‘IEEE Conference on Decision and Control’, Vol. 41.
- Manzie, C. & Kristic, M. (2009b), ‘Extremum seeking with stochastic perturbations’, *IEEE Transactions on Automatic Control* **54**.

- Messai, A., Mellit, A., Guessoum, A. & Kalogirou, S. (2011), ‘Maximum power point tracking using a ga optimized fuzzy logic controller and its fpga implementation’, *Solar Energy* **85**(2), 265 – 277.
- Montecucco, A., Buckle, J. & Knox, A. (2012), ‘Solution to the 1-d unsteady heat conduction equation with internal joule heat generation for thermoelectric devices’, *Applied Thermal Engineering* **35**(0), 177 – 184.
- Montecucco, A. & Knox, A. (2014), ‘Maximum power point tracking converter based on the open-circuit voltage method for thermoelectric generators’, *IEEE Transactions on Power Electronics* .
- Montecucco, A., Siviter, J. & Knox, A. (2012), Simple, fast and accurate maximum power point tracking converter for thermoelectric generators, *in* ‘Energy Conversion Congress and Exposition (ECCE), 2012 IEEE’, pp. 2777–2783.
- Moradi, M. & Reisi, A. (2011), ‘A hybrid maximum power point tracking method for photovoltaic systems’, *Solar Energy* **85**(11), 2965–2976.
- Moradi, M., Tousi, S., Nemati, M., Basir, N. & Shalavi, N. (2013), ‘A robust hybrid method for maximum power point tracking in photovoltaic systems’, *Solar Energy* **94**(0), 266–276.
- Moura, S. & Chang, Y. (2010), Asymptotic convergence through lyapunov-based switching in extremum seeking with application to photovoltaic systems, *in* ‘American Control Conference (ACC), 2010’, pp. 3542–3548.
- Moura, S. & Chang, Y. (2013), ‘Lyapunov-based switched extremum seeking for photovoltaic power maximization’, *Control Engineering Practice* **21**(7), 971–980.

- Nagayoshi, H. & Kajikawa, T. (2006), Mismatch power loss reduction on thermoelectric generator systems using maximum power point trackers, *in* 'Thermoelectrics, 2006. ICT '06. 25th International Conference on', pp. 210–213.
- Nagayoshi, H., Kajikawa, T. & Sugiyama, T. (2002), Comparison of maximum power point control methods for thermoelectric power generator, *in* 'Thermoelectrics, 2002. Proceedings ICT '02. Twenty-First International Conference on', pp. 450–453.
- Nagayoshi, H., Tokumisu, K. & Kajikawa, T. (2007), Evaluation of multi mppt thermoelectric generator system, *in* 'Thermoelectrics, 2007. ICT 2007. 26th International Conference on', pp. 318–321.
- Nesic, D., Mohammadi, A. & Manzie, C. (2013), 'Framework for extremum seeking control of systems with parameter uncertainties', *IEEE Transactions on Automatic Control* **58**, 435–448.
- Ogren, P., Fiorelli, E. & Leonard, N. (2004), 'Cooperative control of mobile sensor networks:adaptive gradient climbing in a distributed environment', *Automatic Control, IEEE Transactions on* **49**(8), 1292–1302.
- Park, J., Lee, H. & Bond, M. (2014), 'Uninterrupted thermoelectric energy harvesting using temperature-sensor-based maximum power point tracking system', *Energy Conversion and Management* **86**, 233–240.
- Patcharaprakiti, N., Premrudeepreechacharn, S. & Sriuthaisiriwong, Y. (2005), 'Maximum power point tracking using adaptive fuzzy logic control for grid-connected photovoltaic system', *Renewable Energy* **30**(11), 1771 – 1788.
- Phillip, N., Maganga, O., Burnham, K., Dunn, J., Rouaud, C., Ellis, M. & Robinson, S. (2012), Modelling and simulation of a thermoelectric generator for waste heat energy recovery in low carbon vehicles, *in* '2nd International

- Symposium on Environment Friendly Energies and Applications (EFEA), 2012', pp. 94–99.
- Phillip, N., Maganga, O., Burnham, K. J., Ellis, M. A., Robinson, S., Dunn, J. & Rouaud, C. (2013), 'Investigation of maximum power point tracking for thermoelectric generators', *Journal of electronic materials* **42**(7), 1900–1906.
- Popovic, D., Jankovic, M., Magner, S. & Teel, A. (2006), 'Extremum seeking methods for optimization of variable cam timing engine operation', *Control Systems Technology, IEEE Transactions on* **14**(3), 398–407.
- Ramaprabha, R. & Mathur, B. (2011), 'Intelligent controller based maximum power point tracking for solar pv system', *International Journal of Computer Applications* **12**(10), 37 – 41.
- Reisi, A., Moradi, M. & Jamasb, S. (2013), 'Classification and comparison of maximum power point tracking techniques for photovoltaic system: A review', *Renewable and Sustainable Energy Reviews* **19**, 433 – 443.
- Rowe, D. (2005), *Thermoelectrics Handbooks*.
- Schwartz, D. (2012), A maximum-power-point-tracking control system for thermoelectric generators, in 'Power Electronics for Distributed Generation Systems (PEDG), 2012 3rd IEEE International Symposium on', pp. 78–81.
- Shadmand, M., Balog, R. & Abu Rub, H. (2014), Maximum power point tracking using model predictive control of a flyback converter for photovoltaic applications, in 'Power and Energy Conference at Illinois (PECI), 2014', pp. 1–5.
- Snyder, G. J. & Toberer, E. S. (2008), 'Complex thermoelectric materials', *Nature materials* **7**(2), 105–114.
- Stobart, R. & Milner, D. (2009), The potential for thermo-electric regeneration of energy in vehicles, Technical report, SAE Technical Paper.

- Tan, Y., Moase, W., Manzie, C., Nesic, D. & Mareels, I. (2010), Extremum seeking control from 1922 to 2010, *in* ‘Proceeding of the 29th Chinese Control Conference’, pp. 14–26.
- Tan, Y., Nei, D. & Mareels, I. (2008), ‘On the choice of dither in extremum seeking systems: A case study’, *Automatica* **44**(5), 1446–1450.
- Tan, Y., Nesic, D., Mareels, I. & Astolfi, A. (2009), ‘On global extremum seeking in the presence of local extrema’, *Automatica* **45**, 245–251.
- Tanelli, M., Astolfi, A. & Savaresi, S. (2006), Non-local extremum seeking control for active braking control systems, *in* ‘International Conference on Control Applications’, pp. 891–896.
- Vieira, J. & Mota, A. (2009), Thermoelectric generator using water gas heater energy for battery charging, *in* ‘Control Applications, (CCA) Intelligent Control, (ISIC), 2009 IEEE’, pp. 1477–1482.
- Wai, R., Wang, W. & Lin, J. (2006), Grid-connected photovoltaic generation system with adaptive step-perturbation method and active sun tracking scheme, *in* ‘IEEE Industrial Electronics, IECON 2006 - 32nd Annual Conference on’, pp. 224–228.
- Wang, H. & Krstic, M. (2000), ‘Extremum seeking for limit cycle minimisation’, *IEEE Transactions on Automatic Control* **45**.
- Wiederhold, O., King, R., Noack, B., Neuhaus, L., Neise, W., Enghardt, L. & Swoboda, M. (2009), ‘Extensions of extremum-seeking control to improve the aerodynamic performance of axial turbomachines’, *AIAA Fluid Dynamics Conference* **39**, 22–25.

- Xiao, W. & Dunford, W. (2004), A modified adaptive hill climbing mppt method for photovoltaic power systems, *in* ‘Power Electronics Specialists Conference, 2004. PESC 04. 2004 IEEE 35th Annual’, Vol. 3, pp. 1957–1963 Vol.3.
- Yang, S., Xiang, D., Bryant, A., Mawby, P., Ran, L. & Tavner, P. (2010), ‘Condition monitoring for device reliability in power electronic converters: A review’, *Power Electronics, IEEE Transactions on* **25**(11), 2734–2752.
- Youn, N., Lee, H., Wee, D., Gomez, M., Reid, R. & Ohara, B. (2014), ‘Achieving maximum power in thermoelectric generation with simple power electronics’, *Journal of Electronic Materials* **43**(6), 1597–1602.
- Yu, S., Chen, H. & Kong, L. (2010), ‘Particle swarm optimization-based extremum seeking control’, *Advanced Intelligent Computing Theories and Applications* **6215**, 185–196.
- Zhang, C. (2007), ‘Numerical optimization-based extremum seeking control with application to abs design’, *IEEE Transactions on Automatic Control* **52**, 454–467.
- Zhang, C. & Ordonez, R. (2012), *Extremum Seeking Control and Applications, A Numerical Optimization-Based Approach*.
- Zhang, C., Siranosian, A. & Kristic, M. (2007), ‘Extremum seeking for moderately unstable systems and for autonomous target tracking without position measurements’, *Automatica* **43**, 1832–1839.
- Zhang, C., Siranosian, A. & Kristic, M. (2009), ‘Design of extremum seeking control with pd accelerator and its application to monod and williams-otto models’, *Engineering and Technology* **3**, 1154–1158.

- Zhang, F., Thanapalan, K., Procter, A., Carr, S. & Maddy, J. (2013), ‘Adaptive hybrid maximum power point tracking method for a photovoltaic system’, *Energy Conversion, IEEE Transactions on* **28**(2), 353–360.
- Zhang, T., Guay, M. & Dochain, D. (2002), ‘Adaptive extremum seeking control of continuous stirred tank bioreactors’, *IFAC* (6).

Appendix A

Description of the TEG model

Similar to the physical system, the TEG model is set-up with multiples of the three subsystems with each multiple representing a section of the system in the stream of the exhaust as shown in Fig. A. The TEG model requires the exhaust and coolant inlet temperature (T_{ai} , T_{wi}) and mass flow rate (m_a , m_w) as inputs and outputs of the voltage and current (V , I) generated by the TEG. The transient analysis capability of the model makes it possible to account for the initial warm up period and also provides the capability to integrate with a vehicle model for fuel consumption analysis over defined drive cycles.

A.1 Thermal electric module (TEM)

TEMs can either be connected electrically in series or parallel to increase the operating voltage or decrease the thermal resistance, respectively. The TEM subsystem uses the hot and cold side temperature inputs from the heat exchanger

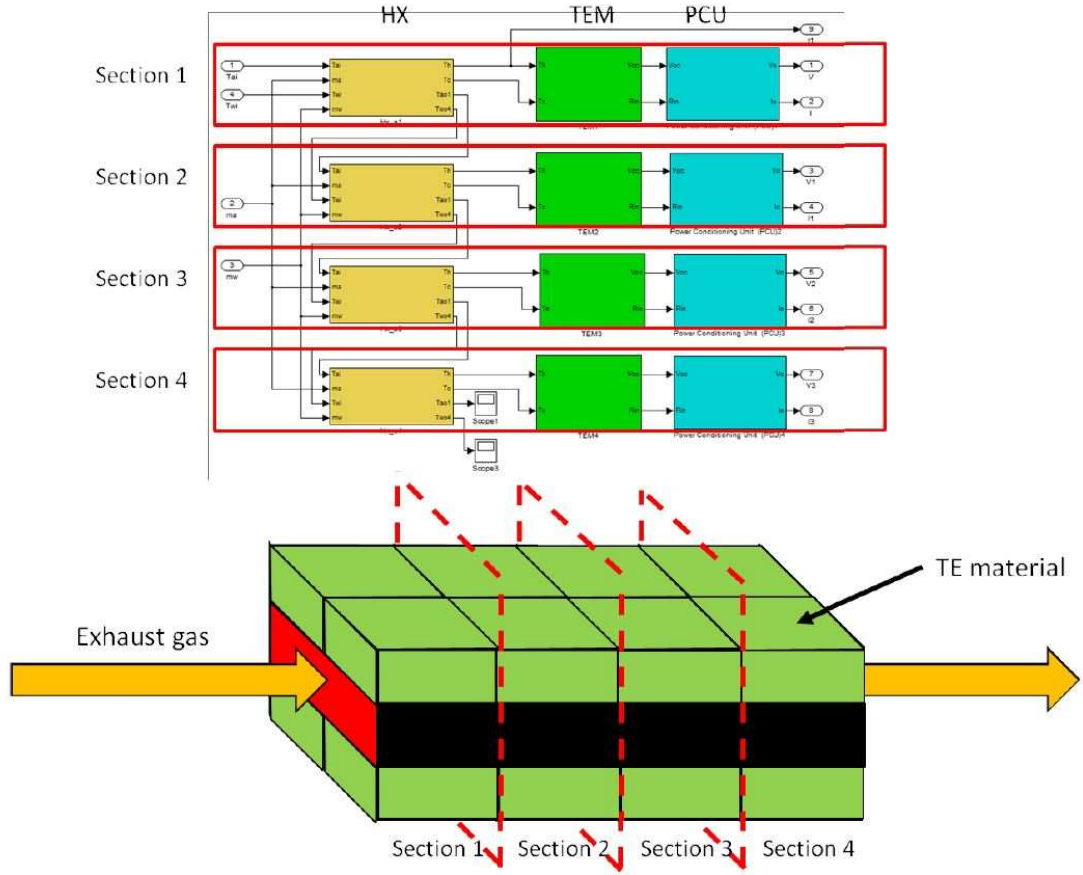


Figure A.1: TEG subsystem configuration in comparison to physical system

subsystem to give the electrical power generated using the following equations

$$V_{oc} = n_{couple} (s_n + s_p) \Delta T \quad (\text{A.1a})$$

$$R_{in} = \frac{n_{couple} (\rho_n + \rho_p) L_{tem}}{A} \quad (\text{A.1b})$$

$$K_m = \frac{n_{couple} (\kappa_n - \kappa_p) L_{tem}}{A} \quad (\text{A.1c})$$

where s_n denotes Seebeck coefficient of n thermal couple, κ_n denotes thermal conductivity of n thermal couple. V_{oc} denotes the open circuit voltage (V), ρ denotes the electrical resistivity $\Omega\text{-m}$, R_{in} denotes the module internal resistance (Ω), K_m denotes the module thermal conductivity (W/Km), A denotes the cross-sectional area (m^2), n_{couple} denotes the number of couples, L_{tem} denotes leg length

(m), subscripts "n" and "p" refer to n -type and p -type legs.

A.2 Heat exchange (HX) subsystem

The HX subsystem in Phillip et al. (2013) is modelled as a stack of several thermal layers (see Fig. A.2). The interactions between individual thermal layers are described using convection and conduction thermodynamic energy balance equations. Convection and conduction thermodynamics energy balance equations were used to describe the interactions between individual thermal layers. The energy balanced equations were formulated based on the assumption that, the temperature distribution within the layers is homogeneous, hence simplifying the overall computation whilst retaining the main dynamic features. A further detailed description of the model together with governing equations can be found in Phillip et al. (2012). The HX is divided into several control volumes along the flow of the exhaust gas stream. Heat flow from the exhaust layer to the coolant layer, i.e., from hot to cold, is assumed to be uniform, a function of the mean temperature of the individual layer, and a function of time. The TEG model does not include the heat losses to adjacent control volumes and heat losses to ambient, given the uncertainty of environmental effects within the system. Considering (A.1a) and (A.1b), it is apparent that the TEM is modelled using material data for n -type and p -type legs of n -couple number of couples. The Bismuth telluride (Bi_2Te_3) TEM was validated in Phillip et al. (2013) in order to provide confidence in the modelling methodology. The validated TEM model (TEM subsystem) achieves an output with 94.6% accuracy at steady state.

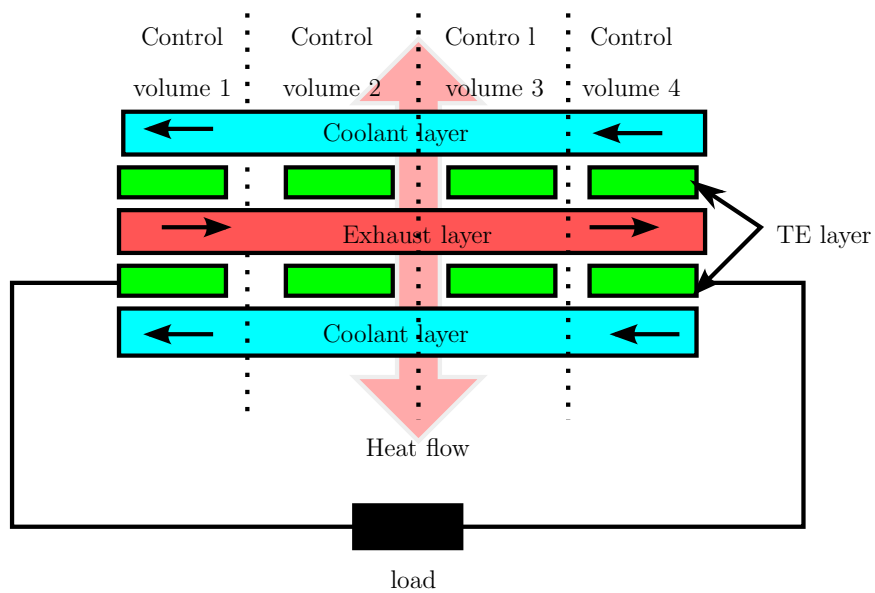


Figure A.2: TEG HX/TEM configuration

Appendix B

Simulink block diagram for MPPT algorithms

B.1 Simulink models of MPPT algorithms

This appendix presents Simulink models of the MPPT algorithms implemented in this Thesis. As shown in Fig. B.1 duty cycle from a selected controller are fed into a DS1104-DSP-PWM3 which generates 6 PWM signals of which 3 are in same phase and 3 are out of phase. Two PWM signals were used to drive the synchronous DC-DC converter. The analog signals from the converter reading were taken from ADC-5 to ADC-8. I_{out} and I_{in} scaled by 1:1 and V_{out} scaled by 1:4 and V_{in} scaled by 1:16. In order to obtain the temperature reading in dSPACE from K-type thermal couples AD-595 were used. The scale of 1:100 was used to rescale these readings.

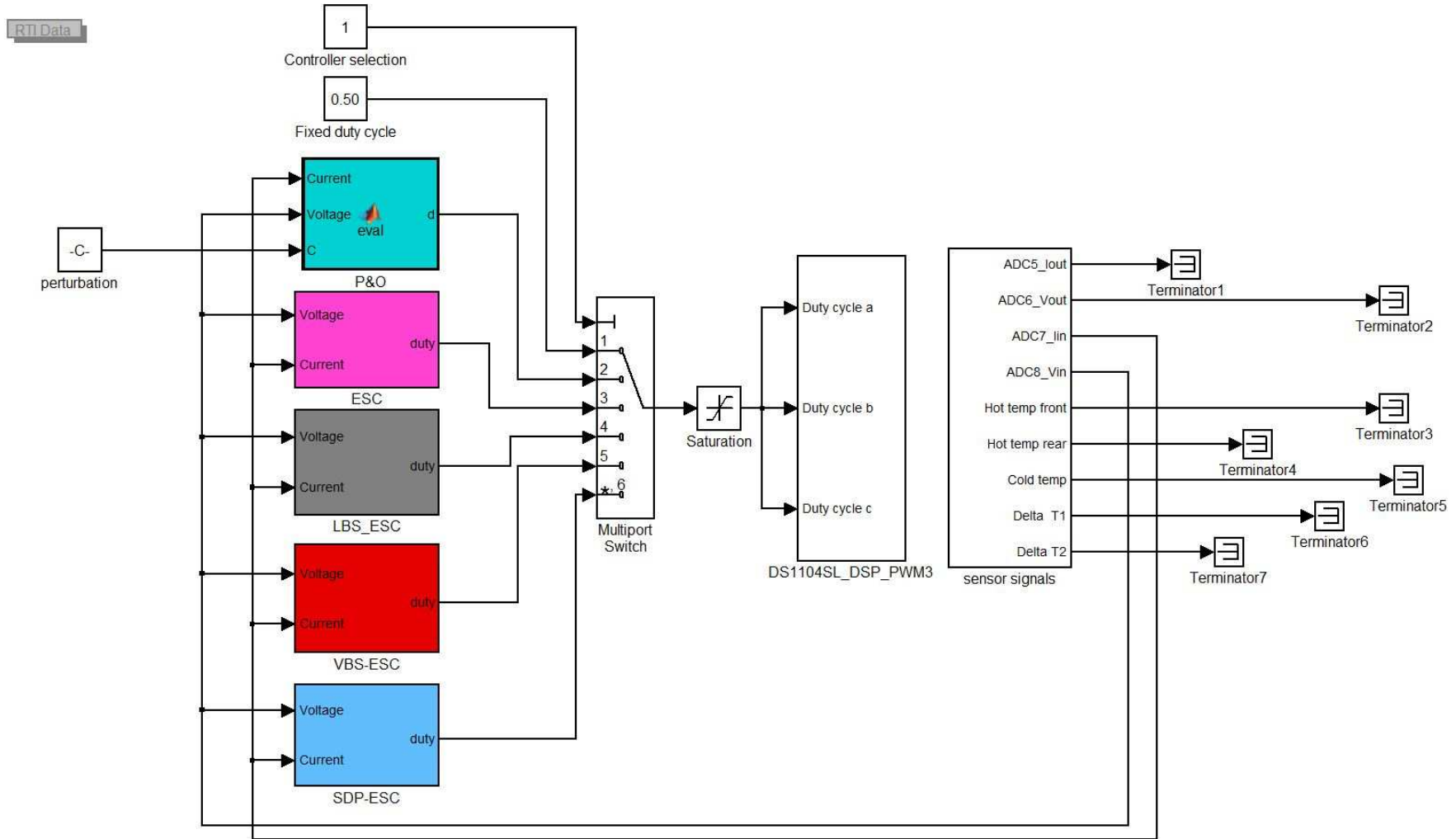


Figure B.1: Simulink block diagram for P&O, PESC, LBS-ESC, VBS-ESC and SDP-ESC subsystems

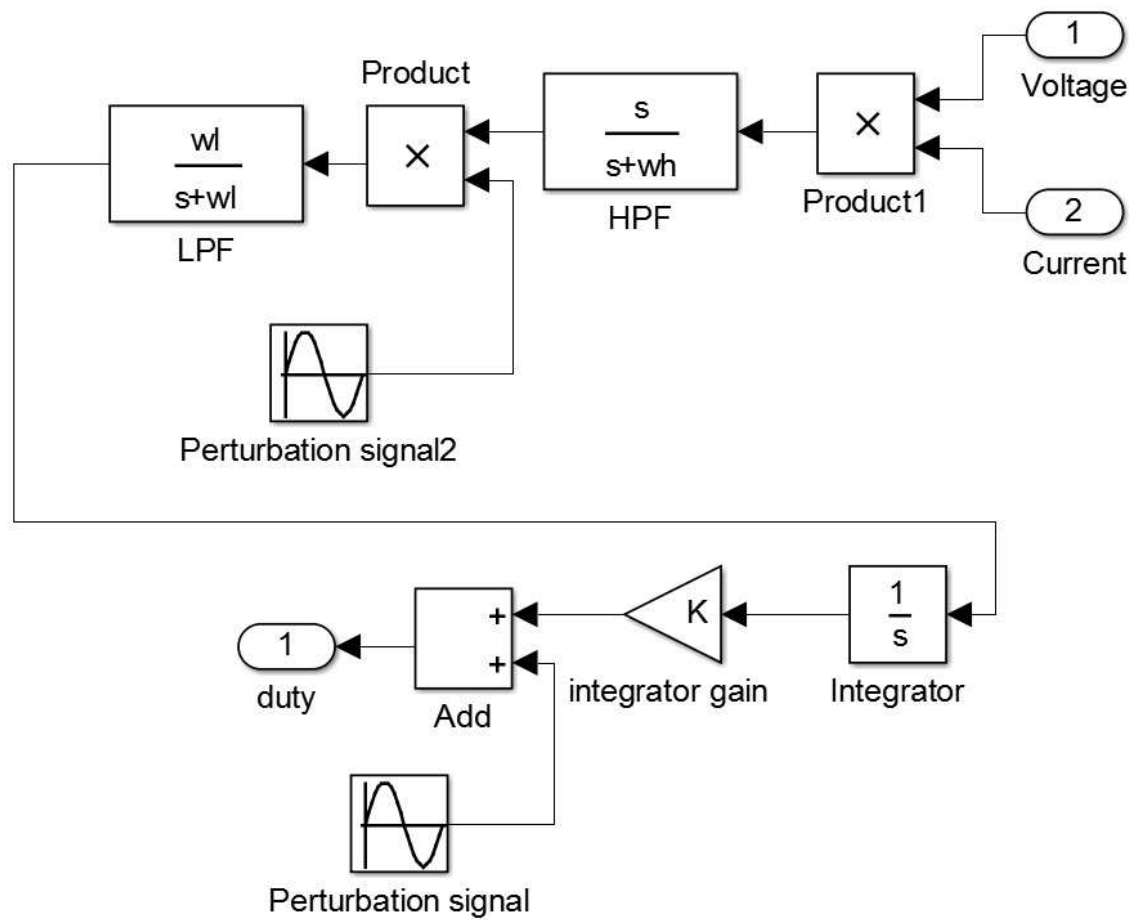


Figure B.2: Simulink block diagram for PESC subsystem

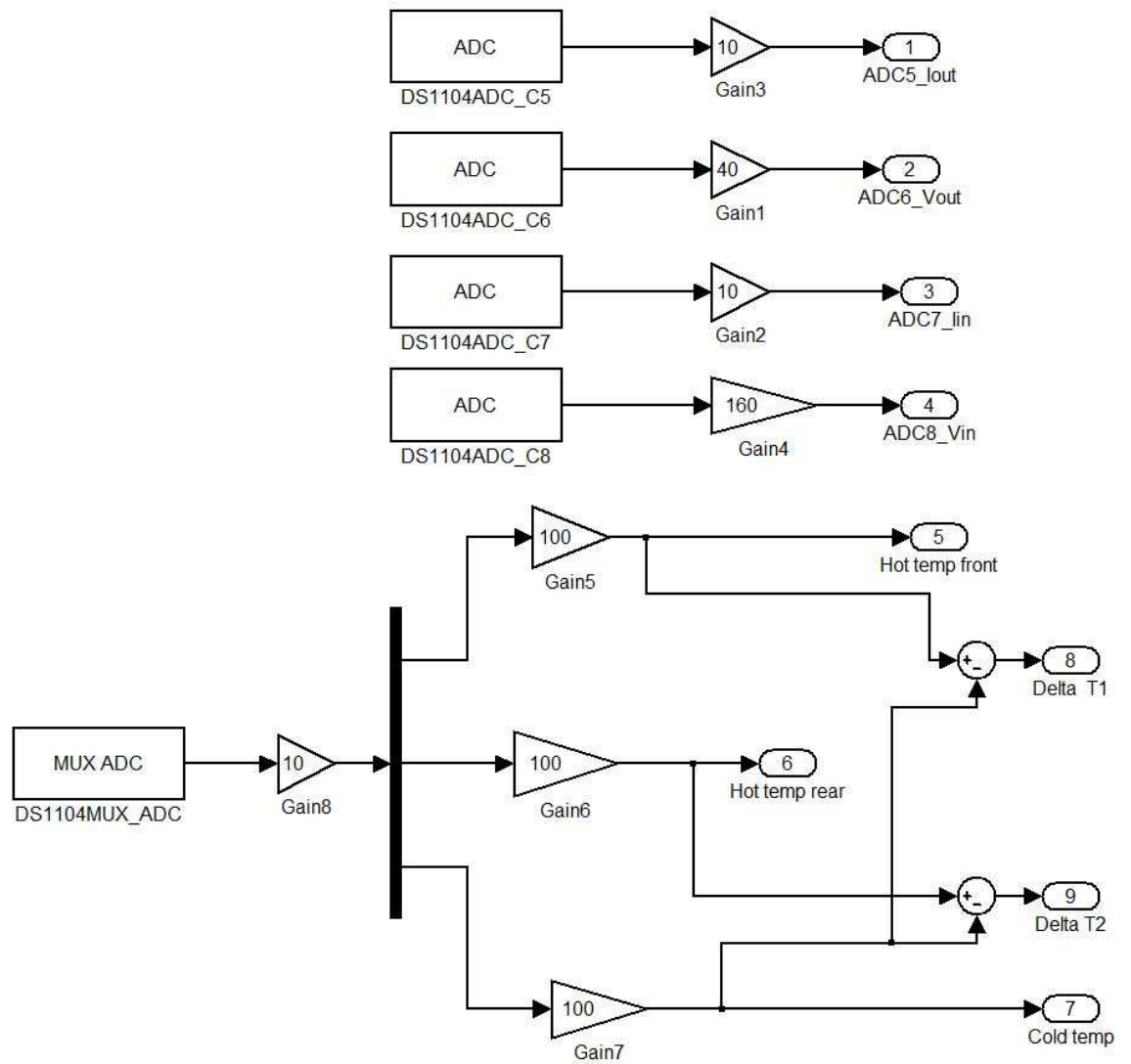


Figure B.3: Simulink block diagram for sensor measurements from ADCs

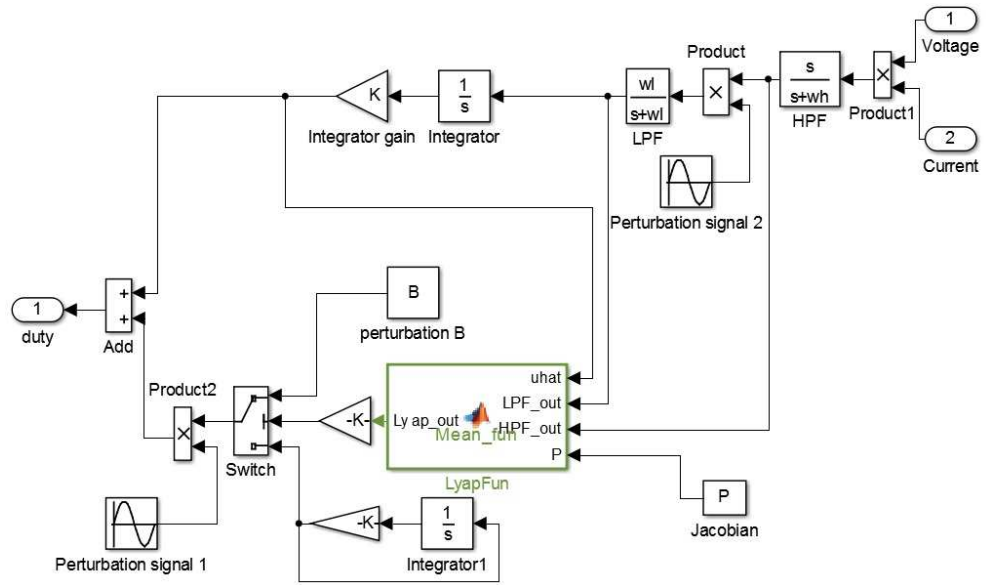


Figure B.4: Simulink block diagram for LBS-ESC subsystem

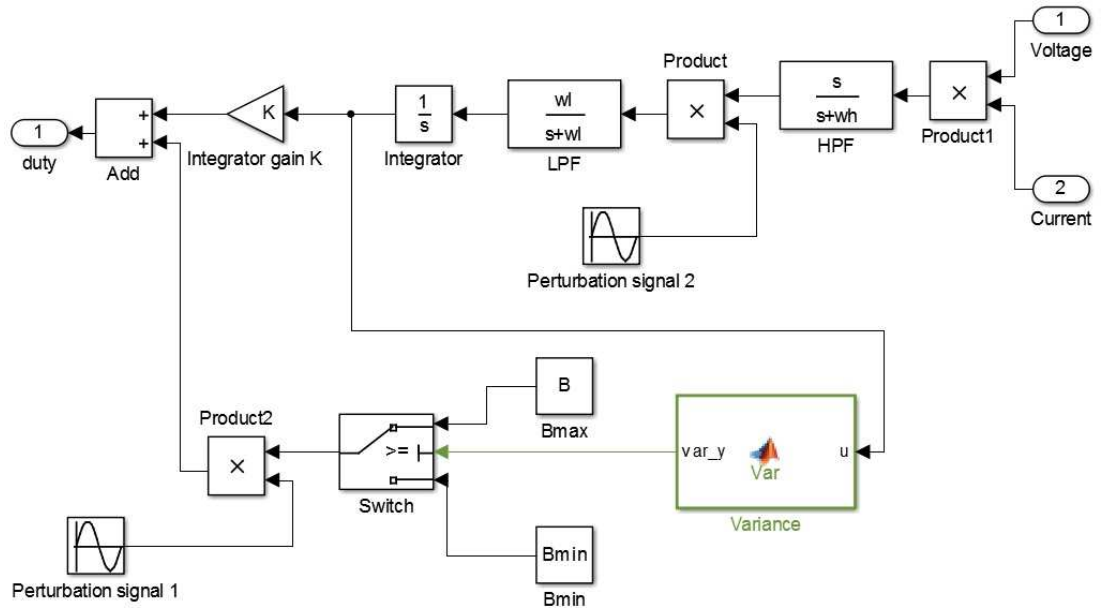


Figure B.5: Simulink block diagram for VBS-ESC subsystem

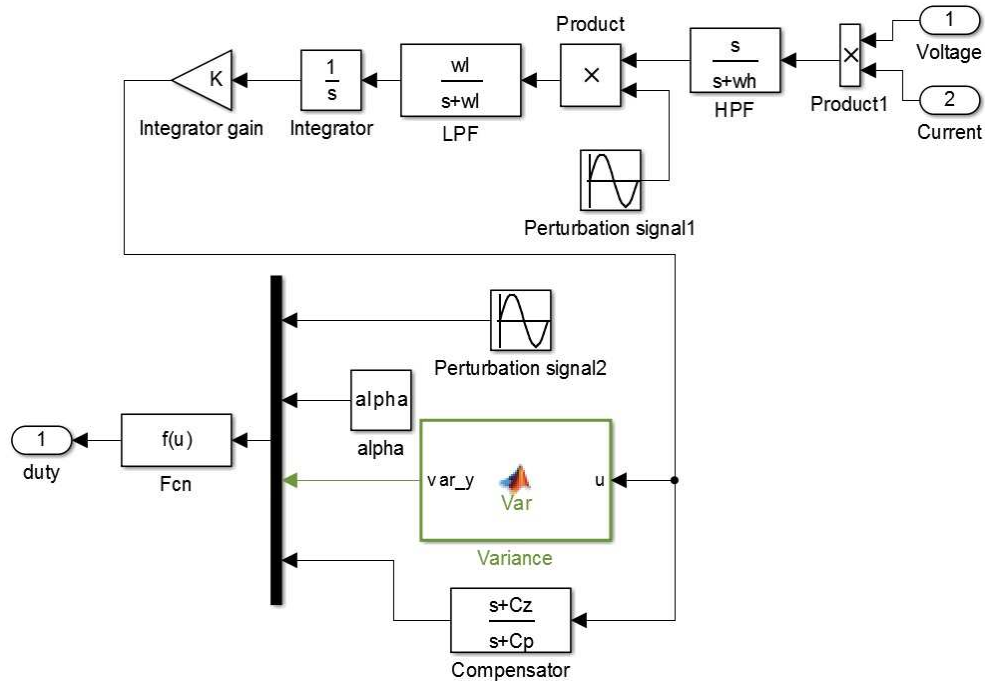


Figure B.6: Simulink block diagram for SDP-ESC subsystem

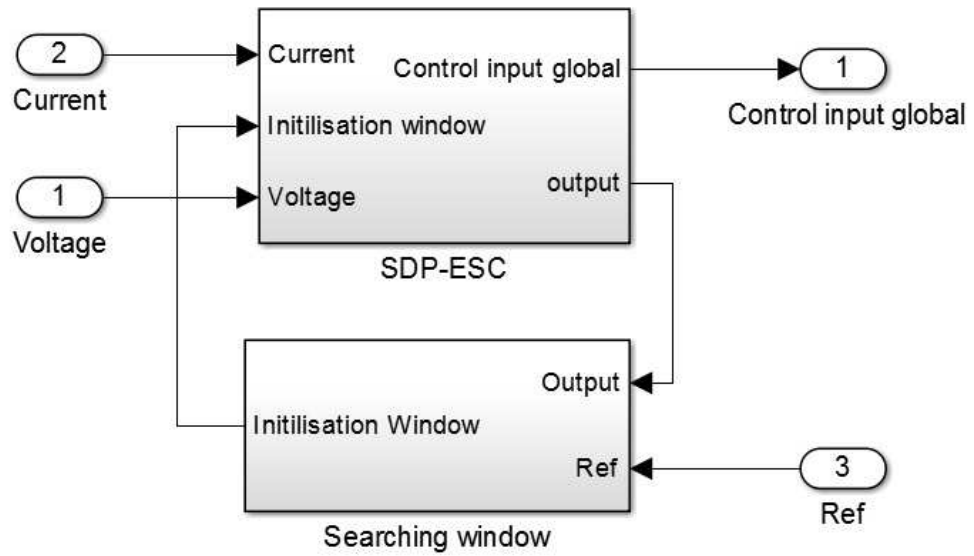


Figure B.7: Simulink block diagram for extended SDP-ESC subsystem

Appendix C

Components/Instruments used in the HIL set-up

This appendix presents instruments and components used in the HIL set-up via dSPACE which are: Temperature control box, cartridge heater, synchronous DC-DC converter and GM250-127-28-12 TE modules. The main information provided in this appendix includes: the schematic diagram of the temperature control box and the synchronous DC-DC converter also, data sheets for the heater cartridge and the TE modules. Both schematics (i.e. the temperature control box and synchronous DC-DC converter) comprises all components and these schematics were used for designing the PCB layout.

Cartridge Heater, 10mmX150mm, 300W



Standard Features and Internal Construction:-



1. High temperature lead wires for temperatures up to 450° C.
2. High impact ceramic cap retards contamination and is suitable for high vibration applications. Deep holes in cap prevent fraying of leads when bent.
3. Nickel-chromium resistance wire for maximum heater life, evenly wound for even heat distribution.
4. High purity magnesium oxide fill selected for maximum dielectric strength and thermal conductivity, highly compacted for maximum heat transfer.
5. 304 stainless steel sheath for oxidation resistance in a wide variety of environments. 316 stainless steel and Incoloy are also available. Please consult the application guide in the back for help in determining which material is best for your application.
6. TIG welded end disc to prevent contamination and moisture absorption.

Technical Specifications:-

- Diameter : 10mm (9.86mm to 9.98mm Tolerance)
- Length : 150 Length
- Voltage : 220V AC
- Wattage : 300W Wattage
- Lead wires : 10 inch long
- Lead wire insulation : Fibreglass

Figure C.2: Specifications for cartridge heater block used in experiment phase II

C.2 Synchronous DC-DC buck-boost converter

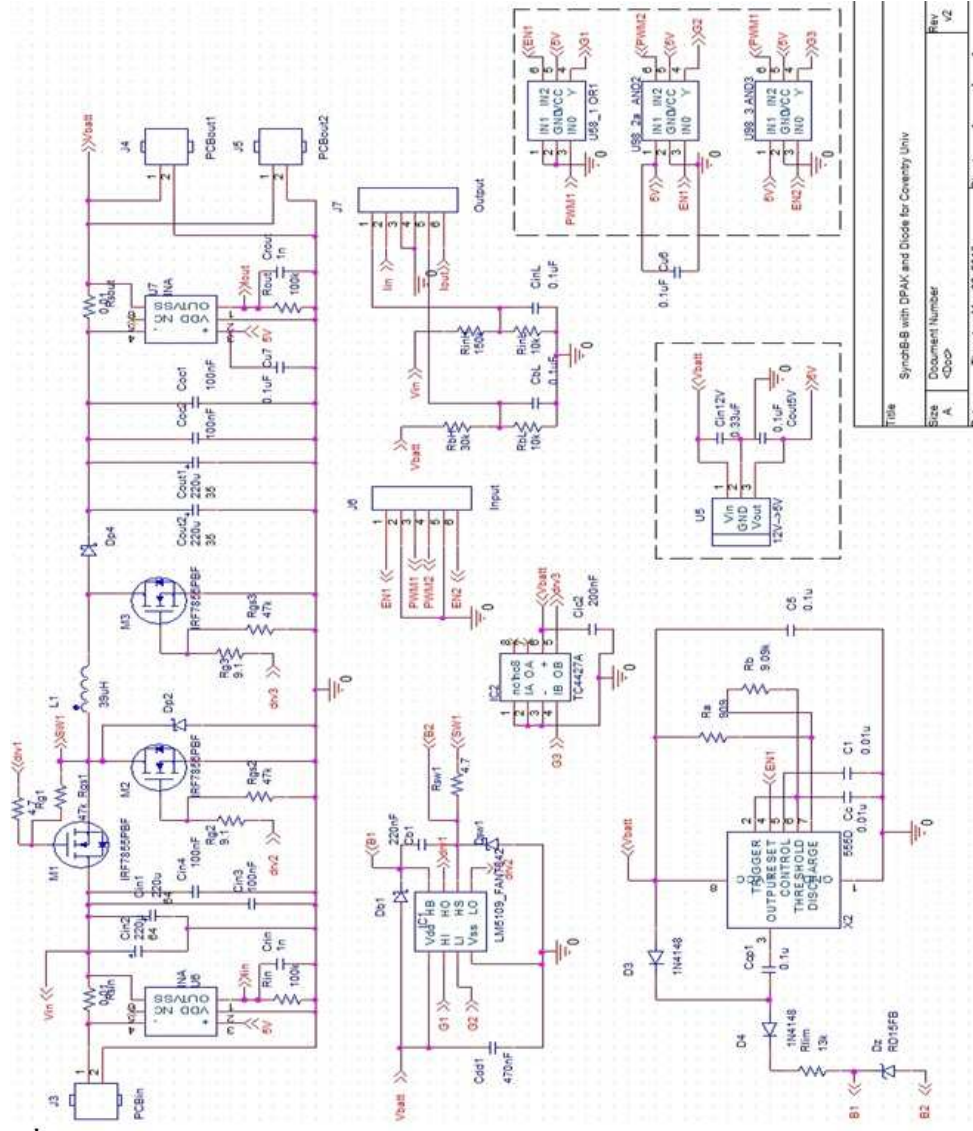
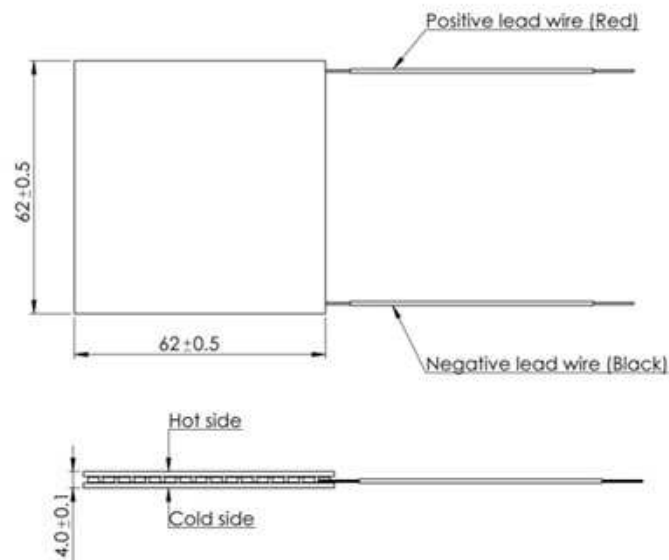


Figure C.3: Schematic diagram of DC-DC buck-boost converter used for experiment tests

C.3 GM250-127-28-12 TEMs characteristics

This material has been removed from this thesis due to Third Party Copyright. The unabridged version of the thesis can be viewed at the Lanchester Library, Coventry University.



This material has been removed from this thesis due to Third Party Copyright. The unabridged version of the thesis can be viewed at the Lanchester Library, Coventry University.

This material has been removed from this thesis due to Third Party Copyright. The unabridged version of the thesis can be viewed at the Lanchester Library, Coventry University.